ANALYSIS OF TWO-DIMENSIONAL LINEAR FIELD PROBLEMS BY SCALED BOUNDARY FINITE ELEMENT METHOD

Mr. Nguyen Van Chung

A Dissertation Submitted in Partial Fulfillment of the Requirements
for the Degree of Doctor of Philosophy Program in Civil Engineering
Department of Civil Engineering
Faculty of Engineering
Chulalongkorn University
Academic Year 2016

การวิเคราะห์ปัญหาสนามเชิงเส้นสองมิติโดยระเบียบวิธีสเกลบาวดารีไฟไนต์เอเลเมนต์

นายเหงวียน วัน จูง

วิทยานิพนธ์นี้เป็นส่วนหนึ่งของการศึกษาตามหลักสูตรปริญญาวิศวกรรมศาสตรดุษฎีบัณฑิต
สาขาวิชาวิศวกรรมโยธา ภาควิชาวิศวกรรมโยธา
คณะวิศวกรรมศาสตร์ จุฬาลงกรณ์มหาวิทยาลัย
ปีการศึกษา 2559

Thesis Title	ANALYSIS OF TWO-DIMENSIONAL LINEAR FIELD PROBLEMS BY SCALED BOUNDARY FINITE ELEMENT METHOD
By	Mr. Nguyen Van Chung
Field of Study	Civil Engineering
Thesis Advisor	Associate Professor Jaroon Rungamornrat, Ph.D.

Accepted by the Faculty of Engineering, Chulalongkorn University in Partial Fulfillment of the Requirements for the Doctoral Degree

______________________Dean of the Faculty of Engineering

(Associate Professor Supot Teachavorasinskun, D.Eng.)

THESIS COMMITTEE

______________________Chairman

(Professor Teerapong Senjuntichai, Ph.D.)

______________________Thesis Advisor

(Associate Professor Jaroon Rungamornrat, Ph.D.)

______________________Examiner

(Assistant Professor Watanachai Smittakorn, Ph.D.)

______________________Examiner

(Associate Professor Akhrawat Lenwari, Ph.D.)

______________________External Examiner

(Associate Professor Suchart Limkatanyu, Ph.D.)

เหงวียน วัน จูง : การวิเคราะห์ปัญหาสนามเชิงเส้นสองมิติโดยระเบียบวิธีสเกลบาวดารีไฟไนต์เอเลเมนต์ (ANALYSIS OF TWO-DIMENSIONAL LINEAR FIELD PROBLEMS BY SCALED BOUNDARY FINITE ELEMENT METHOD) อ.ที่ปรึกษาวิทยานิพนธ์หลัก: รศ. ดร. จรูญ รุ่งอมรรัตน์, 70 หน้า.

ดุษฎีนิพนธ์ฉบับนี้นำเสนอการพัฒนาระเบียบวิธีเชิงตัวเลขที่มีความถูกต้องและมีประสิทธิภาพโดยอ้างอิงระเบียบวิธีสเกลบาวดารีไฟไนต์เอลิเมนต์ซึ่งสามารถแก้ปัญหาหลายสนามเชิงเส้นสองมิติอันดับที่สอง สมการกำกับพื้นฐานถูกสร้างในรูปแบบทั่วไปซึ่งทำให้สามารถแก้ปัญหาค่าขอบเขตหลายประเภทในลักษณะเดียวกัน อาทิเช่น ปัญหาการเหนี่ยวนำความร้อนแบบคงตัว การไหลแบบคงตัวในวัสดุพรุน ปัญหายืดหยุ่นเชิงเส้น ปัญหาไพอิโซอิเลคทริกเชิงเส้น และปัญหาสนามร่วมอื่นๆที่เกี่ยวข้อง สมการสเกลบาวดารีไฟไนต์เอลิเมนต์ถูกพัฒนาขึ้นบนกรอบกว้างซึ่งรวมอิทธิพลของแหล่งวัตถุแผ่กระจาย เงื่อนไขขอบเขตทั่วไป การมีส่วนร่วมของผิวด้านข้างทั้งประเภทที่ทราบค่าฟลักซ์พื้นผิวและประเภทที่ทราบค่าตัวแปรสถานะ และความยืดหยุ่นในการประมาณผลเฉลยที่ขอบเขตของโดเมน ผลที่ได้จากการวิเคราะห์ปัญหาหลากหลายประเภทได้ถูกนำเสนอในดุษฎีนิพนธ์ฉบับนี้ไม่เพียงเพื่อยืนยันความถูกต้องของระเบียบวิธีที่พัฒนาขึ้นเท่านั้น แต่ยังแสดงให้เห็นถึงความสามารถและประสิทธิภาพในเชิงการคำนวณของระเบียบวิธีดังกล่าวด้วย

ภาควิชา วิศวกรรมโยธา ลายมือชื่อนิสิต ....

สาขาวิชา วิศวกรรมโยธา ลายมือชื่อ อ.ที่ปรึกษาหลัก ....

ปีการศึกษา 2559

5671455521 : MAJOR CIVIL ENGINEERING

KEYWORDS: MULTI-FIELD PROBLEMS / SBFEM / SURFACE FLUX / STATE VARIABLE / SCALED BOUNDARY COORDINATES

NGUYEN VAN CHUNG: ANALYSIS OF TWO-DIMENSIONAL LINEAR FIELD PROBLEMS BY SCALED BOUNDARY FINITE ELEMENT METHOD. ADVISOR: ASSOC. PROF. JAROON RUNGAMORNRAT, Ph.D., 70 pp.

This dissertation presents the development of an efficient and accurate numerical technique based upon the scaled boundary finite element method that is capable of solving two-dimensional, second-order, linear, multi-field problems. Basic governing equations are established in a general context allowing various classes of linear boundary value problems such as the steady-state heat conduction, the steady-state flow in porous media, linear elasticity, linear piezoelectricity, and other related couple-field problems to be treated in a unified fashion. The scaled boundary finite element equations are also formulated within a broad framework integrating the influence of the distributed body source, general boundary conditions, contributions of the side face with either prescribed surface flux or prescribed state variable, and the flexibility of the scaled boundary approximations. Several examples are solved and selected results are reported not only to verify the implemented technique but also to demonstrate its vast capability, computational efficiency, and robustness.

Department: Civil Engineering Student's Signature ....

Field of Study: Civil Engineering Advisor's Signature ....

Academic Year: 2016

ACKNOWLEDGEMENTS

I would like to express my deep sense of gratitude to Associate Professor Dr. Jaroon Rungamornat, my advisor, for advising me on this research topic. Without his timely support, encouragement and advice this thesis would not have been completed. He has been a continuous source of inspiration throughout my study here. His insights and ideas helped me overcome this research toward the completion of this thesis.

The author gratefully acknowledge the support by CU Scholarship for ASEAN countries 2013 for giving me the opportunity purse a Doctor’s Degree in Civil Engineering in the field of Structure Engineering. I also thank the International School of Engineering at Chulalongkorn University for their supporting programs. I express my gratitude to Chulalongkorn University for support for the duration of my studying.

My sincere thank to all committee members, namely, Professor Dr. Teerapong Senjuntichai, Associate Professor Dr. Wantanachai Smittakorn, Associate Professor Dr. Akharawat and Associate Professor Suchart Limkatanyu for their helpful suggestions and comments.

I would like to extend my thanks to all my colleagues and friends for the duration of my studies. Finally, I appreciate and thank my parents, my brothers and sisters for their supporting, patience and encouragements.

CONTENTS

Page

Page

LIST OF ABBREVIATIONS

$\boldsymbol{A}$	Coefficient matrix of a system of linear algebraic equations
BEM	Boundary element method
FEM	Finite element method
SBFEM	Scaled boundary finite element method
C	Defining curve
$\boldsymbol{C}^{+}, \boldsymbol{C}^{-}$	Vectors containing arbitrary constants corresponding to each mode
$\boldsymbol{D}$	Modulus matrix
dA	Differential area
$\boldsymbol{E}_0, \boldsymbol{E}_1, \boldsymbol{E}_2$	Coefficient matrices
$\boldsymbol{F}_1^t, \boldsymbol{F}_2^t$	Vector of prescribed surface flux
$\boldsymbol{I}_{\Lambda\times\Lambda}$	Identity matrix of size $\Lambda\times\Lambda$
$\boldsymbol{J}$	Jacobian of transformation
$\boldsymbol{K}$	Stiffness matrix
$\boldsymbol{L}$	Differential operator
$\boldsymbol{N}^{G}$	Vector containing all nodal basic functions for approximating defining curve
$\boldsymbol{N}^{S}$	Vector containing all nodal basic functions for approximating the state variable
$\boldsymbol{T}$	Jacobian matrix
$\boldsymbol{P}_1,\ \boldsymbol{P}_2$	The equivalent nodal internal flux on boundary
$\boldsymbol{Q}^h$	The nodal internal flux
$\boldsymbol{R}$	Inverse of Jacobian matrix
$\boldsymbol{U}^h$	Vector containing all functions $\boldsymbol{u}_{(i)}^{h}(\xi)$
$\boldsymbol{U}^{hu}$	Contains only unknown functions from a collection $\boldsymbol{u}_{(i)}^{h}(\xi)$

$\boldsymbol{U}^{hc}$	The prescribed state variable on the side face
$\boldsymbol{X}_{\alpha}$	Vector containing nodal relative coordinates
Ω	Body of interest
$\boldsymbol{W}^{h}$	Vector containing all functions $\boldsymbol{w}_{(i)}^{h}(\xi)$
Π	Diagonal matrix containing ξ^{λ_i}
$\boldsymbol{b}$	Distributed body source
$\boldsymbol{b}_1$, $\boldsymbol{b}_2$	Matrices in the linear difference operator $\boldsymbol{L}$
$c_j^{b}, c_j^{t1}, c_j^{t2}, c_j^{uc}$	Vector of unknown constants in the terms of the particular solution
$d\xi$	The differential line at any point (ξ, s) in the $\xi - s$ plane
dx	The differential line at any point (x_1, x_2) in the $x_1 - x_2$ plane
$d\lambda$	The length of $d\xi$
dl	The length of dx
h	Superscript used to designate approximate quantities
hu	Superscript used to designate unknown functions
hc	Superscript used to designate known functions
m	Number of modes
n	Number of elements
p	The number of known functions $\boldsymbol{u}_{(i)}^{h}(\xi)$
$\boldsymbol{n}$	Outward unit normal vector
s	Scaled boundary coordinate
$\boldsymbol{t}_1^{s}$	Surface flux on the side-face-1
$\boldsymbol{t}_2^{s}$	Surface flux on the side-face-2
$\boldsymbol{q}_i^{u}$	Vector representing i^{th} modal internal flux
$\boldsymbol{u}_{(i)}^{h}$	Value of the state variable along the line $s = s_{(i)}$
$error$	The relative prevent error

$\boldsymbol{u}$	State variable
$\boldsymbol{u}^{exact}$	The exact solution of the state variable
$\boldsymbol{w}$	Weight function
x_{α}	Cartesian coordinates
$x_{\alpha 0}$	Coordinates of scaling center
λ_i	Modal scaling factor
$\boldsymbol{\psi}_i$	Vector representing the i^{th} mode of state variable
$\boldsymbol{q}_i^u$	The i^{th} modal internal flux
$\boldsymbol{\Phi}^{\psi-}$	Matrix containing all vectors $\boldsymbol{\psi}_i^u$
$\boldsymbol{\Phi}^{q-}$	Matrix containing all vectors $\boldsymbol{q}_i^u$
σ	Body flux field
ξ	Radial coordinate
μ	Shear modulus
ν	Poisson ratio
$\bar{\varepsilon}$	State-variable gradient
Λ	Key parameter used to identify type of problems

LIST OF FIGURES

LIST OF TABLES

Chapter 1

INTRODUCTION

In this chapter, the motivation and significance of the current investigation is first addressed. Next, the research objective, scope of work and methodology are presented. Finally, the expected outcome and contribution of the present study are summarized.

1.1 General

Nowadays, most continuum mechanics problems have been performed in mathematical equation. For instance, heat conduction, elastic, plastic, viscoelastic, piezoelectric and other kinds of behavior of isotropic and non-isotropic materials have been expressed by systems of partial differential equations or integral equations. Formulations of problems related to new materials, fracture, fatigue, heat and other fields are well known. However, almost all of the exact solutions of these formulations are unknown. Only some basic problems can be solved in analytical solution when they have a simple domain geometry and boundary conditions. To construct a solution of the general boundary value problems, approximations of the solution form, involved operators, or both may be required. To overcome the limitations, various methods of discretization have been proposed by researchers and mathematicians. Due to the fast growth of digital computers and computational technology, numerical methods have become an efficient tool to investigate all of continuum mechanics problems.

The finite element method (FEM) has become a general tool to solve the mathematical formulation in continuum mechanics problems over sixty years (Reddy, 1993). Nevertheless, FEM is a very general method that can be treated any types of solid mechanics problems, there are difficulties to solve problems in certain areas, such as dynamic analysis of large or unbounded domains, wage propagation, crack propagation, stress concentration, etc. These difficulties have played an important role for the appearance of the Boundary Element Method (BEM). In this method, governing equations of boundary problems are expressed as boundary integral equations and the spatial dimension of the problem is reduced by one. These led to the reduction of the computation and data preparation. In addition, the BEM has become a numerical tool efficient for the treatment of an unbounded domain where all involved fundamental solutions satisfy the remote boundary conditions exactly. The BEM has been continuously developed and widely employed as an efficient numerical tool in the area of applied mechanics and modeling. Recently, a scaled boundary finite element method (SBFEM) has appeared as a new computational procedure which has overcome many difficulties found in standard FEM and combined the advantages of both the FEM and the BEM.

The scaled boundary finite element method is recognized as a semi-analytical technique combining features of both analytical schemes and the finite element approximation. The SBFEM is achieved in two purposes such with regards to the analytical and numerical method and to the standard procedure of the finite element and boundary element method within the numerical procedures (Wolf, 2003). This method is an order reduction method which links to both finite element and boundary element method. It is a semi-analytical method for continuum analysis and no fundamental solution is required.

The scaled boundary finite element method has demonstrated many advantages with its own salient features. The SBFEM is based on the standard finite element procedure so that it does not require fundamental solutions. Like the BEM, only the boundary is discretized and reduced the spatial discretization by one. These led to the increase of computational efficiency. On the other hand, the SBFEM can solve the difficulties of the FEM very well. For example, analysis of straight interface between two materials passing the scaling center, discretization is not required; analysis of singularity and stress discontinuities in fracture mechanic that are modeled and calculated analytically by analytical solution in the radial direction. Particularly, the SBFEM can easily model infinite domain and get the results higher accuracy than other approaches. In contrast to the BEM, the property matrices of an unbounded domain could be coupled with the structure of formulating equations to analyze problem-structure interaction by substructure method (Wolf and Song, 1996b; Wolf, 2003). Finally, the advantages of the scaled boundary finite element method were compared with the finite element and boundary element methods, shown in Table 1.1.

In last two decades, the SBFEM has been developed for unbounded and bounded domains in two and three-dimensional media. The method was originally derived to compute the dynamic stiffness of the unbounded domain (Wolf and Song, 1996b). The SBFEM has proved to be more general than initially investigated, then developments has allowed analysis of incompressible material and bounded domain (Wolf and Song, 1996a), and inclusion of body loads (Song and Wolf, 1999). The complexity of the original derivation of this technique led to develop weighted residual formulation (Song and Wolf, 1997; Wolf and Song, 2001). Then Deeks and Wolf (2002) and Deeks (2004) commenced with virtual work and novel semi-analytical approach of the scaled boundary finite element method to derive the standard finite element method for two dimensional problems in solid mechanics accessibly.

Table 1.1: Features of SBFEM, FEM and BEM (Wolf, 2003).

Features	FEM	BEM	SBFEM
Reduction of the spatial dimension		x	x
Analytical solution completed inside domain			x
No fundamental solutions and treatment of singular integrals	x		x
Radiation condition at infinity satisfied exactly for modeling unbounded domain		x	x
No discretization of free and fixed boundaries and interfaces between different materials			x
No approximation other than that of the surface finite elements on the boundary		x	x
Symmetric stiffness matrices for finite media (super-element)	x	(x)	x
Symmetric stiffness and unit-impulse response matrices for unbounded domain	x	x	x
Body loads processed without additional domain	x		x
Stress concentrations and intensity factors are calculated directly based on their definition			x
No fictitious Eigen-frequencies for unbounded media	x		x
Straightforward coupling by standard assemblage of structure with finite elements in unbounded medium	x		x

Other recent applications of the SBFEM have been also recognized. This method has been applied to treat various problems such as solving problems with concentrated load (Vu and Deeks, 2014), modeling elasto-plastic material responses in structures (Ooi et al., 2014), treatment electrostatic problems (Liu and Lin, 2012), identity parameter of elastic orthotropic (Chen et al., 2013), analysis of fracture problem in piezoelectric materials, etc. On the other hand, the SBFEM was also extended to analysis of the temperature for heat conductions fields (Li and Ren, 2016). Other published papers investigated the SBFEM in analysis of piezoelectric and composites fields. For instance, the SBFEM was applied for fracture analysis of piezoelectric composites under thermal load (Li et al., 2015), for semi-analytical analysis of piezoelectric plate (Li et al., 2011), and for 2D analysis of crack and interface crack in piezoelectric composites (Li et al., 2014). Moreover, the SBFEM has widely applied to construct adequate numerical alternatives for the solutions of formulations in solid-structure interaction, diffusion, fracture mechanic, piezoelectric, elasto-plastic and other fields.

These presented researches have proposed that SBFEM had more advantages in terms of accuracy, simplicity and efficiency. Nevertheless, all of the published researches, the formulations of problems developed for specific problems corresponding to the features of the SBFEM. These procedures did not solve various particular problems as changing the parameters of governing equations; considering the influence of the distributed body source, general boundary conditions, and contributions of the side face with either prescribed surface flux or prescribed state variable; and or general domain. Therefore, the motivation of this study with regards of the intention of developing a general algorithm for multi-field problems to solve various problems under different scenarios to demonstrate its vast capability, computational efficiency and robustness, based on the features of the scaled boundary finite element method.

1.2 Objectives

The main objectives of the present research are (1) to develop scaled boundary finite element method capable of solving general, linear multi-field boundary value problems and (2) to investigate the computational performance of the developed numerical technique such as the convergence, accuracy and capability of solving a variety of problems.

1.3 Scope of Work

The present study is limited to following situations: (i) a body is represented by either a bounded or an unbounded region in a two-dimensional physical space with its geometry completely described by a simple, single region bounded by the constant coordinates in the scaled boundary transformation space; (ii) basic equations governing all field quantities such as the state variable, the measure of spatial variation of the state variable, and body flux are assumed in a linear form, and the final governing equations only involve a set of linear, second-order, partial differential equations of an elliptic type and are applicable to various classes of boundary value problems such as steady-state heat conduction problems, steady-state Darcy's flow problems, membrane problems, Laplace's equation, linear elasticity, and problems involving multi-field materials such as linear piezoelectric, piezomagnetic and piezoelectromagnetic solids; (iii) boundary conditions on the inner and outer boundaries can be general whereas either the state variable or the surface flux is prescribed on the entire side faces; and (iv) prescribed distributed body source and prescribed data on the side-faces are assumed expressible in a polynomial form.

1.4 Methodology

Key procedure and methodology proposed for the development of the scaled boundary finite element method for general, linear multi-field boundary value problems are summarized as follows:

(1) Fundamental laws of conservations (e.g., conservation of linear and angular momentum, conservation of mass, conservation of heat flow, etc.), linear constitutive laws (e.g., Darcy's law, Fourier's law, Hookes' law, generalized Hookes' law, etc) and the laws of kinematics (e.g., strain-displacement relations, electric potential-field relations, etc.) are used as the basis in the formulation of general basic equations governing field quantities of interest. The formulation is established in a unified manner allowing the treatment of various classes of boundary value problems such as steady-state heat conduction problems, steady-state Darcy's flow problems, membrane problems, Laplace's equation, linear elasticity, and problems involving multi-field materials such as linear piezoelectric, piezomagnetic and piezoelectromagnetic solids.

(2) The standard weighted residual technique along with the integration by parts via Gauss-divergence theorem is employed to derive the weak-form equation.

(3) A scaled boundary coordinate transformation is utilized to describe the geometry of bodies and then the formulation is transformed to that involving the scaled boundary coordinates.

(4) Scaled boundary finite element approximation is adapted to approximate the weak-form equation. The geometry of the body, the field quantities, and the weight function are interpolated from values or functions along the scaling coordinate direction using standard basis functions defined in the boundary coordinate direction.

(5) Scaled boundary finite element equations are obtained from the weak-form via the use of scaled boundary finite element approximation along with the

integration by parts with respect to the scaling coordinate. The original system of linear partial differential equations is transformed into a system of linear, non-homogeneous, second-order, ordinary differential equations of Euler-Cauchy type and two sets of boundary conditions on the inner and outer boundaries.

(6) A standard technique for solving the differential equations of Euler-Cauchy type is utilized to determine the homogeneous solution and this process results in an equivalent linear eigenvalue problem. All eigenvalues and the corresponding eigenvectors are solved using a selected efficient numerical procedure.

(7) The particular solution of the system of linear differential equations associated with the prescribed distributed body source and the prescribed state variable and the prescribed surface flux on the side faces is constructed via the well-known method of undetermined coefficients.

(8) The final general solution is obtained by enforcing the boundary conditions on both inner and outer boundaries of the body.

(9) All field quantities of interest within the body can be post-processed using the nodal basis functions along with the approximate solution obtained along the scaling coordinate direction.

(10) The implemented technique is fully tested by comparing with existing analytical and reference solutions for various scenarios.

1.5 Outcomes and Contributions

The present investigation offers an alternative, accurate and efficient numerical technique (in terms of an in-house computer package) capable of solving a variety of two-dimensional, linear boundary value problems commonly encountered in the physical modeling. The important contribution and novel aspect of the current work stem directly from the key formulation and implementations of the scaled boundary finite element method, which are to be established in a general framework allowing many governing physics and various scenarios (such as bounded/unbounded bodies, external excitations, prescribed boundary conditions) to be treated in a unified fashion. The full investigation of the computational performance of the proposed procedure should offer its pros and cons in comparison with other existing numerical techniques and also provide a general guideline for selecting the SBFEM as an efficient tool in the solution search. In addition, the framework of the SBFEM established in the present study provides a sufficient and essential basis for its generalization to treat more complex/general bodies along with the sub-domain technique and its extension to three-dimensional problems.

Chapter 2
BACKGROUND AND REVIEW

This chapter briefly summarizes the background and relevant literature concerning the scaled boundary finite element method in various aspects such as its first development, the underlying formulation, numerical implementations, and its applications to various classes of boundary value problems. Pros and cons, advantages, drawbacks, limitations and possible extensions of existing work are pointed out and discussed. Additionally, results from this extensive survey indicate the significance and novelty of the present investigation.

2.1 Background of Scaled Boundary Finite Element Method

The scaled boundary finite element method was originally developed to solve both bounded and unbounded domains during the 1990s. The first derivation of the method was presented by the infinitesimal finite element method (Wolf and Song, 1995a), and later the consistent infinitesimal finite element cell method (Wolf and Song, 1995b). However, the original mechanical-based derivation of the SBFEM in these publications, which involved mathematically, may be contributed lower than other engineering researchers. On purposes to raise its application and to demonstrate its advantages as a computational tool in analysis of dynamic stiffness of an unbounded domain, the method was re-derived by using a weighted residual approach. By means of weighted residual approaches, a displacement formulation in the frequency domain was derived for general problems in elastodynamics in three dimension (Song and Wolf, 1997).

In the progress of the SBFEM, the first derivation was compared with an example application and solution, and then re-derived using a mechanical-based approach to obtain the governing equations (Wolf and Song, 2000; Song and Wolf, 2000). This solution procedure was illustrated by solving a homogenous bounded medium and an unbounded medium. In developments, while the researchers found that the complexity of the original derivation technique led to the weighted residual formulation for SBFEM, it was still more complex than derivational formulation of the finite element method. Therefore, a virtual work derivation was developed for the scaled boundary finite element method. A third derivation of the SBFEM was presented by Deeks and Wolf (2002). They commenced with a new virtual work derivation of the scaled boundary method to develop a standard finite element method for two dimensional problems in solid mechanics accessibly. The new formulation treated both bounded and unbounded domain involving the stress singularities.

In recent years, the SBFEM has also been developed to solve various problems. In fracture mechanics, a salient feature of the SBFEM is that whole problem domain is generated by the scaling boundary to a single point which is called the scaling center. It is defined at the crack tip; the stress field is expressed analytically along the radian direction from the crack tip. It can be calculated directly on the obtained solution which led to the stress singularity more accurately (Chowdhury et al., 2014; Dai, et al., 2015). Based on this feature, many fields of fracture mechanics have been modeled to validate such as crack propagation, dynamic crack propagation, and transient respond of finite biomaterial plates with interface crack (Song et al., 2010). Furthermore, the SBFEM has widely investigated in elastic guided waves, water wave, an unbounded domain (Gravenkamp et al., 2014; Doherty and Deeks, 2005; Meng and Zou, 2013). The researchers applied SBFEM to solve the radiation and diffraction of linear water waves in shallow water with sidewall. The results demonstrated that this method had more accurate and computational efficient than other published approaches.

2.2 Applications of Scaled Boundary Finite Element Method

In many engineering applications, the SBFEM has been a new attractive alternative computational technique. The desirable features of this method include the reduction of the spatial dimension of the key governing equations, combining the advantages of both FEM and BEM, and efficient and useful for the analysis of problems concerning infinite domains and problems in linear fracture mechanics. It is also a novel-analytical method for continuum analysis requiring no fundamental solution. For simple geometries, the SBFEM only requires meshing on the boundary of analyzed domain and does not need a fundamental solution. For complex problems, the interior of domain can be discretized into subdomains to satisfy the scaling requirement. On the other hand, the stress singularities and bi-material interfaces can be analyzed by definition with no singular integrals (Wolf, 2003).

The basic concept of employing the SBFEM to model a bounded or an unbounded domain is illustrated in Figures 2.1 and 2.2. A scaling center O, which must be chosen either within or outside the domain, is visible in the totally boundary. The origin of the Cartesian coordinates $\{x_1, x_2\}$ is commonly selected at the scaling center. The boundary is represented into one-dimension line elements. The shape functions are used to interpolate the geometry of an element on the boundary. The geometry of the domain is described by a normalized radial coordinate ξ which starts from the scaling center to its boundary. The values of ξ is specified as 0 at the scaling center and 1 at the boundary (for a bounded domain). The coordinate system consisting of the coordinate ξ in the radial direction and the coordinate s in the circumferential direction can be used to completely describe the geometry of the domain.

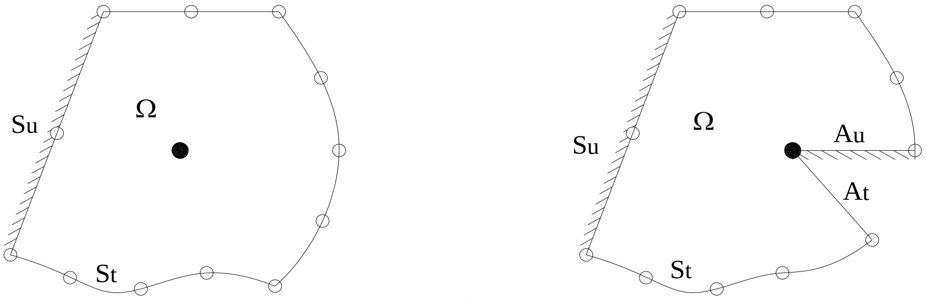

(a) (b)

Figure 2.1: Scaled boundary coordinate system for bounded bodies: (a) the scaling center inside body and (b) the scaling center on the boundary and body containing side faces.

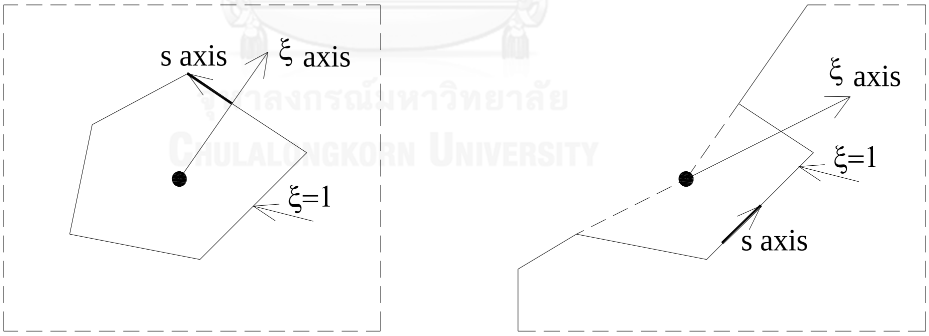

(a) (b)

Figure 2.2: Scaled boundary coordinate system for unbounded bodies: (a) a body without side face and (b) a body with side faces.

On the domain boundary, the nodal state variable functions are first introduced and then interpolated by the nodal basis functions to obtain values at any location. The scaled boundary coordinate transformation is utilized to describe the geometry of bodies and the formulation is transformed into that involving the scaled boundary coordinates. The SBFEM equations in state variable are obtained by applying the weighted residual method or the principle of virtual work for the governing differentials in the circumferential direction s. Coefficient matrices of the SBFEM are calculated in the same way as the stiffness matrix in the finite element method. For instance, the SBFEM equations in the static analysis are reduced to be into of first-order ordinary differential equations which can be solved by eigenvalue problem. Thus, the state variables and flux fields are represented by semi-analytical solutions which permit the boundary at infinity to be satisfied rigorously. Most of the procedures of the SBFEM were based on the basic solution above. However, there is a little difference at post procedure to determine the state variable field or the flux fields in particular problems. For instance, in analysis of fracture problem, the basic concept of the SBFEM solution is obtained as the basic procedure above, and then stress intensity factor analysis, propagation analysis are simulated basing on its definition (Shrestha and Ohga, 2007).

Deeks and Wolf (2002) used an h-hierachical adaptive procedure in the SBFEM. This technique took the ability of the SBFEM to model stress singularities at the scaling center and to avoid discretization of certain adjacent segments of the boundary. Vu and Deeks (2006) investigated high-order elements in the SBFEM. The spectral element and hierarchical approach were employed in this study. They found that the spectral element approach was better than the hierarchical approach. Doherty and Deeks (2005) developed a meshless scaled boundary method to model the far field and the conventional meshless local Petrov-Galerkin modeling. This combining was general and could be employed to other techniques of modeling the far field. Although, the SBFEM has demonstrated many advantages in the approach method, it also has had disadvantaged in solving problems involving an unbounded domain or stress singularities. When the number of degrees of freedom became too large, the computational expense was a trouble. So, Vu and Deeks (2008) developed a p-adaptive in the SBFEM for the two dimensional problem. These authors investigated an alternative set of refinement criteria. This led to be maximize the solution accuracy and minimizing the cost. Furthermore, He et al. (2012) presented a new Element-free Galerkin scaled boundary method to approximate in the circumferential direction. This work was applied to a number of standard linear elasticity problems, and the technique was found to offer higher and better convergence than the original SBFEM. Additionally, He et al. (2014) investigated the possibility of using the Fourier shape functions in the SBFEM to approximate in the circumferential direction. This research used to solve three elastostactic and steady-state heat transfer problems. They found that the accuracy and convergence were better than using polynomial elements or using an element-free Galerkin to approximate on the circumferential direction in the SBFEM. These published papers focused on the shape functions and applied in individual particular problem to show the advantages of the SBFEM. They may not provide the advantages of the using other kinds of shape function for general problem. They only used typical function to apply in the SBFEM for each particular problem such as using linear shape functions for heat problem, two dimensional problems, etc.

The computational efficient of the analysis for the piezoelectric materials using the SBFEM has been increased significantly by adopting the SBFEM. Li et al. (2013) developed and employed SBFEM to analyze two-dimensional problems of piezoelectric material. The stress and electric displacement intensity factor in both static and dynamic were evaluated by extending SBFEM. No asymptotic solution, local mesh refinement or special treatment around a crack tip was required. The author provided the highlight, the accuracy, simplicity and efficiency of this method. Dieringer and Becker (2015) presented the employment of the SBFEM for problems within the framework of classical laminated plate theory. The researcher dedicated to derive the scaled boundary finite element equations in displacements for composites and to examine stress singularities in a notch. They demonstrated the enhancement of the SBFEM that could evaluate the stress singularities field as a function of the notch opening for wide variety of composites. On the other hand, they also provided the accuracy and efficiency of employed SBFEM for arbitrarily laminated plates. These publications provided the improvement of the SBFEM to analyze stress singularities. However, they only focused on the individual advantage of the SBFEM, examined each particular in piezoelectric field and they could not analyze general problems of piezoelectric.

In recent decades, many researchers have studied the SBFEM. Li et al. (2013a) and Li et al. (2013b) extended the SBFEM to develop a computation model for the three-dimensional wave-pile and to investigate both wave behavior and pile group responses. This publication employed the basic concept SBFEM equation into the Helmholtz equation by separating the vertical-direction component from velocity potential. Two dimensional SBFEM investigated at the free surface level of the wave field. Li et al. (2011) used SBFEM to analysis of structural behavior of offshore monopoles with ocean wave load, the basic concept SBFEM equations were implemented to formulate the governing mono-pile’s equation and analytical wave equation. These published papers showed the SBFEM in which had high efficiency and accuracy in analysis of the wave domain, the wave-structure interaction. Nonetheless, they only focused on the individual particular problem. They could not solve the general problem for both wave domain and wave-structure interaction.

In nearly years, Vu and Deeks (2014) used fundamental solutions in the scaled boundary finite element method to solve problems with concentrated loads. Liu and Lin (2012) extended the SBFEM to treat electrostatic problems. He et al. (2013) presented an approach method to develop for numerical analysis of 2D elastic systems with rotationally periodic symmetry under arbitrary load conditions. Ooi et al. (2012) and Ooi et al. (2013) developed an efficient methodology for automatic dynamic crack propagation simulations using scaled boundary polygon elements.

The aforementioned works have shown various important progresses to implement the SBFEM in analysis of engineering problems. However, the existing methods are nearly all focused on the analysis of the structural response through the SBFEM. The alternative computational procedure was only solved for individual particular problem and presented each advantage of the SBFEM, while less work has been conducted for its advantages to apply for general problems. In real structures and analysis, many parameters such as material properties, loads or geometrical characteristics can be performed. They are very important for problems analysis to improve the SBFEM's applicability in real analysis. Additionally, the multi-field problems are analyzed by using the SBFEM; they may be a future topic in applying new technique computation instead of employing for an individual problem.

Chapter 3
FORMULATION

This chapter first summarizes the clear description of the problem, basic governing field equations for two-dimensional, linear multi-field problems, and the corresponding weak formulation. Then, the scale boundary coordinates transformation and the scale boundary finite element approximation are introduced. Finally, the scale boundary finite element equations are presented.

3.1 Problem Description

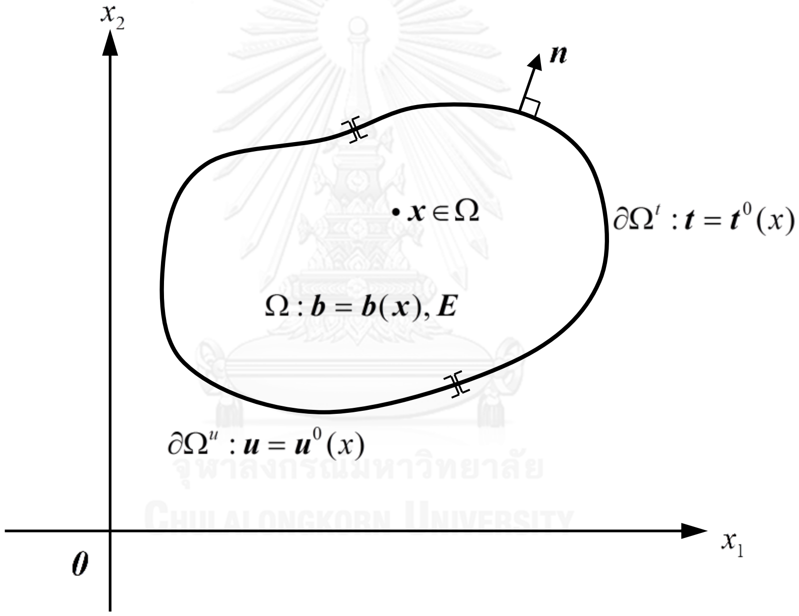

Figure 3.1: Schematic of two-dimensional, multi-field body subjected to external excitations.

Let us consider a two-dimensional body occupying a region Ω in R^2 as shown schematically in Figure 3.1. The region is assumed *smooth* in the sense that all involved mathematical operators (e.g., integrations and differentiations) can be performed over this region. In addition, the boundary of the body Ω, denoted by $\partial\Omega$, is assumed piecewise smooth and an outward unit normal vector at any smooth point on $\partial\Omega$ is denoted by $\boldsymbol{n} = \{n_1 \;\; n_2\}^T$. The interior of the body is denoted by $\text{int}\,\Omega$. More restrictions about the geometry of the body Ω will be placed later in the following development of the key formulation.

For convenience in further reference and presentations, a two-dimensional, reference Cartesian coordinate system $\{\boldsymbol{0}; x_1, x_2\}$ is introduced where $\boldsymbol{0}$ denotes the origin and x_1, x_2 denote the orthogonal coordinate axes (see Figure 3.1). A symbol $f_{,\alpha}$ is used throughout to denote a partial derivative of a function f with respect to the spatial coordinate x_α, $\alpha \in \{1,2\}$ (i.e., $f_{,\alpha} = \partial f / \partial x_\alpha$) and, here and in what follows, standard indicial notations apply for subscripts with lower case Greek and upper case indices. In particular, lower Greek subscripts range from 1 to 2 whereas upper case subscripts range from 1 to $\Lambda \in \{1,2,3,\ldots\}$ and repeated subscripts imply the summation over their range unless stated otherwise.

The body is made of a homogeneous material with its behavior completely characterized by $4\Lambda^2$ constants denoted by at a set $\{E_{\alpha IJ\beta}\}$ and subjected to a prescribed distributed body source field at any point $\boldsymbol{x} \in \Omega$, denoted by an Λ-component vector $\boldsymbol{b} = \boldsymbol{b}(\boldsymbol{x}) = \{b_1(\boldsymbol{x}) \;\; b_2(\boldsymbol{x}) \; \ldots \; b_\Lambda(\boldsymbol{x})\}^T$. In the present study, the constants $E_{\alpha IJ\beta}$ are assumed to satisfy the following symmetry condition $E_{\alpha IJ\beta} = E_{\beta JI\alpha}$. Responses of the body due to the applied distributed body source $\boldsymbol{b} = \boldsymbol{b}(\boldsymbol{x})$ are assumed to be completely described by the following three field quantities: the state variable $\boldsymbol{u} = \boldsymbol{u}(\boldsymbol{x})$, the state-variable gradient $\bar{\boldsymbol{\varepsilon}} = \bar{\boldsymbol{\varepsilon}}(\boldsymbol{x})$, and the body flux $\boldsymbol{\sigma} = \boldsymbol{\sigma}(\boldsymbol{x})$. The state variable $\boldsymbol{u} = \boldsymbol{u}(\boldsymbol{x})$ contains Λ components denoted by $u_J(\boldsymbol{x})$ and is represented in a vector form by

$$u(x) = \{u_1(x) \quad u_1(x) \quad \ldots \quad u_\Lambda(x)\}^T \tag{3. 1}$$

The state-variable gradient $\bar{\boldsymbol{\varepsilon}} = \bar{\boldsymbol{\varepsilon}}(\boldsymbol{x})$ and the body flux $\boldsymbol{\sigma} = \boldsymbol{\sigma}(\boldsymbol{x})$ contain $2 \times \Lambda$ components denoted by $\bar{\varepsilon}_{\alpha J}$ and $\sigma_{\alpha J}$, respectively and they can also be represented in a vector form by

$$\bar{\boldsymbol{\varepsilon}}(\boldsymbol{x}) = \{\bar{\varepsilon}_{11}(\boldsymbol{x}) \;\; \bar{\varepsilon}_{12}(\boldsymbol{x}) \; \ldots \; \bar{\varepsilon}_{1\Lambda}(\boldsymbol{x}) \;\; \bar{\varepsilon}_{21}(\boldsymbol{x}) \;\; \bar{\varepsilon}_{22}(\boldsymbol{x}) \; \ldots \; \bar{\varepsilon}_{2\Lambda}(\boldsymbol{x})\}^T \tag{3. 2}$$

$$\boldsymbol{\sigma}(\boldsymbol{x}) = \{\sigma_{11}(\boldsymbol{x}) \;\; \sigma_{12}(\boldsymbol{x}) \; \ldots \; \sigma_{1\Lambda}(\boldsymbol{x}) \;\; \sigma_{21}(\boldsymbol{x}) \;\; \sigma_{22}(\boldsymbol{x}) \; \ldots \; \sigma_{2\Lambda}(\boldsymbol{x})\}^T \tag{3. 3}$$

In addition, the surface flux at any smooth point on the boundary is denoted by an Λ-component vector $\boldsymbol{t} = \boldsymbol{t}(\boldsymbol{x}) = \{t_1(\boldsymbol{x}) \;\; t_2(\boldsymbol{x}) \; \ldots \; t_\Lambda(\boldsymbol{x})\}^T$. The boundary of the given body $\partial\Omega$ can be decomposed into two disjoint portions; one is denoted by $\partial\Omega^u$ where the state variable $\boldsymbol{u}$ is fully prescribed ($\boldsymbol{u} = \boldsymbol{u}^0(\boldsymbol{x}) \; \forall \boldsymbol{x} \in \partial\Omega^u$ where $\boldsymbol{u}^0(\boldsymbol{x})$ is a prescribed vector) and the other is denoted by $\partial\Omega^t$ where the surface flux $\boldsymbol{t}$ is fully prescribed (i.e., $\boldsymbol{t} = \boldsymbol{t}^0(\boldsymbol{x}) \;\; \forall \boldsymbol{x} \in \partial\Omega^t$ where $\boldsymbol{t}^0(\boldsymbol{x})$ is a prescribed vector). In the present study, the prescribed vector value functions $\boldsymbol{b}(\boldsymbol{x})$, $\boldsymbol{u}^0(\boldsymbol{x})$ and $\boldsymbol{t}^0(\boldsymbol{x})$ are assumed sufficiently smooth to ensure the existence of the responses $\boldsymbol{u} = \boldsymbol{u}(\boldsymbol{x})$, $\bar{\boldsymbol{\varepsilon}} = \bar{\boldsymbol{\varepsilon}}(\boldsymbol{x})$ and $\boldsymbol{\sigma} = \boldsymbol{\sigma}(\boldsymbol{x})$.

The statement of the problem is to find the state variable $\boldsymbol{u} = \boldsymbol{u}(\boldsymbol{x})$, the state-variable gradient $\bar{\boldsymbol{\varepsilon}} = \bar{\boldsymbol{\varepsilon}}(\boldsymbol{x})$ and the body flux $\boldsymbol{\sigma} = \boldsymbol{\sigma}(\boldsymbol{x})$ within the body Ω associated with the prescribed distributed body source $\boldsymbol{b} = \boldsymbol{b}(\boldsymbol{x})$, the given material properties $\{E_{\alpha IJ\beta}\}$ and the prescribed boundary conditions $\boldsymbol{u}^0(\boldsymbol{x})$ and $\boldsymbol{t}^0(\boldsymbol{x})$ on $\partial\Omega^u$ and $\partial\Omega^t$, respectively.

3.2 Basic Governing Field Equations

A set of field equations governing all field quantities described in the problem description is formulated within a general framework to allow various classes of linear, second-order boundary value problems encountered in many areas (e.g., steady-state heat condition problems, steady-state flow in porous media, membrane problems, linear elasticity, problems associated with multi-field materials such as piezoelectric and piezo-electromagnetic solids, etc.) to be treated in a unified manner. The integer Λ is used as a key parameter to indicate type of the problems. For instance, $\Lambda = 1$ represents the heat condition problems, flow in porous media, and membrane problems and $\{\boldsymbol{u}(\boldsymbol{x}), \bar{\boldsymbol{\varepsilon}}(\boldsymbol{x}), \boldsymbol{\sigma}(\boldsymbol{x}), \boldsymbol{b}(\boldsymbol{x}), E_{\alpha IJ\beta}, \boldsymbol{t}\}$ denotes {temperature, temperature gradient, heat flux, heat source, thermal conductivity, surface heat flux}, {fluid pressure, pressure gradient, fluid flux, source or sink, permeability, surface flux}, and {deflection, slopes, resultant shear force, distributed transverse load, membrane stiffness, end shear force}, respectively; $\Lambda = 2$ represents linear elasticity problems and $\{\boldsymbol{u}(\boldsymbol{x}), \bar{\varepsilon}(x)$ $\sigma(x)$ $\boldsymbol{b}(\boldsymbol{x}), E_{\alpha IJ\beta}, \boldsymbol{t}\}$ therefore denotes {displacement, displacement gradient, stress, body force, elastic constants, traction}; $\Lambda = 3$ represents linear piezoelectric and piezo-magnetic problems and $\{\boldsymbol{u}(\boldsymbol{x}), \bar{\boldsymbol{\varepsilon}}(\boldsymbol{x}), \boldsymbol{\sigma}(\boldsymbol{x}), \boldsymbol{b}(\boldsymbol{x}), E_{\alpha IJ\beta}, \boldsymbol{t}\}$ denotes {displacement and electric potential, displacement gradient and potential gradient, stress and electric induction, body force and charge, elastic and piezoelectric constants and dielectric permittivities, traction and surface charge} and {displacement and magnetic potential, displacement gradient and potential gradient, stress and magnetic induction, body force and magnetic body source, elastic and piezomagnetic constants and magnetic permeabilities, traction and surface magnetic induction}, respectively; and $\Lambda = 4$ represents piezoelectromagnetic problems and $\{\boldsymbol{u}(\boldsymbol{x}), \bar{\boldsymbol{\varepsilon}}(\boldsymbol{x}), \boldsymbol{\sigma}(\boldsymbol{x}), \boldsymbol{b}(\boldsymbol{x}), E_{\alpha IJ\beta}, \boldsymbol{t}\}$ denotes {displacement and electric and magnetic potentials, displacement gradient and potential gradients, stress and electric and magnetic inductions, body force and body charge and magnetic body source, elastic and piezoelectric and piezomagnetic and electromagnetic constants and dielectric permittivities and magnetic permeabilities, traction and surface charge and surface magnetic induction}.

The fundamental laws of conservation (e.g., conservation of linear and angular momentum, conservation of mass, conservation of heat flow, etc.), the linear constitutive laws (e.g., Darcy's law, Fourier's law, Hooke's law, generalized Hooke's law, etc.), and the laws of kinematics (e.g., strain-displacement relations, electric potential-field relations, etc.) are employed to form the basic governing field equations and they are expressed in a single and concise form as indicated below. The body flux field $\boldsymbol{\sigma}(\boldsymbol{x})$ is related to the distributed body source field $\boldsymbol{b}(\boldsymbol{x})$ via a set of Λ-linear partial differential equations:

$$\sigma_{\alpha J,\alpha} + \mathbf{b}_J = 0 \quad or \quad \mathbf{L}^T\sigma + \mathbf{b} = \mathbf{0} \tag{3. 4}$$

where the superscript "T"denotes the transpose operator and $\boldsymbol{L}$ represents the linear differential operator defined, in terms of a $2\Lambda \times \Lambda$-matrix, by

$$\boldsymbol{L} = \begin{bmatrix} \boldsymbol{I}_{\Lambda\times\Lambda} \\ \boldsymbol{0}_{\Lambda\times\Lambda} \end{bmatrix} \frac{\partial}{\partial x_1} + \begin{bmatrix} \boldsymbol{0}_{\Lambda\times\Lambda} \\ \boldsymbol{I}_{\Lambda\times\Lambda} \end{bmatrix} \frac{\partial}{\partial x_2} = \boldsymbol{L}_1 \frac{\partial}{\partial x_1} + \boldsymbol{L}_2 \frac{\partial}{\partial x_2};\ \boldsymbol{L}_1 = \begin{bmatrix} \boldsymbol{I}_{\Lambda\times\Lambda} \\ \boldsymbol{0}_{\Lambda\times\Lambda} \end{bmatrix}, \boldsymbol{L}_2 = \begin{bmatrix} \boldsymbol{0}_{\Lambda\times\Lambda} \\ \boldsymbol{I}_{\Lambda\times\Lambda} \end{bmatrix} \tag{3. 5}$$

with $\boldsymbol{I}_{\Lambda\times\Lambda}$ and $\boldsymbol{0}_{\Lambda\times\Lambda}$ denoting a $\Lambda\times\Lambda$-identity matrix and a $\Lambda\times\Lambda$-zero matrix, respectively. The body flux $\boldsymbol{\sigma}(\boldsymbol{x})$ at any point $\boldsymbol{x}$ is directly related to the state-variable gradient $\bar{\boldsymbol{\varepsilon}}(\boldsymbol{x})$ at the same point via a local, linear constitutive law:

$$\sigma_{\alpha J} = E_{\alpha JK\beta}\bar{\varepsilon}_{\beta K} \quad or \quad \sigma = \mathbf{D}\bar{\varepsilon} \tag{3. 6}$$

where $\boldsymbol{D}$ is a $2\Lambda \times 2\Lambda$ - termed matrix of the modulus matrix. It should be remarked that entries of the modulus matrix $\boldsymbol{D}$ can simply be obtained from the set $\{E_{\alpha IJ\beta}\}$ by properly considering the definition of the vectors $\boldsymbol{\sigma}$ and $\bar{\boldsymbol{\varepsilon}}$ (i.e., $E_{1JK1} = D_{JK}$, $E_{1JK2} = D_{J,K+\Lambda}$, $E_{2JK1} = D_{J+\Lambda,K}$ and $E_{2JK1} = D_{J+\Lambda,K+\Lambda}$) and, due to the symmetry of $E_{\alpha IJ\beta}$, the modulus matrix $\boldsymbol{D}$ is essentially symmetric. Finally, the state-variable gradient $\bar{\boldsymbol{\varepsilon}}(\boldsymbol{x})$ is related to the state variable $\boldsymbol{u}(\boldsymbol{x})$ by

$$\bar{\varepsilon}_{\beta K} = u_{K,\beta} \quad or \quad \bar{\varepsilon} = \mathbf{Lu} \tag{3. 7}$$

By applying the law of conservation at any smooth point $\boldsymbol{x}$ on the boundary $\partial\Omega$, the surface flux $\boldsymbol{t}(\boldsymbol{x})$ can be related to the body flux $\boldsymbol{\sigma}(\boldsymbol{x})$ and the outward unit normal vector $\boldsymbol{n}(\boldsymbol{x}) = \{n_1(\boldsymbol{x})\ \ n_2(\boldsymbol{x})\}^T$ by

$$t_\alpha = \sigma_{\alpha J} n_\alpha \quad or \quad \mathbf{t} = \begin{bmatrix} n_1\mathbf{I} & n_2\mathbf{I} \end{bmatrix}\sigma \tag{3. 8}$$

where again $\boldsymbol{I}$ denotes the $\Lambda\times\Lambda$-identity matrix. The relations (3.4), (3.6) and (3.7) constitute a set of 3Λ linear partial differential equations and 2Λ linear algebraic equations, involve 5Λ unknown functions (i.e., Λ components of the state variable, 2Λ components of the state-variable gradient, and 2Λ components of the body flux), and, as a result, form a complete set of governing equations for determining all field quantities. Other useful relations such as that directly relating the body flux and the state variable and one connecting the surface flux and the state variable on the boundary can readily be established. By combining (3.6) and (3.7), it simply leads to

$$\sigma_{\alpha J} = E_{\alpha JK\beta}u_{K,\beta} \quad or \quad \sigma = \mathbf{D}(\mathbf{Lu}) \tag{3. 9}$$

Then, by substituting (3.9) into (3.8), it yields

$$t_{\alpha} = n_{\alpha}E_{\alpha JK\beta}u_{K,\beta} \quad or \quad \mathbf{t} = \begin{bmatrix} n_1\mathbf{I} & n_2\mathbf{I}\end{bmatrix}\mathbf{D}(\mathbf{Lu}) \tag{3. 10}$$

Now, the statement of the problem can be formulated mathematically by: find the state variable $\boldsymbol{u}=\boldsymbol{u}(\boldsymbol{x})$, the state-variable gradient $\bar{\boldsymbol{\varepsilon}}=\bar{\boldsymbol{\varepsilon}}(\boldsymbol{x})$ and the body flux $\boldsymbol{\sigma}=\boldsymbol{\sigma}(\boldsymbol{x})$ that satisfies (3.4), (3.6)-(3.7) $\forall\boldsymbol{x}\in\operatorname{int}\Omega$ and the boundary conditions $\boldsymbol{u}(\boldsymbol{x})=\boldsymbol{u}^0(\boldsymbol{x})\ \forall\boldsymbol{x}\in\partial\Omega^u$ and $\boldsymbol{t}(\boldsymbol{x})=\begin{bmatrix} n_1\boldsymbol{I} & n_2\boldsymbol{I}\end{bmatrix}\sigma=\boldsymbol{t}^0(\boldsymbol{x})\ \ \forall\boldsymbol{x}\in\partial\Omega^t$.

3.3 Weak Formulation

The constitutive law established in a strong form (3.4) (i.e., in terms of partial differential equations) is then reformulated in a weak form well suited for the development of the scale boundary finite element equation presented further below. A standard weighted residual technique is adopted along with the integration by parts via the Gauss-divergence theorem to obtain the weak-form equation as follows.

By taking the inner product between (3.4) and any sufficiently smooth weight function $\boldsymbol{w}(\boldsymbol{x})=\{w_1(\boldsymbol{x})\ \ w_2(\boldsymbol{x})\ ...\ w_\Lambda(\boldsymbol{x})\}^T$ and then integrating the result over the body Ω, it leads to

$$\int_\Omega \boldsymbol{w}^T\boldsymbol{L}^T\boldsymbol{\sigma}dA+\int_\Omega \boldsymbol{w}^T\boldsymbol{b}dA=0 \tag{3. 11}$$

By applying the identity $(w_J\sigma_{\alpha J})_{,\alpha}=\boldsymbol{w}^T\boldsymbol{L}^T\sigma+(\boldsymbol{Lw})^T\sigma$ to the first integral of (3.11), it yields

$$\int_\Omega (\boldsymbol{Lw})^T\boldsymbol{\sigma}dA=\int_\Omega (w_J\sigma_{\alpha J})_{,\alpha}dA+\int_\Omega \boldsymbol{w}^T\boldsymbol{b}dA \tag{3. 12}$$

From two-dimensional Gauss-divergence theorem, the first integral on the right hand side of (3.12) can be replaced by the boundary integral and the final result is given by

$$\int_{\Omega}(\boldsymbol{Lw})^T\boldsymbol{\sigma}dA=\int_{\partial\Omega}w_J(\sigma_{\alpha J}n_\alpha)dl+\int_{\Omega}\boldsymbol{w}^T\boldsymbol{b}dA \tag{3. 13}$$

where dl is an infinitesimal arc length. By applying the relation (3.8) to the boundary term, it finally yields

$$\int_{\Omega}(\boldsymbol{Lw})^T\boldsymbol{\sigma}dA=\int_{\partial\Omega}\boldsymbol{w}^T\boldsymbol{t}dl+\int_{\Omega}\boldsymbol{w}^T\boldsymbol{b}dA \tag{3. 14}$$

It is worth noting that the resulting weak-form (3.14) for the special case of linear elasticity is in fact the principle of virtual work with $\boldsymbol{w}(\boldsymbol{x})$ denoting the virtual displacement field. By further replacing the body flux $\boldsymbol{\sigma}$ in (3.14) by that associated with the state variable via the relation (3.9), it leads to

$$\int_{\Omega}(\boldsymbol{Lw})^T\boldsymbol{D}(\boldsymbol{Lu})dA=\int_{\partial\Omega}\boldsymbol{w}^T\boldsymbol{t}dl+\int_{\Omega}\boldsymbol{w}^T\boldsymbol{b}dA \tag{3. 15}$$

It should be apparent from the above formulation that the weak-form equation (3.15) is valid for an arbitrary choice of the weight function $\boldsymbol{w}$. Only restriction placed to the weight function is the smoothness requirement to ensure the integrability of all integrals appearing in (3.15). This can be achieved by requiring the weight function and their first partial derivatives square integrable, i.e.

$$\int_{\Omega}\left[(\boldsymbol{Lw})^T(\boldsymbol{Lw})+\boldsymbol{w}^T\boldsymbol{w}\right]dA<\infty \tag{3. 16}$$

Now, let $\boldsymbol{W}$ be a space of all weight functions satisfying the condition (3.16). It can be readily verified that satisfaction of (3.4) and (3.9) $\forall\boldsymbol{x}\in\operatorname{int}\Omega$ implies the weak statement (3.15) $\forall\boldsymbol{w}\in\boldsymbol{W}$. The converse is also valid if the data of the problem such as $\boldsymbol{D}$ and the distributed body source $\boldsymbol{b}$ is sufficiently smooth. Now, the problem statement can be formulated in terms of a weak-form equation by: find the state variable $\boldsymbol{u}=\boldsymbol{u}(\boldsymbol{x})$ such that the weak-form equation (3.15) is satisfied $\forall\boldsymbol{w}\in\boldsymbol{W}$ and $\boldsymbol{u}(\boldsymbol{x})=\boldsymbol{u}^0(\boldsymbol{x})$ is satisfied $\forall\boldsymbol{x}\in\partial\Omega^u$ and $\boldsymbol{t}(\boldsymbol{x})=\left[n_1\boldsymbol{I}\quad n_2\boldsymbol{I}\right]\boldsymbol{D}(\boldsymbol{Lu})=\boldsymbol{t}^0(\boldsymbol{x})$ is satisfied $\forall\boldsymbol{x}\in\partial\Omega^t$.

3.4 Scaled Boundary Coordinate Transformation

Let $\boldsymbol{x}_0=(x_{10},x_{20})$ be a point in R^2 and C be a simple, piecewise smooth curve in R^2 parameterized by a function $\boldsymbol{r}:s\in[a,b]\rightarrow(x_{10}+\hat{x}_1(s),x_{20}+\hat{x}_2(s))\in\mathbb{R}^2$ as shown in Figure 3.2. Let $\theta(s)$ be the circumferential angle of a point $\boldsymbol{r}(s)$ on the curve C measured from a straight line passing to $\boldsymbol{x}_0$ and $\boldsymbol{r}(a)$ to a straight line passing to $\boldsymbol{x}_0$ and $\boldsymbol{r}(s)$ (see Figure 3.2). The simple curve C considered here can be either closed (i.e., $\boldsymbol{r}(a)=\boldsymbol{r}(b)$) or not closed (i.e., $\boldsymbol{r}(a)\neq\boldsymbol{r}(b)$) and, in addition, it must not contain the point $\boldsymbol{x}_0$ and satisfies the condition $\theta \in [0, 2\pi]$ and $d\theta / ds > 0 \;\; \forall s \in (a, b)$. Now, let us introduce the following coordinate transformation

$$\boldsymbol{x} = \boldsymbol{x}_0 + \xi \hat{\boldsymbol{x}}(s) \quad \text{or} \quad x_\alpha = x_{\alpha 0} + \xi \hat{x}_\alpha(s) \tag{3. 17}$$

where $\xi \geq 0$. It is evident from the coordinate transformation (3.17) that (i) any straight line $\xi = \xi_0, a \leq s \leq b$ in the $\xi - s$ plane is mapped to a curve S in the $x_1 - x_2$ plane which is simply a scaled version of the curve C about $\boldsymbol{x}_0$ and (ii) any straight line $\xi \geq 0, s = s_0 \in [a, b]$ in the $\xi - s$ plane is mapped to a semi-infinite straight line L in the $x_1 - x_2$ plane starting from $\boldsymbol{x}_0$ and passing through the point $\boldsymbol{r}(s_0)$ on the curve C (also see Figure 3.2). In addition, a straight line $\xi = 0, a \leq s \leq b$ in the $\xi - s$ plane is mapped to a single point $\boldsymbol{x}_0$ which is commonly termed the *scaling center* and a straight line $\xi = 1, a \leq s \leq b$ in the $\xi - s$ plane is mapped directly to the curve C which is termed the *defining curve*. The coordinates ξ and s are termed the *scale boundary coordinates*. Clearly, the transformation (3.17) simply maps the region $\xi \geq 0, a \leq s \leq b$ in the $\xi - s$ plane into a region in the $x_1 - x_2$ plane bounded by the two straight lines L_a and L_b (i.e., a shaded region shown in Figure 3.2).

It is apparent from the coordinate mapping (3.17) that the differential line $d\boldsymbol{\xi} = \{d\xi \;\; ds\}^T$ at any point (ξ, s) in the $\xi - s$ plane is related to the differential line $d\boldsymbol{x} = \{dx_1 \;\; dx_2\}^T$ at any point (x_1, x_2) in the $x_1 - x_2$ plane by

$$d\boldsymbol{x} = \boldsymbol{T} d\boldsymbol{\xi} \tag{3. 18}$$

where $\boldsymbol{T}$ is the Jacobian matrix of transformation given explicitly by

$$\boldsymbol{T} = \begin{bmatrix} \hat{x}_1 & \xi d\hat{x}_1 / ds \\ \hat{x}_2 & \xi d\hat{x}_2 / ds \end{bmatrix} \tag{3. 19}$$

The inverse relation of (3.18) is given by

$$d\boldsymbol{\xi} = \boldsymbol{T}^{-1} d\boldsymbol{x} = \boldsymbol{R} d\boldsymbol{x} \tag{3. 20}$$

where the matrix $\boldsymbol{R}$ is the inverse of the Jacobian matrix $\boldsymbol{T}$ given by

$$\boldsymbol{R} = \frac{1}{J} \begin{bmatrix} d\hat{x}_2 / ds & -d\hat{x}_1 / ds \\ -\hat{x}_2 / \xi & \hat{x}_1 / \xi \end{bmatrix} \tag{3. 21}$$

with J denoting

$$J = \hat{x}_1 \frac{d\hat{x}_2}{ds} - \hat{x}_2 \frac{d\hat{x}_1}{ds} \tag{3. 22}$$

By setting $d\boldsymbol{\xi} = (d\lambda)\boldsymbol{m}$ where $\boldsymbol{m}$ is a unit vector and $d\lambda$ is the length of $d\boldsymbol{\xi}$, it can be readily verified that the length of $d\boldsymbol{x}$, denoted by dl, is given by

$$dl = \sqrt{dx_\alpha dx_\alpha} = \sqrt{T_{\alpha\beta}T_{\alpha\gamma}m_\beta m_\gamma}\,d\lambda \tag{3. 23}$$

For following special cases (i) $\boldsymbol{m} = \{1\ 0\}^T$, $d\lambda = d\xi$ and (ii) $\boldsymbol{m} = \{0\ 1\}^T$, $d\lambda = ds$, the relation (3.23) reduces, respectively, to

$$dl = \sqrt{\hat{x}_1^2 + \hat{x}_2^2}\,d\xi = J^\xi(s)d\xi,\ \ J^\xi(s) = \sqrt{\hat{x}_1^2 + \hat{x}_2^2} \tag{3. 24}$$

$$dl = \sqrt{\left(d\hat{x}_1/ds\right)^2 + \left(d\hat{x}_2/ds\right)^2}\,\xi ds = J^s(s)\xi ds,\ \ J^s(s) = \sqrt{\left(d\hat{x}_1/ds\right)^2 + \left(d\hat{x}_2/ds\right)^2} \tag{3. 25}$$

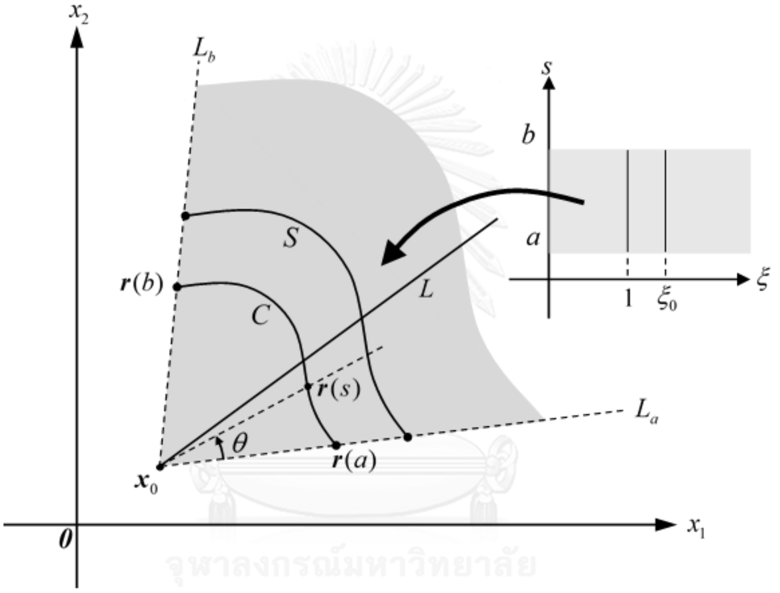

Figure 3.2: Schematic of a scaling center $\boldsymbol{x}_0$ and a defining curve C

Similarly, the differential area $d\xi ds$ at any point (ξ, s) in the $\xi - s$ plane can be related to the differential area dA at any point (x_1, x_2) in the $x_1 - x_2$ plane by

$$dA = J\xi d\xi ds \tag{3. 26}$$

From the chain rule for differentiations, the partial derivative of any function with respect to the coordinate x_α can be related to those with respect to ξ and s via the following relation

$$\begin{Bmatrix} \dfrac{\partial}{\partial x_1} \\ \dfrac{\partial}{\partial x_2} \end{Bmatrix} = \frac{1}{J}\begin{bmatrix} \dfrac{d\hat{x}_2}{ds} & -\hat{x}_2 \\ -\dfrac{d\hat{x}_1}{ds} & \hat{x}_1 \end{bmatrix}\begin{Bmatrix} \dfrac{\partial}{\partial \xi} \\ \dfrac{1}{\xi}\dfrac{\partial}{\partial s} \end{Bmatrix} \tag{3.27}$$

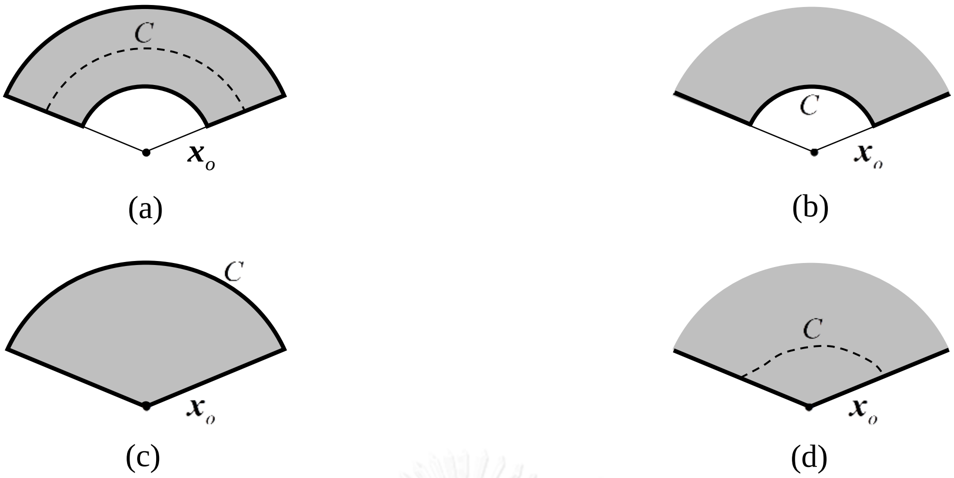

(a) (b)

(c) (d)

Figure 3.3: Examples of opened bodies: (a) bounded body containing no scaling center, (b) unbounded body containing no scaling center, (c) bounded body containing scaling center, and (d) unbounded body containing scaling center.

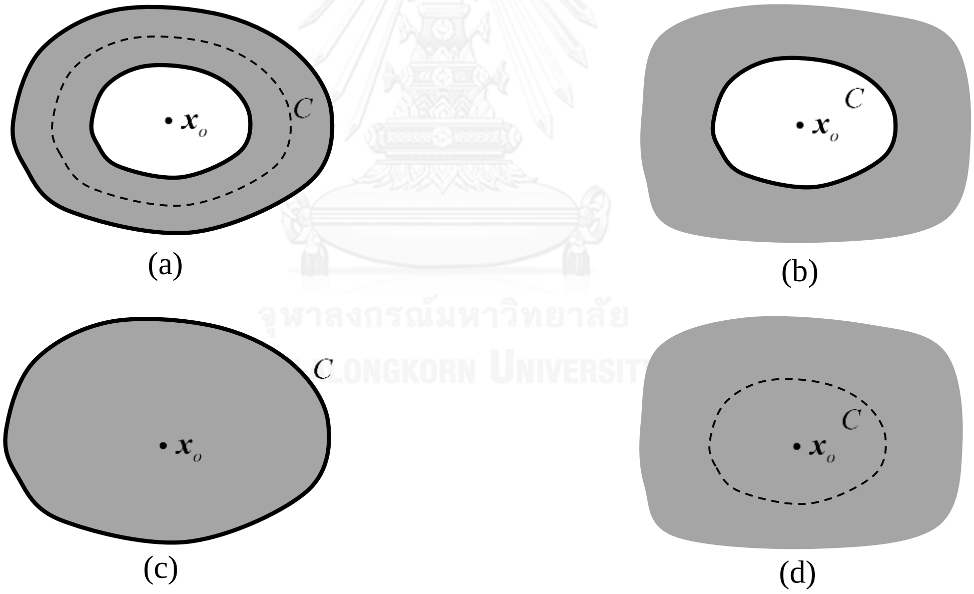

(a) (b)

(c) (d)

Figure 3.4: Examples of closed bodies: (a) bounded body containing a hole, (b) unbounded body containing a hole, (c) bounded body containing no hole, and (d) unbounded body containing no hole.

The linear differential operator $\boldsymbol{L}$ given by (3.5) can now be expressed in terms of partial derivatives with respect to ξ and s by

$$\boldsymbol{L} = \boldsymbol{b}_1 \frac{\partial}{\partial \xi} + \boldsymbol{b}_2 \frac{1}{\xi} \frac{\partial}{\partial s} \tag{3. 28}$$

where $\boldsymbol{b}_1$ and $\boldsymbol{b}_2$ are $2\Lambda \times \Lambda$ -matrices defined by

$$\boldsymbol{b}_1 = \frac{1}{J}\left(\frac{d\hat{x}_2}{ds}\boldsymbol{L}_1 - \frac{d\hat{x}_1}{ds}\boldsymbol{L}_2\right) = \frac{1}{J}\begin{bmatrix} \dfrac{d\hat{x}_2}{ds}\boldsymbol{I}_{\Lambda\times\Lambda} \\ -\dfrac{d\hat{x}_1}{ds}\boldsymbol{I}_{\Lambda\times\Lambda} \end{bmatrix} \tag{3. 29}$$

$$\boldsymbol{b}_2 = \frac{1}{J}\left(\hat{x}_1\boldsymbol{L}_2 - \hat{x}_2\boldsymbol{L}_1\right) = \frac{1}{J}\begin{bmatrix} -\hat{x}_2\boldsymbol{I}_{\Lambda\times\Lambda} \\ \hat{x}_1\boldsymbol{I}_{\Lambda\times\Lambda} \end{bmatrix} \tag{3. 30}$$

Now, it is ready to pose the restriction on the geometry of the body Ω considered in the present investigation. For a given body Ω, there must exist the scaling center $\boldsymbol{x}_0$ and the defining curve C such that there exists a region $[\xi_1,\xi_2]\times[s_1,s_2]$ in the $\xi - s$ plane that is mapped to the region Ω in the $x_1 - x_2$ plane via the coordinate transformation (3.17). If the defining curve C is not closed, the body is said to be *opened* and portions of the boundary $\partial\Omega$ associated with $s = s_1$ and $s = s_2$ are termed the *side face* (see Figure 3.3). If the defining curve is closed, the body is said to be closed and the boundary $\partial\Omega$ contains no side face (see Figure 3.4). If ξ_1 is finite, the body Ω is said to be bounded (see Figures 3.3(a), 3.3(c), 3.4(a), 3.4(c)); otherwise (i.e., $\xi_2 = \infty$), it is said to be unbounded (see Figures 3.3(b), 3.3(d), 3.4(b), 3.4(d)). If $\xi_1 = 0$, the body Ω contains the scaling center $\boldsymbol{x}_0$ (see Figures 3.3(c), 3.3(d), 3.4(c), 3.4(d)); otherwise (i.e., $\xi_1 > 0$), the body Ω does not contain the scaling center $\boldsymbol{x}_0$ (see Figures 3.3(a), 3.3(b), 3.4(c), 3.4(d)). Portions of the boundary $\partial\Omega$ associated with $\xi = \xi_1 > 0$ and $\xi = \xi_2 < \infty$ are termed the inner and outer boundaries, respectively. It is remarked that for an unbounded body with the scaling center located outside, the inner boundary is commonly chosen as the defining curve (i.e., $\xi_1 = 1$) whereas for a bounded body containing the scaling center, the outer boundary is chosen as the defining curve (i.e., $\xi_2 = 1$).

3.5 Scaled Boundary Finite Element Approximation

In this section, three approximations, one associated with the geometry of the defining curve and the other two corresponding to the field quantities and the weight function, are introduced. The defining curve C is discretized into n elements with the total m nodes. The coordinates of points on C, denoted by $\boldsymbol{x} = \boldsymbol{x}_0 + \hat{\boldsymbol{x}}(s)$, is approximated by

$$x_\alpha^h(s) = x_{\alpha 0} + \hat{x}_\alpha^h(s) = x_{\alpha 0} + \sum_{i=1}^{m}\phi_{(i)}(s)\hat{x}_{\alpha(i)} = x_{\alpha 0} + \boldsymbol{N}^G\boldsymbol{X}_\alpha \tag{3. 31}$$

where the superscript “ h ” is used to indicate the approximate quantities, $\phi_{(i)}(s)$ is the basis function associated with the i^{th} node, $\hat{x}_{\alpha(i)} = x_{\alpha(i)} - x_{\alpha 0}$ denotes the coordinate of the i^{th} node relative to the scaling center $\boldsymbol{x}_0$, $\boldsymbol{N}^G = \{\phi_{(1)} \quad \phi_{(2)} \quad \cdots \quad \phi_{(m)}\}^T$ stands for a row-matrix containing all nodal basis functions, and $\boldsymbol{X}_\alpha = \{\hat{x}_{\alpha(1)} \quad \hat{x}_{\alpha(2)} \quad \cdots \quad \hat{x}_{\alpha(m)}\}^T$ denotes a vector containing all nodal relative coordinates in which $\hat{x}_{\alpha(i)} = x_{\alpha(i)} - x_{\alpha 0}$ represents the coordinate of the i^{th} node relative to the scaling center $\boldsymbol{x}_0$. It should be remarked that the global nodal basis function $\phi_{(i)}(s)$ is constructed in a standard fashion by simply patching the local element shape functions associated with the i^{th} node and, as a result, it satisfies the Kronecker-delta property, i.e., $\phi_{(i)}(s_{(j)}) = \delta_{ij}$ where $s_{(j)}$ is the value of the boundary coordinate s of the j^{th} node and δ_{ij} denotes the Kronecker-delta symbol. The resulting discretized (or approximate) defining curve is denoted by C^h and the region in the $x_1 - x_2$ plane described by the discretized defining curve C^h is then used as the approximation for the geometry of the body Ω and denoted by Ω^h. With the relation (3.31), the derivative $d\hat{x}_\alpha / ds$ is then approximated by

$$\frac{d\hat{x}_\alpha^h}{ds} = \boldsymbol{B}^G \boldsymbol{X}_\alpha \tag{3. 32}$$

where $\boldsymbol{B}^G = d\boldsymbol{N}^G/ds = \{d\phi_{(1)}/ds \quad d\phi_{(2)}/ds \quad \cdots \quad d\phi_{(m)}/ds\}^T$. The approximations of J and the matrices $\boldsymbol{b}_1$ and $\boldsymbol{b}_2$ are given by

$$J^h = \boldsymbol{X}_1^T (\boldsymbol{N}^G)^T \boldsymbol{B}^G \boldsymbol{X}_2 - \boldsymbol{X}_2^T (\boldsymbol{N}^G)^T \boldsymbol{B}^G \boldsymbol{X}_1 \tag{3. 33}$$

$$J^{\xi h} = \sqrt{\boldsymbol{X}_1^T (\boldsymbol{N}^G)^T \boldsymbol{N}^G \boldsymbol{X}_1 + \boldsymbol{X}_2^T (\boldsymbol{N}^G)^T \boldsymbol{N}^G \boldsymbol{X}_2} \tag{3. 34}$$

$$J^{sh} = \sqrt{\boldsymbol{X}_1^T (\boldsymbol{B}^G)^T \boldsymbol{B}^G \boldsymbol{X}_1 + \boldsymbol{X}_2^T (\boldsymbol{B}^G)^T \boldsymbol{B}^G \boldsymbol{X}_2} \tag{3. 35}$$

$$\boldsymbol{b}_1^h = \frac{1}{J}\begin{bmatrix} \boldsymbol{B}^G \boldsymbol{X}_2 \boldsymbol{I}_{\Lambda\times\Lambda} \\ -\boldsymbol{B}^G \boldsymbol{X}_1 \boldsymbol{I}_{\Lambda\times\Lambda} \end{bmatrix} \tag{3. 36}$$

$$\boldsymbol{b}_2^h = \frac{1}{J}\begin{bmatrix} -\boldsymbol{N}^G \boldsymbol{X}_2 \boldsymbol{I}_{\Lambda\times\Lambda} \\ \boldsymbol{N}^G \boldsymbol{X}_1 \boldsymbol{I}_{\Lambda\times\Lambda} \end{bmatrix} \tag{3. 37}$$

The approximate linear differential operator $\boldsymbol{L}$ is then given by

$$\boldsymbol{L}^h = \boldsymbol{b}_1^h \frac{\partial}{\partial \xi} + \boldsymbol{b}_2^h \frac{1}{\xi}\frac{\partial}{\partial s} \tag{3. 38}$$

From the coordinate transformation (3.17) along with the approximation (3.31), the state variable $\boldsymbol{u}$ is now approximated by $\boldsymbol{u}^h$ in a form

$$\boldsymbol{u}^h = \boldsymbol{u}^h(\xi,s) = \sum_{i=1}^{m} \phi_{(i)}(s)\boldsymbol{u}^h_{(i)}(\xi) = \boldsymbol{N}^S \boldsymbol{U}^h \tag{3. 39}$$

where $\boldsymbol{u}^h_{(i)}(\xi)$ denotes the value of the state variable along the line $s = s_{(i)}$ (i.e., a line passing through the scaling center and the *i*th node), $\boldsymbol{N}^S = \left\{\phi_{(1)}\boldsymbol{I}_{\Lambda\times\Lambda} \quad \phi_{(2)}\boldsymbol{I}_{\Lambda\times\Lambda} \cdots \phi_{(m)}\boldsymbol{I}_{\Lambda\times\Lambda}\right\}$ is a $\Lambda \times m\Lambda$-matrix containing all basis functions, and $\boldsymbol{U}^h = \left\{\boldsymbol{u}^h_{(1)}(\xi) \quad \boldsymbol{u}^h_{(2)}(\xi) \cdots \boldsymbol{u}^h_{(m)}(\xi)\right\}^T$,and $\boldsymbol{W}^h = \left\{\boldsymbol{w}^h_{(1)}(\xi) \cdots \boldsymbol{w}^h_{(m)}(\xi)\right\}^T$ denote vectors containing all functions $\boldsymbol{u}^h_{(i)}(\xi)$ and $\boldsymbol{w}^h_{(i)}(\xi)$, respectively. The approximation of the body flux $\boldsymbol{\sigma}$ at any point $\boldsymbol{x} \in \Omega^h$ in the $x_1 - x_2$ plane (or at any corresponding point (ξ, s) in the $\xi - s$ plane), denoted by $\boldsymbol{\sigma}^h$, can be obtained directly by substituting (3.39) into the relation (3.9) along with the approximation (3.38) and the final result is given by

$$\sigma^h = \sigma^h(\xi,s) = \boldsymbol{D}(\boldsymbol{L}^h\boldsymbol{u}^h) = \boldsymbol{D}\left[\boldsymbol{b}_1^h \frac{\partial}{\partial\xi} + \boldsymbol{b}_2^h \frac{1}{\xi}\frac{\partial}{\partial s}\right](\boldsymbol{N}^S\boldsymbol{U}^h) = \boldsymbol{D}\left[\boldsymbol{B}_1\boldsymbol{U}^h_{,\xi} + \frac{1}{\xi}\boldsymbol{B}_2\boldsymbol{U}^h\right] \tag{3. 40}$$

where $\boldsymbol{B}_1$ and $\boldsymbol{B}_2$ are given by

$$\boldsymbol{B}_1 = \boldsymbol{b}_1^h \boldsymbol{N}^S \tag{3. 41}$$

$$\boldsymbol{B}_2 = \boldsymbol{b}_2^h \boldsymbol{B}^S \tag{3. 42}$$

where $\boldsymbol{B}^S = d\boldsymbol{N}^S/ds = \{d\phi_{(1)}/ds\boldsymbol{I}_{\Lambda\times\Lambda} \quad d\phi_{(2)}/ds\boldsymbol{I}_{\Lambda\times\Lambda} \quad \cdots \quad d\phi_{(m)}/ds\,\boldsymbol{I}_{\Lambda\times\Lambda}\}$. It is evident that both the matrices $\boldsymbol{B}_1$ and $\boldsymbol{B}_2$ are independent of the coordinate ξ. Similarly, the weight function $\boldsymbol{w}$ and its derivatives $\boldsymbol{Lw}$ can be approximated, in a similar fashion, by

$$\boldsymbol{w}^h = \boldsymbol{w}^h(\xi,s) = \sum_{i=1}^{m} \phi_{(i)}(s)\boldsymbol{w}^h_{(i)}(\xi) = \boldsymbol{N}^S \boldsymbol{W}^h \tag{3. 43}$$

$$\boldsymbol{L}^h\boldsymbol{w}^h = \boldsymbol{L}^h\boldsymbol{w}^h(\xi,s) = \left[\boldsymbol{b}_1^h \frac{\partial}{\partial\xi} + \boldsymbol{b}_2^h \frac{1}{\xi}\frac{\partial}{\partial s}\right](\boldsymbol{N}^S\boldsymbol{W}^h) = \left[\boldsymbol{B}_1\boldsymbol{W}^h_{,\xi} + \frac{1}{\xi}\boldsymbol{B}_2\boldsymbol{W}^h\right] \tag{3. 44}$$

where $\boldsymbol{w}^h_{(i)}(\xi)$ denotes an arbitrary function of the coordinate ξ along the line $s = s_{(i)}$ and $\boldsymbol{W}^h = \left\{\boldsymbol{w}^h_{(1)}(\xi)\,\boldsymbol{w}^h_{(2)}(\xi) \cdots \boldsymbol{w}^h_{(m)}(\xi)\right\}^T$ is a vector containing all functions $\boldsymbol{w}^h_{(i)}(\xi)$.

3.6 Scaled Boundary Finite Element Equations

In this section, a set of scaled boundary finite element equations is established for a generic, two-dimensional body Ω as shown in Figure 3.5. The boundary of the domain $\partial\Omega$ is assumed consisting of four parts resulting from the scale boundary coordinate transformation with the scaling center $\boldsymbol{x}_0$ and defining curve C: the inner boundary

$\partial\Omega_1$, the outer boundary $\partial\Omega_2$, the side-face-1 $\partial\Omega_1^s$, and the side-face-2 $\partial\Omega_2^s$. The body is considered in this general setting to ensure that the resulting formulation is applicable to various cases. For certain special cases such as closed bodies without the side face, bodies containing the scaling center, and unbounded bodies, it simply takes $\partial\Omega_1^s = \partial\Omega_2^s = \varnothing$, $\partial\Omega_1^s = \varnothing$, and $\partial\Omega_2^s = \varnothing$, respectively, in the following formulation. The approximation of the given body Ω is achieved via the discretization of the defining curve C^h along with the mapping region $[\xi_1, \xi_2] \times [s_1, s_2]$ in the $\xi - s$ plane and the approximate body is denoted by Ω^h. In particular, the approximate inner boundary $\partial\Omega_1^h$, the approximate outer boundary $\partial\Omega_2^h$, the side-face-1 $\partial\Omega_1^s$, and the side-face-2 $\partial\Omega_2^s$ are fully described by a curve $\xi = \xi_1, s_1 \le s \le s_2$, a curve $\xi = \xi_2, s_1 \le s \le s_2$, a straight line $s = s_1, \xi_1 \le \xi \le \xi_2$, and a straight line $s = s_2, \xi_1 \le \xi \le \xi_2$, respectively.

As a result of the boundary partition $\partial\Omega = \partial\Omega_1 \cup \partial\Omega_2 \cup \partial\Omega_1^s \cup \partial\Omega_1^s$, the weak-form equation (3.15) can be rewritten for the generic body Ω as

$$\int_{\Omega} (\boldsymbol{Lw})^{\boldsymbol{T}} \boldsymbol{D}(\boldsymbol{Lu}) \boldsymbol{dA} = \int_{\partial\Omega_1} \boldsymbol{w}^{\boldsymbol{T}} \boldsymbol{tdl} + \int_{\partial\Omega_2} \boldsymbol{w}^{\boldsymbol{T}} \boldsymbol{tdl} + \int_{\partial\Omega_1^s} \boldsymbol{w}^{\boldsymbol{T}} \boldsymbol{tdl} + \int_{\partial\Omega_1^s} \boldsymbol{w}^{\boldsymbol{T}} \boldsymbol{tdl} + \int_{\Omega} \boldsymbol{w}^{\boldsymbol{T}} \boldsymbol{bdA} \tag{3. 45}$$

By changing to the $\boldsymbol{\xi}, \boldsymbol{s}$-coordinates via the transformation (3.17) and using the relations (3.24)-(3.26), the weak-form (3.45) becomes

$$\begin{aligned} \int_{s_1}^{s_2}\int_{\xi_1}^{\xi_2} (\boldsymbol{Lw})^T \boldsymbol{D}(\boldsymbol{Lu}) J\xi d\xi ds = \int_{s_1}^{s_2}\int_{\xi_1}^{\xi_2} \boldsymbol{w}^T \boldsymbol{b} J\xi d\xi ds + \int_{s_1}^{s_2} \boldsymbol{w}_1^T \boldsymbol{t}_1(s) J^s(s)\xi_1 ds + \int_{s_1}^{s_2} \boldsymbol{w}_2^T \boldsymbol{t}_2(s) J^s(s)\xi_2 ds \\ + \int_{\xi_1}^{\xi_2} (\boldsymbol{w}_1^s)^T \boldsymbol{t}_1^s(\xi) J_1^\xi d\xi + \int_{\xi_1}^{\xi_2} (\boldsymbol{w}_2^s)^T \boldsymbol{t}_2^s(\xi) J_2^\xi d\xi \end{aligned} \tag{3. 46}$$

where $\boldsymbol{w}_1$, $\boldsymbol{w}_2$, $\boldsymbol{w}_1^s, \boldsymbol{w}_2^s$ are restrictions of the weight function $\boldsymbol{w}$ on the boundaries $\partial\Omega_1, \partial\Omega_2, \partial\Omega_1^s, \partial\Omega_2^s$, respectively; t_1, t_2, t_1^s, t_2^s are surface flux on the boundaries $\partial\Omega_1$, $\partial\Omega_2, \partial\Omega_1^s, \partial\Omega_2^s$, respectively; and $J_1^\xi = J_\xi(s_1)$, $J_2^\xi = J_\xi(s_2)$. Next, by introducing the approximations of the body flux (3.40) and the derivatives of the weight function (3.44) along with the domain approximation, the integral on the left-hand side of (3.46), denoted for convenience by $\mathscr{I}_1$, becomes

$$\mathscr{I}_1 = \int_{s_1}^{s_2}\int_{\xi_1}^{\xi_2} \left[\boldsymbol{B}_1 \boldsymbol{W}_{,\xi}^h \frac{\partial}{\partial\xi} + \frac{1}{\xi} \boldsymbol{B}_2 \boldsymbol{W}^h \right]^T \boldsymbol{D} \left[\boldsymbol{B}_1 \boldsymbol{U}_{,\xi}^h + \frac{1}{\xi} \boldsymbol{B}_2 \boldsymbol{U}^h \right] J^h \xi d\xi ds \tag{3. 47}$$

By manipulating the involved matrix algebra, $\mathscr{I}_1$ can be expressed as

$$\mathscr{J}_1 = \int_{s_1}^{s_2}\int_{\xi_1}^{\xi_2} (\boldsymbol{W}^h_{,\xi})^T \boldsymbol{B}_1^T \boldsymbol{D}\boldsymbol{B}_1 \boldsymbol{U}^h_{,\xi} J^h \xi \, d\xi ds + \int_{s_1}^{s_2}\int_{\xi_1}^{\xi_2} (\boldsymbol{W}^h_{,\xi})^T \boldsymbol{B}_1^T \boldsymbol{D}\boldsymbol{B}_2 \boldsymbol{U}^h J^h d\xi ds$$
$$+ \int_{s_1}^{s_2}\int_{\xi_1}^{\xi_2} (\boldsymbol{W}^h)^T \boldsymbol{B}_2^T \boldsymbol{D}\boldsymbol{B}_1 \boldsymbol{U}^h_{,\xi} J^h d\xi ds + \int_{s_1}^{s_2}\int_{\xi_1}^{\xi_2} (\boldsymbol{W}^h)^T \boldsymbol{B}_2^T \boldsymbol{D}\boldsymbol{B}_2 \boldsymbol{U}^h \frac{J^h}{\xi} d\xi ds \qquad (3.\ 48)$$

Further integrating the first two integrals by parts with respect to the coordinate ξ results in

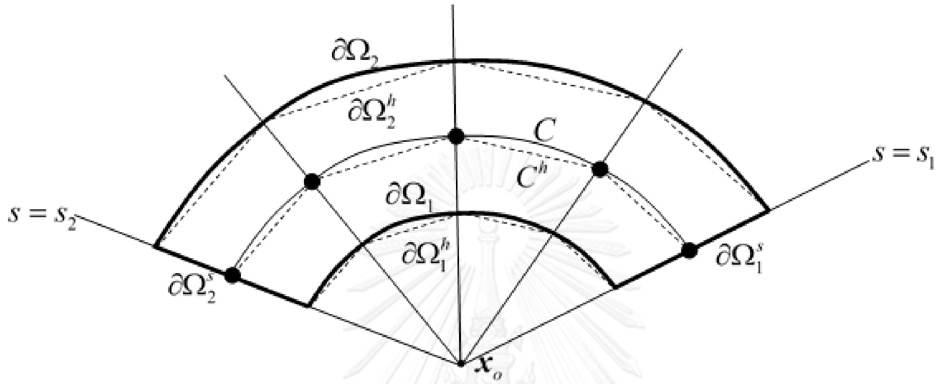

Figure 3.5: Schematic of a generic body Ω and its approximation Ω^h. The dashed lines are used to represent the approximation of the defining curve, the inner boundary and the outer boundary.

$$\mathscr{J}_1 = -\int_{s_1}^{s_2}\int_{\xi_1}^{\xi_2} (\boldsymbol{W}^h)^T \boldsymbol{B}_1^T \boldsymbol{D}\boldsymbol{B}_1 (\xi \boldsymbol{U}^h_{,\xi})_{,\xi} J^h d\xi ds - \int_{s_1}^{s_2}\int_{\xi_1}^{\xi_2} (\boldsymbol{W}^h)^T \boldsymbol{B}_1^T \boldsymbol{D}\boldsymbol{B}_2 \boldsymbol{U}^h_{,\xi} J^h d\xi ds$$
$$+ \int_{s_1}^{s_2}\int_{\xi_1}^{\xi_2} (\boldsymbol{W}^h)^T \boldsymbol{B}_2^T \boldsymbol{D}\boldsymbol{B}_1 \boldsymbol{U}^h_{,\xi} J^h d\xi ds + \int_{s_1}^{s_2}\int_{\xi_1}^{\xi_2} (\boldsymbol{W}^h)^T \boldsymbol{B}_2^T \boldsymbol{D}\boldsymbol{B}_2 \boldsymbol{U}^h \frac{J^h}{\xi} d\xi ds$$
$$+ \int_{s_1}^{s_2} (\boldsymbol{W}_2^h)^T \boldsymbol{B}_1^T \boldsymbol{D}\boldsymbol{B}_1 \boldsymbol{U}^h_{,\xi}\Big|_{\xi=\xi_2} \xi_2 J^h ds - \int_{s_1}^{s_2} (\boldsymbol{W}_1^h)^T \boldsymbol{B}_1^T \boldsymbol{D}\boldsymbol{B}_1 \boldsymbol{U}^h_{,\xi}\Big|_{\xi=\xi_1} \xi_1 J^h ds \qquad (3.\ 49)$$
$$+ \int_{s_1}^{s_2} (\boldsymbol{W}_2^h)^T \boldsymbol{B}_1^T \boldsymbol{D}\boldsymbol{B}_2 \boldsymbol{U}^h\Big|_{\xi=\xi_2} J^h ds - \int_{s_1}^{s_2} (\boldsymbol{W}_1^h)^T \boldsymbol{B}_1^T \boldsymbol{D}\boldsymbol{B}_2 \boldsymbol{U}^h\Big|_{\xi=\xi_1} J^h d$$

where $\boldsymbol{W}_1^h = \boldsymbol{W}^h(\xi = \xi_1)$ and $\boldsymbol{W}_2^h = \boldsymbol{W}^h(\xi = \xi_2)$. By recalling that the matrices $\boldsymbol{B}_1$ and $\boldsymbol{B}_2$ are independent of the coordinate ξ, $\boldsymbol{W}^h$ and $\boldsymbol{U}^h$ are independent of the coordinate s, and the matrix $\boldsymbol{D}$ is independent of both ξ and s, the integral $\mathscr{J}_1$ is simplified to

$$\begin{aligned}\mathcal{I}_1 = &\int_{\xi_1}^{\xi_2} (\boldsymbol{W}^h)^T \left[-\xi \boldsymbol{E}_0 \boldsymbol{U}^h_{,\xi\xi} + (\boldsymbol{E}_1 - \boldsymbol{E}_1^T - \boldsymbol{E}_0)\boldsymbol{U}^h_{,\xi} + \frac{1}{\xi}\boldsymbol{E}_2 \boldsymbol{U}^h \right] d\xi \\ &+ (\boldsymbol{W}_2^h)^T \left\{ \xi \boldsymbol{E}_0 \boldsymbol{U}^h_{,\xi} + \boldsymbol{E}_1^T \boldsymbol{U}^h \right\}_{\xi=\xi_2} - (\boldsymbol{W}_1^h)^T \left\{ \xi \boldsymbol{E}_0 \boldsymbol{U}^h_{,\xi} + \boldsymbol{E}_1^T \boldsymbol{U}^h \right\}_{\xi=\xi_1}\end{aligned} \tag{3. 50}$$

where the matrices $\boldsymbol{E}_0$, $\boldsymbol{E}_1$ and $\boldsymbol{E}_2$ are defined by

$$\boldsymbol{E}_0 = \int_{s_1}^{s_2} \boldsymbol{B}_1^T \boldsymbol{D} \boldsymbol{B}_1 J^h ds \tag{3. 51}$$

$$\boldsymbol{E}_1 = \int_{s_1}^{s_2} \boldsymbol{B}_2^T \boldsymbol{D} \boldsymbol{B}_1 J^h ds \tag{3. 52}$$

$$\boldsymbol{E}_2 = \int_{s_1}^{s_2} \boldsymbol{B}_2^T \boldsymbol{D} \boldsymbol{B}_2 J^h ds \tag{3. 53}$$

It is evident from (3.51) and (3.53) that both matrices $\boldsymbol{E}_0$ and $\boldsymbol{E}_2$ are symmetric, i.e., $(\boldsymbol{E}_0)^T = \boldsymbol{E}_0$ and $(\boldsymbol{E}_2)^T = \boldsymbol{E}_2$. Now, the boundary integrals appearing on the right-hand side of (3.46), denoted for convenience by $\mathcal{I}_2$, can also be approximated by

$$\begin{aligned}\mathcal{I}_2 = &(\boldsymbol{W}_1^h)^T \int_{s_1}^{s_2} (\boldsymbol{N}^S)^T \boldsymbol{t}_1(s) \xi_1 J^{sh}(s) ds + (\boldsymbol{W}_2^h)^T \int_{s_1}^{s_2} (\boldsymbol{N}^S)^T \boldsymbol{t}_2(s) \xi_2 J^{sh}(s) ds \\ &+ \int_{\xi_1}^{\xi_2} (\boldsymbol{W}^h)^T (\boldsymbol{N}_1^S)^T \boldsymbol{t}_1^s(\xi) J_1^{\xi h} d\xi + \int_{\xi_i}^{\xi_o} (\boldsymbol{W}^h)^T (\boldsymbol{N}_2^S)^T \boldsymbol{t}_2^s(\xi) J_2^{\xi h} d\xi\end{aligned} \tag{3. 54}$$

where $\boldsymbol{N}_1^S = \boldsymbol{N}^S(s = s_1)$ and $\boldsymbol{N}_2^S = \boldsymbol{N}^S(s = s_2)$. By defining the following quantities

$$\boldsymbol{P}_1 = \int_{s_1}^{s_2} (\boldsymbol{N}^S)^T \boldsymbol{t}_1(s) \xi_1 J^{sh}(s) ds \tag{3. 55}$$

$$\boldsymbol{P}_2 = \int_{s_1}^{s_2} (\boldsymbol{N}^S)^T \boldsymbol{t}_2(s) \xi_2 J^{sh}(s) ds \tag{3. 56}$$

$$\boldsymbol{F}_1^t = \boldsymbol{F}_1^t(\xi) = (\boldsymbol{N}_1^S)^T \boldsymbol{t}_1^s(\xi) J_1^{\xi h} \tag{3. 57}$$

$$\boldsymbol{F}_2^t = \boldsymbol{F}_2^t(\xi) = (\boldsymbol{N}_2^S)^T \boldsymbol{t}_2^s(\xi) J_2^{\xi h} \tag{3. 58}$$

the integral $\mathcal{I}_2$ now becomes

$$\mathcal{I}_2 = (\boldsymbol{W}_1^h)^T \boldsymbol{P}_1 + (\boldsymbol{W}_2^h)^T \boldsymbol{P}_2 + \int_{\xi_1}^{\xi_2} (\boldsymbol{W}^h)^T \boldsymbol{F}_1^h d\xi + \int_{\xi_1}^{\xi_2} (\boldsymbol{W}^h)^T \boldsymbol{F}_2^h d\xi \tag{3. 59}$$

Without loss of generality, the *first* node and the *last* node resulting from the discretization of opened bodies are taken as a node on the side-face-1 and a node on the side-face-2, respectively, and this applies in what follows. It should be remarked from the Kronecker property of the nodal basis functions that $\phi_{(1)}(s_1)=1$, $\phi_{(j)}(s_1)=0\ \forall j\geq 2$ and $\phi_{(m)}(s_2)=1$, $\phi_{(j)}(s_2)=0\ \forall j\leq m-1$. Now, both the matrices $\boldsymbol{N}_1^S$ and $\boldsymbol{N}_2^S$ clearly contain many zero entries and simply take the form

$$\boldsymbol{N}_1^S=\{\boldsymbol{I}_{\Lambda\times\Lambda}\quad \boldsymbol{0}_{\Lambda\times\Lambda}\quad \cdots\quad \boldsymbol{0}_{\Lambda\times\Lambda}\} \tag{3. 60}$$

$$\boldsymbol{N}_2^S=\{\boldsymbol{0}_{\Lambda\times\Lambda}\quad \boldsymbol{0}_{\Lambda\times\Lambda}\quad \cdots\quad \boldsymbol{I}_{\Lambda\times\Lambda}\} \tag{3. 61}$$

Substituting (3. 60) into (3. 57) and (3. 61) into (3. 58) leads to

$$\boldsymbol{F}_1^t=\boldsymbol{F}_1^t(\xi)=\{J_1^{\xi h}\boldsymbol{t}_1^s(\xi)\quad \boldsymbol{0}\quad \cdots\quad \boldsymbol{0}\}^T \tag{3. 62}$$

$$\boldsymbol{F}_2^t=\boldsymbol{F}_2^t(\xi)=\{\boldsymbol{0}\quad \boldsymbol{0}\quad \cdots\quad J_2^{\xi h}\boldsymbol{t}_2^s(\xi)\}^T \tag{3. 63}$$

where $\boldsymbol{0}$ is a zero Λ-component vector. Finally, the domain integral associated with the distributed body source on the right-hand side of (3. 46), denoted by $\mathscr{J}_3$ can be approximated by

$$\mathscr{J}_3=\int_{s_1}^{s_2}\int_{\xi_1}^{\xi_2}(\boldsymbol{N}^S\boldsymbol{W}^h)^T\boldsymbol{b}J^h\xi d\xi ds=\int_{\xi_1}^{\xi_2}(\boldsymbol{W}^h)^T\xi\boldsymbol{F}^b d\xi \tag{3. 64}$$

where the matrix $\boldsymbol{F}^b$ is defined by

$$\boldsymbol{F}^b=\boldsymbol{F}^b(\xi)=\int_{s_1}^{s_2}(\boldsymbol{N}^S)^T\boldsymbol{b}Jds=\left\{\int_{s_1}^{s_2}\phi_{(1)}\boldsymbol{b}J^h ds\quad \int_{s_1}^{s_2}\phi_{(2)}\boldsymbol{b}J^h ds\quad \cdots\quad \int_{s_1}^{s_2}\phi_{(m)}\boldsymbol{b}J^h ds\right\}^T \tag{3. 65}$$

By combing the results (3.50), (3.59) and (3.64), the weak-form (3.46) is approximated by

$$\begin{aligned}&\int_{\xi_1}^{\xi_2}(\boldsymbol{W}^h)^T\left[-\xi\boldsymbol{E}_0\boldsymbol{U}^h_{,\xi\xi}+(\boldsymbol{E}_1-\boldsymbol{E}_1^T-\boldsymbol{E}_0)\boldsymbol{U}^h_{,\xi}+\frac{1}{\xi}\boldsymbol{E}_2\boldsymbol{U}^h-\boldsymbol{F}_t-\xi\boldsymbol{F}_b\right]d\xi\\ &+(\boldsymbol{W}_2^h)^T\left[\left\{\xi\boldsymbol{E}_0\boldsymbol{U}^h_{,\xi}+\boldsymbol{E}_1^T\boldsymbol{U}^h\right\}_{\xi=\xi_2}-\boldsymbol{P}_2\right]-(\boldsymbol{W}_1^h)^T\left[\left\{\xi\boldsymbol{E}_0\boldsymbol{U}^h_{,\xi}+\boldsymbol{E}_1^T\boldsymbol{U}^h\right\}_{\xi=\xi_1}+\boldsymbol{P}_1\right]=0\end{aligned} \tag{3. 66}$$

where $\boldsymbol{F}^t=\boldsymbol{F}_1^t+\boldsymbol{F}_2^t$. From the arbitrariness of the weight function $\boldsymbol{W}^h$, it can be deduced that

$$\xi^2\boldsymbol{E}_0\boldsymbol{U}^h_{,\xi\xi}+\xi(\boldsymbol{E}_0+\boldsymbol{E}_1^T-\boldsymbol{E}_1)\boldsymbol{U}^h_{,\xi}-\boldsymbol{E}_2\boldsymbol{U}^h+\xi\boldsymbol{F}^t+\xi^2\boldsymbol{F}^b=\boldsymbol{0}\quad \forall\xi\in(\xi_1,\xi_2) \tag{3. 67}$$

$$\boldsymbol{Q}^h(\xi_2)=\boldsymbol{P}_2 \tag{3. 68}$$

$$\boldsymbol{Q}^h(\xi_1) = -\boldsymbol{P}_1 \tag{3. 69}$$

where the vector $\boldsymbol{Q}^h = \boldsymbol{Q}^h(\xi)$ commonly known as the nodal internal flux is defined by

$$\boldsymbol{Q}^h(\xi) = \xi \boldsymbol{E}_0 \boldsymbol{U}^h_{,\xi} + \boldsymbol{E}_1^T \boldsymbol{U}^h \tag{3. 70}$$

Equations (3.67)-(3.69) form a set of the so-called scaled boundary finite element equations governing the function $\boldsymbol{U}^h = \boldsymbol{U}^h(\xi)$. It can be remarked that (3.67) forms a system of linear, second-order, nonhomogeneous, ordinary differential equations with respect to the coordinate ξ whereas (3.68) and (3.69) pose the boundary conditions on the inner and outer boundaries of the body. As previously pointed out, the governing equations (3.67)-(3.69) are formulated in a general context; as a result, for certain special cases, some terms or equations must be eliminated properly. For instances, the boundary condition (3.68) is ignored for unbounded bodies; the boundary condition (3.69) is ignored for bounded bodies containing the scaling center; the term $\boldsymbol{F}^t$ vanishes for closed bodies; and the term $\boldsymbol{F}^b$ vanishes for bodies free of distributed body source.

Now, the statement of an approximate problem can be formulated as follows: find the function $\boldsymbol{U}^h = \boldsymbol{U}^h(\xi)$ such that a system of linear ordinary differential equations (3.67) is satisfied $\forall \xi \in (\xi_1, \xi_2)$ and boundary conditions (3.68) and (3.69) are satisfied.

3.7 Treatment of Prescribed Conditions on Side Faces

It should be evident from (3.67)-(3.69) that the information associated with the prescribed distributed body source and the prescribed boundary conditions on both inner and outer boundaries can be integrated into the formulation via the term $\boldsymbol{F}^b$ and the conditions (3.68) and (3.69), respectively. However, the consideration of the prescribed conditions (either the surface flux or state variable) on the side face is still not apparent from the current formulation. To circumvent this situation, the system of linear differential equations (3.67) is further re-expressed in a form well-suited for the treatment of the prescribed state variable and surface flux on the side face.

First, bodies considered in the present investigation can be divided into five groups as follows: *Group*-1 corresponding to closed bodies without the side-face, *Group*-2 corresponding to opened bodies with prescribed surface flux on both side faces, *Group*-3 corresponding to opened bodies with prescribed surface flux on the side-face-1 and prescribed state variable on the side-face-2, *Group*-4 corresponding to opened bodies with prescribed surface flux on the side-face-2 and prescribed state variable on the side-face-1, and *Group*-5 corresponding to opened bodies with prescribed state variable on both side faces. It should be evident that for bodies in *Group*-1, $\boldsymbol{U}^h$ contains only unknown functions and $\boldsymbol{t}_1^s$, $\boldsymbol{t}_2^s$ do not exist or, equivalently, vanish; for bodies in *Group*-2, $\boldsymbol{U}^h$ contains only unknown functions and $\boldsymbol{t}_1^s$, $\boldsymbol{t}_2^s$ are fully prescribed; for bodies in *Group*-3, $\boldsymbol{t}_1^s$ and $\boldsymbol{u}_{(m)}^h(\xi)$ are fully prescribed and $\boldsymbol{t}_2^s$ and the remaining functions $\boldsymbol{u}_{(i)}^h(\xi)\ \forall i \le m-1$ in $\boldsymbol{U}^h$ are unknown; for bodies in *Group*-4, $\boldsymbol{t}_2^s$ and $\boldsymbol{u}_{(1)}^h(\xi)$ are fully prescribed and $\boldsymbol{t}_1^s$, and the remaining functions $\boldsymbol{u}_{(i)}^h(\xi)\ \forall i \ge 2$ in $\boldsymbol{U}^h$ are unknown; and for bodies in *Group*-5, both $\boldsymbol{u}_{(1)}^h(\xi)$ and $\boldsymbol{u}_{(m)}^h(\xi)$ are fully prescribed whereas $\boldsymbol{t}_1^s$, $\boldsymbol{t}_2^s$, and the remaining functions $\boldsymbol{u}_{(i)}^h(\xi)\ \forall 2 \le i \le m-1$ in $\boldsymbol{U}^h$ are unknown. To treat the prescribed conditions on the side-face for all groups of bodies as a whole, the vector $\boldsymbol{U}^h$ is first partitioned and rearranged into known and unknown parts as $\boldsymbol{U}^h = \{\boldsymbol{U}^{hu} \quad \boldsymbol{U}^{hc}\}^T$ where $\boldsymbol{U}^{hu} = \boldsymbol{U}^{hu}(\xi)$ contains only unknown functions from a collection $\boldsymbol{u}_{(i)}^h(\xi), i = 1, 2, ..., m$ and $\boldsymbol{U}^{hc} = \boldsymbol{U}^{hc}(\xi)$ contains the remaining known functions associated with the prescribed state variable on the side face. By denoting p the number of known functions $\boldsymbol{u}_{(i)}^h(\xi)$ contained in $\boldsymbol{U}^{hc}$, the number of remaining unknown functions $\boldsymbol{u}_{(i)}^h(\xi)$ contained in $\boldsymbol{U}^{hu}$ is then equal to $m-p$. Clearly, the value of p associated with bodies in *Group*-1, *Group*-2, *Group*-3, *Group*-4, and *Group*-5 are 0, 0, 1, 1, and 2 respectively. Consistent with the partition of the vector $\boldsymbol{U}^h$, the vector $\boldsymbol{F}^t$ can also be partitioned into $\boldsymbol{F}^t = \{\boldsymbol{F}^{tu} \quad \boldsymbol{F}^{tc}\}^T$ where $\boldsymbol{F}^{tu} = \boldsymbol{F}^{tu}(\xi)$ contains many $\boldsymbol{0}$ functions and known functions associated with prescribed surface flux on the side face and has the same dimension as that of $\boldsymbol{U}^{hu}$ and $\boldsymbol{F}^{tc} = \boldsymbol{F}^{tc}(\xi)$ contains unknown functions associated with the unknown surface flux on the side face and has the same dimension as that of $\boldsymbol{U}^{hc}$. According to the this partition, the system of differential equations (3.67) can be expressed as

$$\xi^2 \begin{bmatrix} \boldsymbol{E}_0^{uu} & \boldsymbol{E}_0^{uc} \\ (\boldsymbol{E}_0^{uc})^T & \boldsymbol{E}_0^{cc} \end{bmatrix} \begin{Bmatrix} \boldsymbol{U}_{,\xi\xi}^{hu} \\ \boldsymbol{U}_{,\xi\xi}^{hc} \end{Bmatrix} + \xi \begin{bmatrix} \boldsymbol{E}_0^{uu} + (\boldsymbol{E}_1^{uu})^T - \boldsymbol{E}_1^{uu} & \boldsymbol{E}_0^{uc} + (\boldsymbol{E}_1^{cu})^T - \boldsymbol{E}_1^{uc} \\ (\boldsymbol{E}_0^{uc})^T + (\boldsymbol{E}_1^{uc})^T - \boldsymbol{E}_1^{cu} & \boldsymbol{E}_0^{cc} + (\boldsymbol{E}_1^{cc})^T - \boldsymbol{E}_1^{cc} \end{bmatrix} \begin{Bmatrix} \boldsymbol{U}_{,\xi}^{hu} \\ \boldsymbol{U}_{,\xi}^{hc} \end{Bmatrix} - \begin{bmatrix} \boldsymbol{E}_2^{uu} & \boldsymbol{E}_2^{uc} \\ (\boldsymbol{E}_2^{uc})^T & \boldsymbol{E}_2^{cc} \end{bmatrix} \begin{Bmatrix} \boldsymbol{U}^{hu} \\ \boldsymbol{U}^{hc} \end{Bmatrix} + \xi \begin{Bmatrix} \boldsymbol{F}^{tu} \\ \boldsymbol{F}^{tc} \end{Bmatrix} + \xi^2 \begin{Bmatrix} \boldsymbol{F}^{bu} \\ \boldsymbol{F}^{bc} \end{Bmatrix} = \boldsymbol{0} \tag{3. 71}$$

Similarly, equation (3.70) for the nodal internal flux can also be expressed, in a partitioned form, as

$$\begin{Bmatrix} \boldsymbol{Q}^{hu} \\ \boldsymbol{Q}^{hc} \end{Bmatrix} = \xi \begin{bmatrix} \boldsymbol{E}_0^{uu} & \boldsymbol{E}_0^{uc} \\ (\boldsymbol{E}_0^{uc})^T & \boldsymbol{E}_0^{cc} \end{bmatrix} \begin{Bmatrix} \boldsymbol{U}_{,\xi}^{hu} \\ \boldsymbol{U}_{,\xi}^{hc} \end{Bmatrix} + \begin{bmatrix} (\boldsymbol{E}_1^{uu})^T & (\boldsymbol{E}_1^{cu})^T \\ (\boldsymbol{E}_1^{uc})^T & (\boldsymbol{E}_1^{cc})^T \end{bmatrix} \begin{Bmatrix} \boldsymbol{U}^{hu} \\ \boldsymbol{U}^{hc} \end{Bmatrix} \tag{3. 72}$$

Equation (3.71) can be separated into two systems:

$$\xi^2 \boldsymbol{E}_0^{uu} \boldsymbol{U}_{,\xi\xi}^{hu} + \xi\left[\boldsymbol{E}_0^{uu} + (\boldsymbol{E}_1^{uu})^T - \boldsymbol{E}_1^{uu}\right]\boldsymbol{U}_{,\xi}^{hu} - \boldsymbol{E}_2^{uu}\boldsymbol{U}^{hu} = -\xi \boldsymbol{F}^{tu} - \xi^2 \boldsymbol{F}^{bu} - \boldsymbol{F}^{suu} \tag{3. 73}$$

$$\xi \boldsymbol{F}^{tc} = -\xi^2 \boldsymbol{F}^{bc} - \boldsymbol{F}^{suc} - \boldsymbol{F}^{scc} \tag{3. 74}$$

where the vectors $\boldsymbol{F}^{suu}$, $\boldsymbol{F}^{suc}$, and $\boldsymbol{F}^{scc}$ are defined by

$$\boldsymbol{F}^{suu} = \xi^2 \boldsymbol{E}_0^{uc} \boldsymbol{U}_{,\xi\xi}^{hc} + \xi(\boldsymbol{E}_0^{uc} + (\boldsymbol{E}_1^{cu})^T - \boldsymbol{E}_1^{uc})\boldsymbol{U}_{,\xi}^{hc} - \boldsymbol{E}_2^{uc}\boldsymbol{U}^{hc} \tag{3. 75}$$

$$\boldsymbol{F}^{suc} = \xi^2 (\boldsymbol{E}_0^{uc})^T \boldsymbol{U}_{,\xi\xi}^{hu} + \xi\left[(\boldsymbol{E}_0^{uc})^T + (\boldsymbol{E}_1^{uc})^T - \boldsymbol{E}_1^{cu}\right]\boldsymbol{U}_{,\xi}^{hu} - (\boldsymbol{E}_2^{uc})^T\boldsymbol{U}^{hu} \tag{3. 76}$$

$$\boldsymbol{F}^{scc} = \xi^2 \boldsymbol{E}_0^{cc} \boldsymbol{U}_{,\xi\xi}^{hc} + \xi\left[\boldsymbol{E}_0^{cc} + (\boldsymbol{E}_1^{cc})^T - \boldsymbol{E}_1^{cc}\right]\boldsymbol{U}_{,\xi}^{hc} - \boldsymbol{E}_2^{cc}\boldsymbol{U}^{hc} \tag{3. 77}$$

It can be remarked that $\boldsymbol{F}^{suu}$ and $\boldsymbol{F}^{scc}$ are known vectors obtained from the prescribed state variable on the side face whereas $\boldsymbol{F}^{suc}$ is an unknown vector involving the unknown vector $\boldsymbol{U}^{hu}$. By following the same procedure, the partitioned equation (3.72) can also be separated into two systems:

$$\boldsymbol{Q}^{hu}(\xi) = \xi \boldsymbol{E}_0^{uu} \boldsymbol{U}_{,\xi}^{hu} + (\boldsymbol{E}_1^{uu})^T \boldsymbol{U}^{hu} + \boldsymbol{Q}^{huc}(\xi) \tag{3. 78}$$

$$\boldsymbol{Q}^{hc}(\xi) = \xi (\boldsymbol{E}_0^{uc})^T \boldsymbol{U}_{,\xi}^{hu} + (\boldsymbol{E}_1^{uc})^T \boldsymbol{U}^{hu} + \boldsymbol{Q}^{hcc}(\xi) \tag{3. 79}$$

where the known vectors $\boldsymbol{Q}^{huc}(\xi)$ and $\boldsymbol{Q}^{hcc}(\xi)$ are defined by

$$\boldsymbol{Q}^{huc}(\xi) = \xi \boldsymbol{E}_0^{uc} \boldsymbol{U}_{,\xi}^{hc} + (\boldsymbol{E}_1^{cu})^T \boldsymbol{U}^{hc} \tag{3. 80}$$

$$\boldsymbol{Q}^{huc}(\xi) = \xi \boldsymbol{E}_0^{cc} \boldsymbol{U}_{,\xi}^{hc} + (\boldsymbol{E}_1^{cc})^T \boldsymbol{U}^{hc} \tag{3. 81}$$

Now, a system of differential equations (3.73) along with the following two boundary conditions on the inner and outer boundaries:

$$\boldsymbol{Q}^{hu}(\xi_2) = \boldsymbol{P}_2^u \tag{3. 82}$$

$$\boldsymbol{Q}^{hu}(\xi_1) = -\boldsymbol{P}_1^u \tag{3. 83}$$

is sufficient for determining the general solution of $\boldsymbol{U}^{hu}$ for the given boundary value problem. The vectors $\boldsymbol{P}_2^u$ and $\boldsymbol{P}_1^u$ result directly from the partition of the vectors $\boldsymbol{P}_2$ and $\boldsymbol{P}_1$, respectively, i.e., $\boldsymbol{P}_2 = \{\boldsymbol{P}_2^u \quad \boldsymbol{P}_2^c\}^T$ and $\boldsymbol{P}_1 = \{\boldsymbol{P}_1^u \quad \boldsymbol{P}_1^c\}^T$. Once $\boldsymbol{U}^{hu}$ is solved, the unknown vectors $\boldsymbol{F}^{tc}$, $\boldsymbol{P}_1^c$, and $\boldsymbol{P}_2^c$ can be obtained, respectively, by (3.74) and

$$\boldsymbol{Q}^{hc}(\xi_2) = \boldsymbol{P}_2^c \tag{3. 84}$$

$$\boldsymbol{Q}^{hc}(\xi_1) = -\boldsymbol{P}_1^c \tag{3. 85}$$

Details of the solution procedure are provided in the next chapter.

Chapter 4
SOLUTION METHODOLOGY

This chapter presents the procedure for obtaining the analytical solution of a system of linear, second-order, nonhomogeneous, ordinary differential equations (3.73) and the boundary conditions (3.82) and (3.83). A corresponding eigenvalue problem is solved first to determine the homogeneous solution and the technique of assumed solution form is utilized to construct the particular solution associated with the distributed body source, the prescribed surface flux on the side face, and the prescribed state variable on the side face. Once the general solution is obtained, the boundary conditions on the inner and outer boundaries are enforced to determine all involved constants. Finally, the post-process for the field quantities such as the state variable and body flux is described.

4.1 Determination of Homogeneous Solution

In this section, a homogeneous solution of the system of linear differential equations (3.73), denoted by $\boldsymbol{U}_0^{hu}$, is derived following standard procedure from the theory of differential equations. The homogeneous solution $\boldsymbol{U}_0^{hu}$ must satisfy

$$\xi^2 \boldsymbol{E}_0^{uu}\boldsymbol{U}_{0,\xi\xi}^{hu} + \xi\left[\boldsymbol{E}_0^{uu} + (\boldsymbol{E}_1^{uu})^T - \boldsymbol{E}_1^{uu}\right]\boldsymbol{U}_{0,\xi}^{hu} - \boldsymbol{E}_2^{uu}\boldsymbol{U}_0^{hu} = \boldsymbol{0} \tag{4. 1}$$

The corresponding nodal internal flux, denoted by $\boldsymbol{Q}_0^{hu}(\xi)$, is given by

$$\boldsymbol{Q}_0^{hu}(\xi) = \xi \boldsymbol{E}_0^{uu}\boldsymbol{U}_{0,\xi}^{hu} + (\boldsymbol{E}_1^{uu})^T \boldsymbol{U}_0^{hu} \tag{4. 2}$$

Since (4.1) is a set of $(m-p)\Lambda$ linear, second-order, Euler-Cauchy differential equations, the solution $\boldsymbol{U}_0^{hu}$ takes the following form

$$\boldsymbol{U}_0^{hu}(\xi) = \sum_{i=1}^{2(m-p)\Lambda} c_i \xi^{\lambda_i} \boldsymbol{\psi}_i^u \tag{4. 3}$$

where a constant λ_i is termed the modal scaling factor, $\boldsymbol{\psi}_i$ is the $(m-p)\Lambda$-component vector representing the i^{th} mode of the state variable, and c_i are arbitrary constants denoting the contribution of each mode to the solution. By substituting (4.3) into (4.2), it leads to

$$\boldsymbol{Q}_0^{hu}(\xi) = \sum_{i=1}^{2(m-p)\Lambda} c_i \xi^{\lambda_i} \left[\lambda_i \boldsymbol{E}_0^{uu} + (\boldsymbol{E}_1^{uu})^T\right]\boldsymbol{\psi}_i^u = \sum_{i=1}^{2(m-p)\Lambda} c_i \xi^{\lambda_i} \boldsymbol{q}_i^u \tag{4. 4}$$

where $\boldsymbol{q}_i^u$ is termed the i^{th} modal internal flux given in terms of $\boldsymbol{\psi}_i^u$ by

$$\boldsymbol{q}_i^u = \left[\lambda_i \boldsymbol{E}_0^{uu} + (\boldsymbol{E}_1^{uu})^T \right] \boldsymbol{\psi}_i^u \quad \forall i \in \{1, 2, ..., 2(m-p)\Lambda\} \tag{4. 5}$$

By substituting (4.3) into (4.1), it results in

$$\sum_{i=1}^{2(m-p)\Lambda} c_i \xi^{\lambda_i} \left\{ \lambda_i (\lambda_i - 1) \boldsymbol{E}_0^{uu} + \lambda_i \left[\boldsymbol{E}_0^{uu} + (\boldsymbol{E}_1^{uu})^T - \boldsymbol{E}_1^{uu} \right] - \boldsymbol{E}_2^{uu} \right\} \boldsymbol{\psi}_i^u = \boldsymbol{0} \tag{4. 6}$$

Since c_i are arbitrary, (4.6) implies that

$$\left\{ \lambda_i^2 \boldsymbol{E}_0^{uu} + \lambda_i \left[(\boldsymbol{E}_1^{uu})^T - \boldsymbol{E}_1^{uu} \right] - \boldsymbol{E}_2^{uu} \right\} \boldsymbol{\psi}_i^u = \boldsymbol{0} \quad \forall i \in \{1, 2, ..., 2(m-p)\Lambda\} \tag{4. 7}$$

By further rearranging terms in (4.5) such that

$$\lambda_i \boldsymbol{\psi}_i^u = -(\boldsymbol{E}_0^{uu})^{-1} (\boldsymbol{E}_1^{uu})^T \boldsymbol{\psi}_i^u + (\boldsymbol{E}_0^{uu})^{-1} \boldsymbol{q}_i^u \tag{4. 8}$$

where $(\boldsymbol{E}_0^{uu})^{-1}$ denotes the inverse of $\boldsymbol{E}_0^{uu}$, and then substituting the result into (4.7), it gives rise to

$$\lambda_i \boldsymbol{q}_i^u = \left[\boldsymbol{E}_2^{uu} - \boldsymbol{E}_1^{uu} (\boldsymbol{E}_0^{uu})^{-1} (\boldsymbol{E}_1^{uu})^T \right] \boldsymbol{\psi}_i^u + \boldsymbol{E}_1^{uu} (\boldsymbol{E}_0^{uu})^{-1} \boldsymbol{q}_i^u \tag{4. 9}$$

Now, by introducing a $2(m-p)\Lambda$-component vector $\boldsymbol{X}_i$ such that $\boldsymbol{X}_i = \{\boldsymbol{\psi}_i^u \quad \boldsymbol{q}_i^u\}^T$, equations (4.8) and (4.9) can be combined into a system of linear algebraic equations

$$\boldsymbol{A}\boldsymbol{X}_i = \lambda_i \boldsymbol{X}_i \tag{4. 10}$$

where the matrix $\boldsymbol{A}$ is given by

$$\boldsymbol{A} = \begin{bmatrix} -(\boldsymbol{E}_0^{uu})^{-1} (\boldsymbol{E}_1^{uu})^T & (\boldsymbol{E}_0^{uu})^{-1} \\ \boldsymbol{E}_2^{uu} - \boldsymbol{E}_1^{uu} (\boldsymbol{E}_0^{uu})^{-1} (\boldsymbol{E}_1^{uu})^T & \boldsymbol{E}_1^{uu} (\boldsymbol{E}_0^{uu})^{-1} \end{bmatrix} \tag{4. 11}$$

Determination of all $2(m-p)\Lambda$ pairs $\{\lambda_i, \boldsymbol{X}_i\}$ is achieved by solving the eigenvalue problem (4.10) where λ_i denote the eigenvalues and $\boldsymbol{X}_i$ are associated eigenvectors. It should be remarked that since $\boldsymbol{A}$ is not symmetric, $\{\lambda_i, \boldsymbol{X}_i\}$ can involve complex numbers. In fact, only a half of the eigenvalues has the positive real part whereas the other half has negative real part. Let $\boldsymbol{\lambda}^+$ and $\boldsymbol{\lambda}^-$ be $(m-p)\Lambda \times (m-p)\Lambda$ diagonal matrices containing eigenvalues with the positive real part and the negative real part, respectively. Also, let $\boldsymbol{\Phi}^{\psi+}$ and $\boldsymbol{\Phi}^{q+}$ be matrices whose columns containing, respectively, all vectors $\boldsymbol{\psi}_i^u$ and $\boldsymbol{q}_i^u$ obtained from the eigenvectors $\boldsymbol{X}_i = \{\boldsymbol{\psi}_i^u \quad \boldsymbol{q}_i^u\}^T$ associated with all eigenvalues contained in $\boldsymbol{\lambda}^+$ and let $\boldsymbol{\Phi}^{\psi-}$ and $\boldsymbol{\Phi}^{q-}$ be matrices whose columns containing, respectively, all vectors $\boldsymbol{\psi}_i^u$ and $\boldsymbol{q}_i^u$ obtained from the eigenvectors $\boldsymbol{X}_i = \{\boldsymbol{\psi}_i^u \quad \boldsymbol{q}_i^u\}^T$ associated with all eigenvalues contained in $\boldsymbol{\lambda}^-$, i.e.,

$$\boldsymbol{A}\begin{bmatrix}\boldsymbol{\Phi}^{\psi+}\\ \boldsymbol{\Phi}^{q+}\end{bmatrix}=\boldsymbol{\lambda}^{+}\begin{bmatrix}\boldsymbol{\Phi}^{\psi+}\\ \boldsymbol{\Phi}^{q+}\end{bmatrix} \tag{4. 12}$$

$$\boldsymbol{A}\begin{bmatrix}\boldsymbol{\Phi}^{\psi-}\\ \boldsymbol{\Phi}^{q-}\end{bmatrix}=\boldsymbol{\lambda}^{-}\begin{bmatrix}\boldsymbol{\Phi}^{\psi-}\\ \boldsymbol{\Phi}^{q-}\end{bmatrix} \tag{4. 13}$$

Now, the homogeneous solutions $\boldsymbol{U}_0^{hu}$ and $\boldsymbol{Q}_0^{hu}(\xi)$ are given by

$$\boldsymbol{U}_0^{hu}(\xi)=\boldsymbol{\Phi}^{\psi+}\boldsymbol{\Pi}^{+}(\xi)\boldsymbol{C}^{+}+\boldsymbol{\Phi}^{\psi-}\boldsymbol{\Pi}^{-}(\xi)\boldsymbol{C}^{-} \tag{4. 14}$$

$$\boldsymbol{Q}_0^{hu}(\xi)=\boldsymbol{\Phi}^{q+}\boldsymbol{\Pi}^{+}(\xi)\boldsymbol{C}^{+}+\boldsymbol{\Phi}^{q-}\boldsymbol{\Pi}^{-}(\xi)\boldsymbol{C}^{-} \tag{4. 15}$$

where $\boldsymbol{\Pi}^{+}$ and $\boldsymbol{\Pi}^{-}$ are diagonal matrices obtained by simply replacing the diagonal entries λ_i of the matrices $\boldsymbol{\lambda}^{+}$ and $\boldsymbol{\lambda}^{-}$ by the a function ξ^{λ_i}, respectively; and $\boldsymbol{C}^{+}$ and $\boldsymbol{C}^{-}$ are vectors containing arbitrary constants representing the contribution of each mode. It is apparent that the diagonal entries of $\boldsymbol{\Pi}^{+}$ become infinite when $\xi \to \infty$ whereas those of $\boldsymbol{\Pi}^{-}$ is unbounded when $\xi \to 0$. As a result, $\boldsymbol{C}^{+}$ is taken to $\boldsymbol{0}$ to ensure the boundedness of the solution for unbounded bodies and, similarly, the condition $\boldsymbol{C}^{-}=\boldsymbol{0}$ is enforced for bodies containing the scaling center.

4.2 Determination of Particular Solution

In this section, a particular solution of the system of linear differential equations (3.73), denoted by $\boldsymbol{U}_1^{hu}$, is established. In the present study, the distributed body source $\boldsymbol{b}$, the surface flux on the side-face-1 $\boldsymbol{t}_1^{s}$ (if it is prescribed), the surface flux on the side-face-2 $\boldsymbol{t}_2^{s}$ (if it is prescribed), and the prescribed state variable on the side face $\boldsymbol{U}^{hc}$ are assumed to admit the form

$$\boldsymbol{b}(\xi,s)=\sum_{\kappa_j\in\mathbb{R}^*}\xi^{\kappa_j}\bar{\boldsymbol{b}}_j(s) \tag{4. 16}$$

$$\boldsymbol{t}_1^{s}(\xi)=\sum_{\tau_j\in\mathbb{R}^*}\xi^{\tau_j}\bar{\boldsymbol{t}}_j^{s1} \tag{4. 17}$$

$$\boldsymbol{t}_2^{s}(\xi)=\sum_{\gamma_j\in\mathbb{R}^*}\xi^{\gamma_j}\bar{\boldsymbol{t}}_j^{s2} \tag{4. 18}$$

$$\boldsymbol{U}^{hc}(\xi)=\sum_{\omega_j\in\mathbb{R}^*}\xi^{\omega_j}\bar{\boldsymbol{U}}_j^{hc} \tag{4. 19}$$

where $\mathbb{R}^*$ denotes a set of non-negative real numbers, $\bar{\boldsymbol{b}}_j(s)$ are given vectors which are a function of s, and $\bar{\boldsymbol{t}}_j^{s1}$, $\bar{\boldsymbol{t}}_j^{s2}$, $\bar{\boldsymbol{U}}_j^{hc}$ are given constant vectors. Substituting (4.16) into (3.65), (4.17) into (3.62), (4.18) into (3.63), and (4.19) into (3.75) yields

$$\boldsymbol{F}^{b} = \sum_{\kappa_j \in \mathbb{R}^*} \xi^{\kappa_j} \bar{\boldsymbol{F}}_j^{b} \tag{4. 20}$$

$$\boldsymbol{F}_1^{t} = \sum_{\tau_j \in \mathbb{R}^*} \xi^{\tau_j} \bar{\boldsymbol{F}}_j^{t1} \tag{4. 21}$$

$$\boldsymbol{F}_2^{t} = \sum_{\gamma_j \in \mathbb{R}^*} \xi^{\gamma_j} \bar{\boldsymbol{F}}_j^{t2} \tag{4. 22}$$

$$\boldsymbol{F}^{suu} = \sum_{\omega_j \in \mathbb{R}^*} \xi^{\omega_j} \bar{\boldsymbol{F}}_j^{suu} \tag{4. 23}$$

where $\bar{\boldsymbol{F}}_j^{b}$, $\bar{\boldsymbol{F}}_j^{t1}$, $\bar{\boldsymbol{F}}_j^{t2}$, and $\bar{\boldsymbol{F}}_j^{suu}$ are constant vectors defined, in terms of prescribed data, by

$$\bar{\boldsymbol{F}}_j^{b} = \left\{ \int_{s_i}^{s_o} \phi_{(1)} \bar{\boldsymbol{b}}_j(s) J ds \quad \int_{s_i}^{s_o} \phi_{(2)} \bar{\boldsymbol{b}}_j(s) J ds \quad \cdots \quad \int_{s_i}^{s_o} \phi_{(m)} \bar{\boldsymbol{b}}_j(s) J ds \right\}^T \tag{4. 24}$$

$$\bar{\boldsymbol{F}}_j^{t1} = \{ J_1^{\xi} \bar{\boldsymbol{t}}_j^{s1} \quad \boldsymbol{0} \quad \cdots \quad \boldsymbol{0} \} \tag{4. 25}$$

$$\bar{\boldsymbol{F}}_j^{t2} = \{ \boldsymbol{0} \quad \boldsymbol{0} \quad \cdots \quad J_2^{\xi} \bar{\boldsymbol{t}}_j^{s2} \}^T \tag{4. 26}$$

$$\bar{\boldsymbol{F}}_j^{suu} = \left\{ \omega_j(\omega_j - 1)\boldsymbol{E}_0^{uc} + \omega_j(\boldsymbol{E}_0^{uc} + (\boldsymbol{E}_1^{cu})^T - \boldsymbol{E}_1^{uc}) - \boldsymbol{E}_2^{uc} \right\} \bar{\boldsymbol{U}}_j^{hc} \tag{4. 27}$$

The vectors $\boldsymbol{F}^{b}$ and $\boldsymbol{F}^{t} = \boldsymbol{F}_1^{t} + \boldsymbol{F}_2^{t}$ can be further partitioned to obtain $\boldsymbol{F}^{b} = \{\boldsymbol{F}^{bu} \quad \boldsymbol{F}^{bc}\}^T$ and $\boldsymbol{F}^{t} = \{\boldsymbol{F}^{tu} \quad \boldsymbol{F}^{tc}\}^T = \{\boldsymbol{F}_1^{tu} \quad \boldsymbol{F}_1^{tc}\}^T + \{\boldsymbol{F}_2^{tu} \quad \boldsymbol{F}_2^{tc}\}^T$ where

$$\boldsymbol{F}^{bu} = \sum_{\kappa_j \in \mathbb{R}^*} \xi^{\kappa_j} \bar{\boldsymbol{F}}_j^{bu}; \ \ \boldsymbol{F}^{bc} = \sum_{\kappa_j \in \mathbb{R}^*} \xi^{\kappa_j} \bar{\boldsymbol{F}}_j^{bc}; \ \ \bar{\boldsymbol{F}}_j^{b} = \left\{ \bar{\boldsymbol{F}}_j^{bu} \quad \bar{\boldsymbol{F}}_j^{bc} \right\}^T \tag{4. 28}$$

$$\boldsymbol{F}_1^{tu} = \sum_{\tau_j \in \mathbb{R}^*} \xi^{\tau_j} \bar{\boldsymbol{F}}_j^{tu1}; \ \ \boldsymbol{F}_1^{tc} = \sum_{\tau_j \in \mathbb{R}^*} \xi^{\tau_j} \bar{\boldsymbol{F}}_j^{tc1}; \ \ \bar{\boldsymbol{F}}_j^{t1} = \left\{ \bar{\boldsymbol{F}}_j^{tu1} \quad \bar{\boldsymbol{F}}_j^{tc1} \right\}^T \tag{4. 29}$$

$$\boldsymbol{F}_2^{tu} = \sum_{\gamma_j \in \mathbb{R}^*} \xi^{\gamma_j} \bar{\boldsymbol{F}}_j^{tu2}; \ \ \boldsymbol{F}_2^{tc} = \sum_{\gamma_j \in \mathbb{R}^*} \xi^{\gamma_j} \bar{\boldsymbol{F}}_j^{tc2}; \ \ \bar{\boldsymbol{F}}_j^{t2} = \left\{ \bar{\boldsymbol{F}}_j^{tu2} \quad \bar{\boldsymbol{F}}_j^{tc2} \right\}^T \tag{4. 30}$$

Based on this form of prescribed data, the particular solution $\boldsymbol{U}_1^{hu}$ must take the form

$$\boldsymbol{U}_1^{hu}(\xi) = \boldsymbol{U}_1^{hub}(\xi) + \boldsymbol{U}_1^{hut1}(\xi) + \boldsymbol{U}_1^{hut2}(\xi) + \boldsymbol{U}_1^{huu}(\xi) \tag{4. 31}$$

where

$$\boldsymbol{U}_1^{hub}(\xi) = \sum_{\kappa_j \in \mathbb{R}^*} \xi^{\kappa_j + 2} \boldsymbol{c}_j^{b} \tag{4. 32}$$

$$\boldsymbol{U}_1^{hut1}(\xi) = \sum_{\tau_j \in \mathbb{R}^*} \xi^{\tau_j+1} \boldsymbol{c}_j^{t1} \tag{4. 33}$$

$$\boldsymbol{U}_1^{hut2}(\xi) = \sum_{\gamma_j \in \mathbb{R}^*} \xi^{\gamma_j+1} \boldsymbol{c}_j^{t2} \tag{4. 34}$$

$$\boldsymbol{U}_1^{huu}(\xi) = \sum_{\omega_j \in \mathbb{R}^*} \xi^{\omega_j} \boldsymbol{c}_j^{uc} \tag{4. 35}$$

with $\boldsymbol{c}_j^b$, $\boldsymbol{c}_j^{t1}$, $\boldsymbol{c}_j^{t2}$, and $\boldsymbol{c}_j^{uc}$ being vectors of unknown constants. By substituting (4.20)-(4.23) and (4.31) along with (4.32)-(4.35) into (3.73), it leads to

$$\begin{aligned}
&\sum_{\kappa_j \in \mathbb{R}^*} \xi^{\kappa_j+2} \left[\left\{ (\kappa_j+2)(\kappa_j+1)\boldsymbol{E}_0^{uu} + (\kappa_j+2)\left[\boldsymbol{E}_0^{uu} + (\boldsymbol{E}_1^{uu})^T - \boldsymbol{E}_1^{uu} \right] - \boldsymbol{E}_2^{uu} \right\} \boldsymbol{c}_j^b + \bar{\boldsymbol{F}}_j^{bu} \right] + \\
&\sum_{\tau_j \in \mathbb{R}^*} \xi^{\tau_j+1} \left[\left\{ (\tau_j+1)\tau_j \boldsymbol{E}_0^{uu} + (\tau_j+1)\left[\boldsymbol{E}_0^{uu} + (\boldsymbol{E}_1^{uu})^T - \boldsymbol{E}_1^{uu} \right] - \boldsymbol{E}_2^{uu} \right\} \boldsymbol{c}_j^{t1} + \bar{\boldsymbol{F}}_j^{tu1} \right] + \\
&\sum_{\gamma_j \in \mathbb{R}^*} \xi^{\gamma_j+1} \left[\left\{ (\gamma_j+1)\gamma_j \boldsymbol{E}_0^{uu} + (\gamma_j+1)\left[\boldsymbol{E}_0^{uu} + (\boldsymbol{E}_1^{uu})^T - \boldsymbol{E}_1^{uu} \right] - \boldsymbol{E}_2^{uu} \right\} \boldsymbol{c}_j^{t2} + \bar{\boldsymbol{F}}_j^{tu2} \right] + \\
&\sum_{\omega_j \in \mathbb{R}^*} \xi^{\omega_j} \left[\left\{ \omega_j(\omega_j-1) \boldsymbol{E}_0^{uu} + (\omega_j-1)\left[\boldsymbol{E}_0^{uu} + (\boldsymbol{E}_1^{uu})^T - \boldsymbol{E}_1^{uu} \right] - \boldsymbol{E}_2^{uu} \right\} \boldsymbol{c}_j^{uc} + \bar{\boldsymbol{F}}_j^{suu} \right] = 0
\end{aligned} \tag{4. 36}$$

Equation (4.36) can be satisfied $\forall \xi \in [\xi_1, \xi_2]$ if and only if

$$\left\{ (\kappa_j+2)(\kappa_j+1)\boldsymbol{E}_0^{uu} + (\kappa_j+2)\left[\boldsymbol{E}_0^{uu} + (\boldsymbol{E}_1^{uu})^T - \boldsymbol{E}_1^{uu} \right] - \boldsymbol{E}_2^{uu} \right\} \boldsymbol{c}_j^b + \bar{\boldsymbol{F}}_j^{bu} = \boldsymbol{0} \tag{4. 37}$$

$$\left\{ (\tau_j+1)\tau_j \boldsymbol{E}_0^{uu} + (\tau_j+1)\left[\boldsymbol{E}_0^{uu} + (\boldsymbol{E}_1^{uu})^T - \boldsymbol{E}_1^{uu} \right] - \boldsymbol{E}_2^{uu} \right\} \boldsymbol{c}_j^{t1} + \bar{\boldsymbol{F}}_j^{tu1} = \boldsymbol{0} \tag{4. 38}$$

$$\left\{ (\gamma_j+1)\gamma_j \boldsymbol{E}_0^{uu} + (\gamma_j+1)\left[\boldsymbol{E}_0^{uu} + (\boldsymbol{E}_1^{uu})^T - \boldsymbol{E}_1^{uu} \right] - \boldsymbol{E}_2^{uu} \right\} \boldsymbol{c}_j^{t2} + \bar{\boldsymbol{F}}_j^{tu2} = \boldsymbol{0} \tag{4. 39}$$

$$\left\{ \omega_j(\omega_j-1) \boldsymbol{E}_0^{uu} + (\omega_j-1)\left[\boldsymbol{E}_0^{uu} + (\boldsymbol{E}_1^{uu})^T - \boldsymbol{E}_1^{uu} \right] - \boldsymbol{E}_2^{uu} \right\} \boldsymbol{c}_j^{uc} + \bar{\boldsymbol{F}}_j^{suu} = \boldsymbol{0} \tag{4. 40}$$

A system of linear algebraic equations (4.37)-(4.40) is sufficient for determining all unknown constant vectors $\boldsymbol{c}_j^b$, $\boldsymbol{c}_j^{t1}$, $\boldsymbol{c}_j^{t2}$, and $\boldsymbol{c}_j^{uc}$. One the particular solution $\boldsymbol{U}_1^{hu}(\xi)$ is obtained, the corresponding particular nodal internal flux, denoted by $\boldsymbol{Q}_1^{hu}(\xi)$, is given by

$$\boldsymbol{Q}_1^{hu}(\xi) = \xi \boldsymbol{E}_0^{uu} \boldsymbol{U}_{1,\xi}^{hu} + (\boldsymbol{E}_1^{uu})^T \boldsymbol{U}_1^{hu} \tag{4. 41}$$

4.3 Final General Solution

The general solution of (3.73) $\boldsymbol{U}^{hu}(\xi)$ and the corresponding nodal internal flux $\boldsymbol{Q}^{hu}(\xi)$ are then given by

$$\boldsymbol{U}^{hu}(\xi) = \boldsymbol{U}_0^{hu}(\xi) + \boldsymbol{U}_1^{hu}(\xi) = \boldsymbol{\Phi}^{\psi+} \boldsymbol{\Pi}^{+}(\xi) \boldsymbol{C}^{+} + \boldsymbol{\Phi}^{\psi-} \boldsymbol{\Pi}^{-}(\xi) \boldsymbol{C}^{-} + \boldsymbol{U}_1^{hu}(\xi) \tag{4. 42}$$

$$\boldsymbol{Q}^{hu}(\xi)=\boldsymbol{Q}_0^{hu}(\xi)+\boldsymbol{Q}_1^{hu}(\xi)=\boldsymbol{\Phi}^{q+}\boldsymbol{\Pi}^{+}(\xi)\boldsymbol{C}^{+}+\boldsymbol{\Phi}^{q-}\boldsymbol{\Pi}^{-}(\xi)\boldsymbol{C}^{-}+\boldsymbol{Q}_1^{hu}(\xi) \tag{4. 43}$$

To determine the constants contained in $\boldsymbol{C}^{+}$ and $\boldsymbol{C}^{-}$, the boundary conditions on both inner and outer boundaries are enforced. By applying the condition (3.82) and (3.83), it results in

$$\boldsymbol{\Phi}^{q+}\boldsymbol{\Pi}^{+}(\xi_1)\boldsymbol{C}^{+}+\boldsymbol{\Phi}^{q-}\boldsymbol{\Pi}^{-}(\xi_1)\boldsymbol{C}^{-}+\boldsymbol{Q}_1^{hu}(\xi_1)=-\boldsymbol{P}_1^{u} \tag{4. 44}$$

$$\boldsymbol{\Phi}^{q+}\boldsymbol{\Pi}^{+}(\xi_2)\boldsymbol{C}^{+}+\boldsymbol{\Phi}^{q-}\boldsymbol{\Pi}^{-}(\xi_2)\boldsymbol{C}^{-}+\boldsymbol{Q}_1^{hu}(\xi_2)=\boldsymbol{P}_2^{u} \tag{4. 45}$$

It is worth noting that for bounded bodies containing the scaling center, the first system (4.44) is ignored with $\boldsymbol{C}^{-}=\boldsymbol{0}$ whereas, for unbounded bodies, the second system is ignored with $\boldsymbol{C}^{+}=\boldsymbol{0}$. The two systems (4.44) and (4.45) can be combined to obtain

$$\begin{bmatrix}\boldsymbol{\Phi}^{q+}\boldsymbol{\Pi}^{+}(\xi_1) & \boldsymbol{\Phi}^{q-}\boldsymbol{\Pi}^{-}(\xi_1)\\ \boldsymbol{\Phi}^{q+}\boldsymbol{\Pi}^{+}(\xi_2) & \boldsymbol{\Phi}^{q-}\boldsymbol{\Pi}^{-}(\xi_2)\end{bmatrix}\begin{Bmatrix}\boldsymbol{C}^{+}\\ \boldsymbol{C}^{-}\end{Bmatrix}=\begin{Bmatrix}-\boldsymbol{P}_1^{u}\\ \boldsymbol{P}_2^{u}\end{Bmatrix}-\begin{Bmatrix}\boldsymbol{Q}_1^{hu}(\xi_1)\\ \boldsymbol{Q}_1^{hu}(\xi_2)\end{Bmatrix} \tag{4. 46}$$

The system (4.46) can be inverted to obtain

$$\begin{Bmatrix}\boldsymbol{C}^{+}\\ \boldsymbol{C}^{-}\end{Bmatrix}=\begin{bmatrix}\boldsymbol{\Phi}^{q+}\boldsymbol{\Pi}^{+}(\xi_1) & \boldsymbol{\Phi}^{q-}\boldsymbol{\Pi}^{-}(\xi_1)\\ \boldsymbol{\Phi}^{q+}\boldsymbol{\Pi}^{+}(\xi_2) & \boldsymbol{\Phi}^{q-}\boldsymbol{\Pi}^{-}(\xi_2)\end{bmatrix}^{-1}\left(\begin{Bmatrix}-\boldsymbol{P}_1^{u}\\ \boldsymbol{P}_2^{u}\end{Bmatrix}-\begin{Bmatrix}\boldsymbol{Q}_1^{hu}(\xi_1)\\ \boldsymbol{Q}_1^{hu}(\xi_2)\end{Bmatrix}\right) \tag{4. 47}$$

From (4.42), it can be readily obtained

$$\begin{Bmatrix}\boldsymbol{U}^{hu}(\xi_1)\\ \boldsymbol{U}^{hu}(\xi_2)\end{Bmatrix}=\begin{bmatrix}\boldsymbol{\Phi}^{\psi+}\boldsymbol{\Pi}^{+}(\xi_1) & \boldsymbol{\Phi}^{\psi-}\boldsymbol{\Pi}^{-}(\xi_1)\\ \boldsymbol{\Phi}^{\psi+}\boldsymbol{\Pi}^{+}(\xi_2) & \boldsymbol{\Phi}^{\psi-}\boldsymbol{\Pi}^{-}(\xi_2)\end{bmatrix}\begin{Bmatrix}\boldsymbol{C}^{+}\\ \boldsymbol{C}^{-}\end{Bmatrix}+\begin{Bmatrix}\boldsymbol{Q}_1^{hu}(\xi_1)\\ \boldsymbol{Q}_1^{hu}(\xi_2)\end{Bmatrix} \tag{4. 48}$$

Substituting (4.47) into (4.48) yields

$$\boldsymbol{K}\begin{Bmatrix}\boldsymbol{U}^{hu}(\xi_1)\\ \boldsymbol{U}^{hu}(\xi_2)\end{Bmatrix}=\begin{Bmatrix}-\boldsymbol{P}_1^{u}\\ \boldsymbol{P}_2^{u}\end{Bmatrix}+\boldsymbol{K}\begin{Bmatrix}\boldsymbol{U}_1^{hu}(\xi_1)\\ \boldsymbol{U}_1^{hu}(\xi_2)\end{Bmatrix}-\begin{Bmatrix}\boldsymbol{Q}_1^{hu}(\xi_1)\\ \boldsymbol{Q}_1^{hu}(\xi_2)\end{Bmatrix} \tag{4. 49}$$

where the coefficient matrix $\boldsymbol{K}$, commonly termed the stiffness matrix, is given by

$$\boldsymbol{K}=\begin{bmatrix}\boldsymbol{\Phi}^{q+}\boldsymbol{\Pi}^{+}(\xi_1) & \boldsymbol{\Phi}^{q-}\boldsymbol{\Pi}^{-}(\xi_1)\\ \boldsymbol{\Phi}^{q+}\boldsymbol{\Pi}^{+}(\xi_2) & \boldsymbol{\Phi}^{q-}\boldsymbol{\Pi}^{-}(\xi_2)\end{bmatrix}\begin{bmatrix}\boldsymbol{\Phi}^{\psi+}\boldsymbol{\Pi}^{+}(\xi_1) & \boldsymbol{\Phi}^{\psi-}\boldsymbol{\Pi}^{-}(\xi_1)\\ \boldsymbol{\Phi}^{\psi+}\boldsymbol{\Pi}^{+}(\xi_2) & \boldsymbol{\Phi}^{\psi-}\boldsymbol{\Pi}^{-}(\xi_2)\end{bmatrix}^{-1} \tag{4. 50}$$

By applying the prescribed surface flux and the state variable on both inner and outer boundaries, a system of linear algebraic equations (4.49) is sufficient for determining all unknowns contained in the vectors $\{\boldsymbol{U}^{hu}(\xi_1)\quad \boldsymbol{U}^{hu}(\xi_2)\}^T$ and $\{-\boldsymbol{P}_1^{u}\quad \boldsymbol{P}_2^{u}\}^T$. Once the unknowns on both inner and outer boundaries are solved, the constant vectors $\boldsymbol{C}^{+}$ and $\boldsymbol{C}^{-}$ can be obtained from (4.47) and, then, the general solution for both $\boldsymbol{U}^{hu}(\xi)$ and $\boldsymbol{Q}^{hu}(\xi)$ are obtained from (4.42) and (4.43), respectively.

4.4 Post-process for Field Quantities

Once the approximate general solution $\boldsymbol{U}^{hu}(\xi)$ is obtained, the approximate field quantities such as the state variable and the surface flux within the body can be determined. For instance, the approximate state variable associated with a point (ξ, s) can be obtained from (3.39) as

$$\boldsymbol{u}^h(\xi,s) = \boldsymbol{N}^S(s)\boldsymbol{U}^h(\xi) = \begin{bmatrix} \boldsymbol{N}^{Su}(s) & \boldsymbol{N}^{Sc}(s) \end{bmatrix} \begin{Bmatrix} \boldsymbol{U}^{hu}(\xi) \\ \boldsymbol{U}^{hc}(\xi) \end{Bmatrix} = \boldsymbol{N}^{Su}(s)\boldsymbol{U}^{hu}(\xi) + \boldsymbol{N}^{Sc}(s)\boldsymbol{U}^{hc}(\xi) \quad (4.\ 51)$$

where $\boldsymbol{N}^{Su}$ and $\boldsymbol{N}^{Sc}$ are matrices resulting from the partition of $\boldsymbol{N}^S$. Similarly, the approximated body flux can be computed from (3.40) as

$$\begin{aligned} \boldsymbol{\sigma}^h(\xi,s) &= \boldsymbol{D}\left[\boldsymbol{B}_1(s)\boldsymbol{U}^h_{,\xi} + \frac{1}{\xi}\boldsymbol{B}_2(s)\boldsymbol{U}^h \right] \\ &= \boldsymbol{D}\begin{bmatrix} \boldsymbol{B}_1^u(s) & \boldsymbol{B}_1^c(s) \end{bmatrix} \begin{Bmatrix} \boldsymbol{U}^{hu}_{,\xi}(\xi) \\ \boldsymbol{U}^{hc}_{,\xi}(\xi) \end{Bmatrix} + \frac{1}{\xi}\boldsymbol{D}\begin{bmatrix} \boldsymbol{B}_2^u(s) & \boldsymbol{B}_2^c(s) \end{bmatrix} \begin{Bmatrix} \boldsymbol{U}^{hu}(\xi) \\ \boldsymbol{U}^{hc}(\xi) \end{Bmatrix} \\ &= \boldsymbol{D}\left[\boldsymbol{B}_1^u(s)\boldsymbol{U}^{hu}_{,\xi}(\xi) + \frac{1}{\xi}\boldsymbol{B}_2^u(s)\boldsymbol{U}^{hu}(\xi) \right] + \boldsymbol{D}\left[\boldsymbol{B}_1^c(s)\boldsymbol{U}^{hc}_{,\xi}(\xi) + \frac{1}{\xi}\boldsymbol{B}_2^c(s)\boldsymbol{U}^{hc}(\xi) \right] \end{aligned} \quad (4.52)$$

where $\boldsymbol{B}_1^u$, $\boldsymbol{B}_1^c$ and $\boldsymbol{B}_2^u$, $\boldsymbol{B}_2^c$ are matrices resulting from the partition of the matrices $\boldsymbol{B}_1$ and $\boldsymbol{B}_2$, respectively. It is emphasized here again that the solutions (4.48) and (4.49) also apply to the special cases of bounded and unbounded bodies. For bounded bodies containing the scaling center, $\boldsymbol{C}^-$ simply vanishes and, for unbounded bodies, $\boldsymbol{C}^+ = \boldsymbol{0}$.

4.5 Error of Approximations

To investigate the error of the scaled boundary finite element approximation, an error vector-valued function $\boldsymbol{e} = \boldsymbol{e}(x)$ is first defined by

$$\boldsymbol{e}(x) = \boldsymbol{u}^{exact}(\boldsymbol{x}) - \boldsymbol{u}^h(\boldsymbol{x}) \quad (4.53)$$

where $\boldsymbol{u}^{exact}$ and $\boldsymbol{u}^h$ denotes the exact solution and scaled boundary finite element solution of the state variables, respectively. The following standard L^2-norm is employed to measure the magnitude of the error function, i.e.,

$$\|\boldsymbol{e}\|_{L^2} = \left(\int_\Omega \boldsymbol{e}^T(x)\boldsymbol{e}(x) \right)^{1/2} \quad (4.54)$$

Note that the evaluation of the above integral can be achieved efficiently in the $\xi - s$ space. Finally, the relative prevent error, denoted by $error$, is obtained by normalizing the L^2-norm of the error function by the L^2-norm of the exact state variable, i.e.,

$$error = \frac{\| \boldsymbol{e} \|_{L^2}}{\| \boldsymbol{u}^{exact} \|_{L^2}} \times 100 \tag{4.55}$$

where

$$\| \boldsymbol{u}^{exact} \|_{L^2} = \left(\int_{\Omega} [\boldsymbol{u}^{exact}(x)]^T \boldsymbol{u}^{exact}(x) \right)^{1/2} \tag{4.56}$$

It is remarked that for problems without the exact solution, the converged solution obtained from a particular, sufficiently fine mesh can be used to estimate the error for any level of meshes used in the approximation.

Chapter 5
NUMERICAL RESULTS

This chapter presents several numerical examples to verify the proposed technique and demonstrate its performance and capabilities. To demonstrate its capability to treat a variety of boundary value problems, general boundary conditions, and prescribed data on the side faces, three different types of problems associated with steady-state heat conduction ($\Lambda = 1$), linear elasticity ($\Lambda = 2$), and linear piezoelectricity ($\Lambda = 3$), under various scenarios are considered. In the approximation, standard finite element shape functions are employed to discretize both the defining curve and the trial and test functions. The accuracy and convergence of numerical solutions are confirmed by benchmarking with available analytical solutions and carrying out the analysis via a series of meshes.

5.1 Heat Conduction in Rectangular Domain

The proposed technique is first tested with a representative problem associated with the steady-state heat conduction ($\Lambda = 1$). Let us consider a two-dimensional rectangular domain of dimensions l_1 and l_2 as shown schematically in Figure 5.1 (a). The domain is made of a medium with an isotropic heat conductivity k_0 (or, equivalently, $D_{11} = D_{22} = k_0, D_{12} = D_{21} = 0$) and subjected to a uniform heat source $b_1 = Q_0$. A zero temperature is prescribed along the boundary *AD* (i.e., $u_1^{AD} = 0$) and a uniform surface heat flux q_0 is prescribed along the boundary *BC* (i.e., $t_1^{BC} = q_0$) whereas, along the boundaries *AB* and *CD*, the surface heat flux vanishes (i.e., $t_1^{AB} = t_1^{CD} = 0$). For this particular case, the exact solution for the temperature field (i.e., $u_1(x)$) and body heat flux (i.e., $\sigma_{11}(x)$ and $\sigma_{21}(x)$) is given by

$$u_1 = \frac{1}{k_0}\left[(q_0 + Q_0 l_1)x_1 - \frac{1}{2}Q_0 x_1^2\right] \tag{5.1}$$

$$\sigma_{11} = q_0 + Q_0(l_1 - x_1), \quad \sigma_{21} = 0 \tag{5.2}$$

The domain geometry is described by the scaling center at point *D* and the defining curve *ABC*; as a result, the boundaries *AD* and *CD* become the side faces (see Figure 5.1 (b)). In the numerical study, q_0 and Q_0 are chosen such that $Q_0 l_1 = 3q_0$ and the defining curve is discretized by a series of *N* identical linear elements.

The normalized temperature $u_1 k_0 / q_0 l_1$ and the non-zero normalized body heat flux σ_{11}/q_0 along the boundary *AB* are reported in Tables 5.1 and 5.2 for various values of normalized coordinate $\bar{x}_1 = x_1/l_1$ and meshes. Clearly, computed numerical solutions exhibit an excellent convergence behavior as the number of elements increases and, in addition, accurate results in comparison with the benchmark solution can be obtained even when few elements are employed to discretize the defining curve and solution along the boundary direction. The relative percent error of the approximate temperature field versus the number of degrees of freedom used in the discretization is shown in Figure 5.2. It can be concluded from these results that the rate of convergence with respect to the L^2-norm is two when the linear finite elements are employed in the discretization.

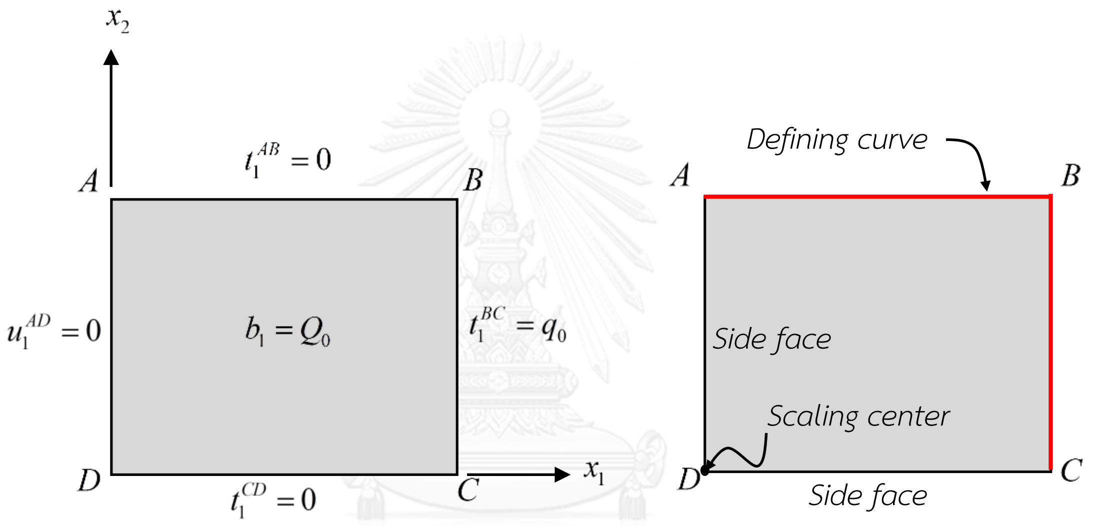

(a) (b)

Figure 5.1: Schematic of (a) rectangular domain under body heat source and mixed boundary conditions and (b) scaling center and defining curve used in scale boundary finite element analysis.

Table 5.1: Normalized temperatures along the boundary AB of a rectangular domain subjected to body heat source and mixed boundary conditions.

	$u_1 k_0 / q_0 l_1$					
$\bar{x}_1$	0.0	0.2	0.4	0.6	0.8	1.0
SBFEM, *N* = 4	0.0000	0.7196	1.3287	1.8290	2.2175	2.4684
SBFEM, *N* = 8	0.0000	0.7352	1.3520	1.8512	2.2332	2.4950
SBFEM, *N* = 16	0.0000	0.7388	1.3580	1.8577	2.2382	2.4986
SBFEM, *N* = 32	0.0000	0.7397	1.3595	1.8594	2.2395	2.4996
Exact solution	0.0000	0.7400	1.3600	1.8600	2.2400	2.5000

Table 5.2: Normalized body heat flux along the boundary AB of a rectangular domain subjected to body heat source and mixed boundary conditions.

	σ_{11}/q_0					
$\bar{x}_1$	0.0	0.2	0.4	0.6	0.8	1.0
SBFEM, *N* = 4	3.8735	3.3211	2.7724	2.2297	1.6359	0.8099
SBFEM, *N* = 8	3.9709	3.3802	2.7890	2.2037	1.6121	1.0222
SBFEM, *N* = 16	3.9929	3.3950	2.7970	2.2005	1.6034	1.0006
SBFEM, *N* = 32	3.9982	3.3988	2.7992	2.2001	1.6008	1.0000
Exact solution	4.0000	3.4000	2.8000	2.2000	1.6000	1.0000

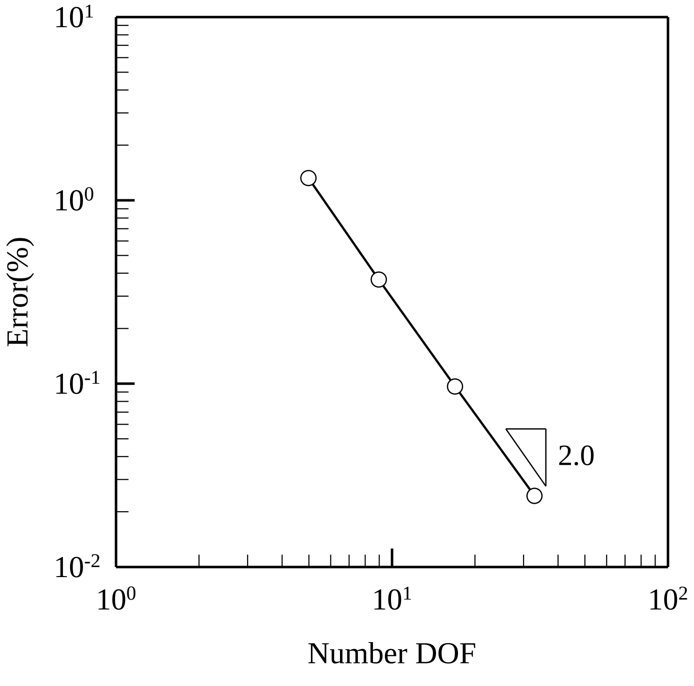

Figure 5.2: Relative percent error of temperature field versus number of degrees of freedom (DOF) for approximation by linear elements.

5.2 Linear Elastic Hollowed Cylinder under Uniform Pressure

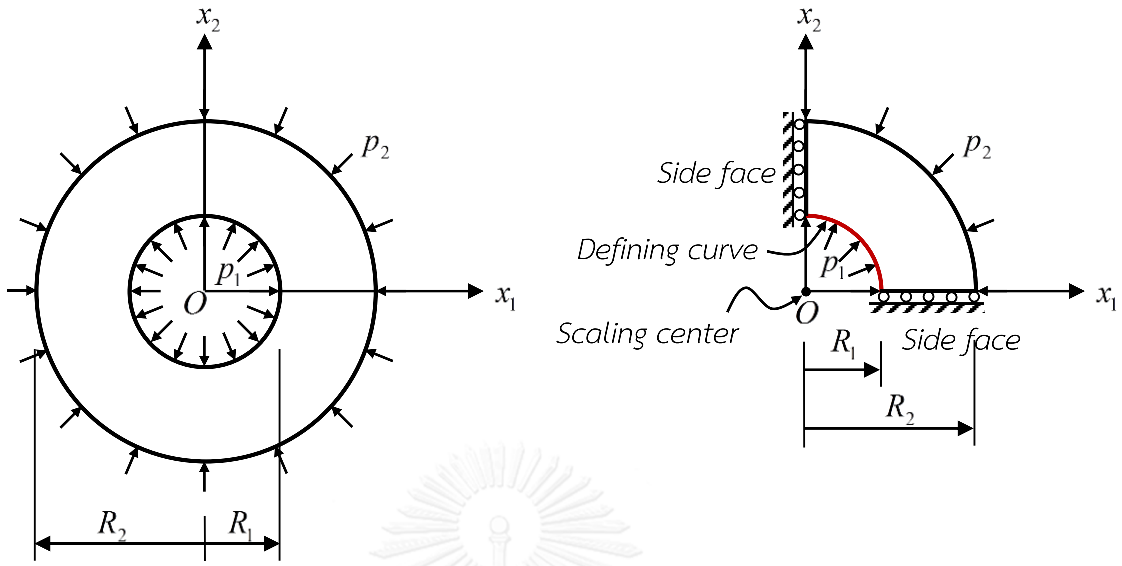

(a) (b)

Figure 5.3: Schematic of (a) hollowed cylinder under uniform internal and external pressure and (b) quarter of cylinder used in the analysis.

Consider, next, a hollowed cylinder of the inner radius R_1 and outer radius R_2 (see Figure 5.3(a)). The cylinder is made of a homogeneous, linearly elastic, isotropic material with Young's modulus E and Poisson's ratio ν and is subjected to a plane-strain condition and uniform pressure p_1 and p_2 on the inner and outer boundary, respectively, (i.e., $\Lambda = 2$ and the modulus matrix $\mathbf{D}$ with non-zero entries $D_{11} = (1-\nu)E/(1+\nu)(1-2\nu)$, $D_{44} = (1-\nu)E/(1+\nu)(1-2\nu)$, $D_{14} = D_{41} = \nu E/(1+\nu)(1-2\nu)$, $D_{23} = E/2(1+\nu)$, $D_{22} = E/2(1+\nu)$, $D_{32} = E/2(1+\nu)$, $D_{33} = E/2(1+\nu)$). Due to the symmetry, it is sufficient to model this problem using only a quarter of the cylinder (see Figure 5.3(b)) with appropriate conditions on both side faces (i.e., the normal displacement and tangential traction on the side faces vanish). To describe the geometry, the scaling center is chosen at the center of the cylinder whereas the inner boundary is treated as the defining curve. In a numerical study, $R_2 / R_1 = 1.5$, $p_2 / p_1 = 2$, $\nu = 0.3$, and meshes with N identical linear elements are employed.

Results for the normalized radial displacement ($u_r/(p_1 R_1/E)$), normalized radial stress (σ_{rr}/p_1) and normalized hoop stress ($\sigma_{\theta\theta}/p_1$) are reported along with existing analytical solutions (Martin 2014) in Tables 5.3, 5.4 and 5.5, respectively, for four meshes (i.e., $N = 4, 8, 16, 32$). It is seen that numerical solutions generated by the proposed technique converge and exhibit excellent agreement with the benchmark solution. It is worth noting that the discretization with only few linear elements can capture numerical solution with sufficient accuracy. The relative percent error of the approximate displacement field versus the number of degrees of freedom used in the discretization is shown in Figure 5.4. Again, by using linear elements in the approximation in the boundary direction, the rate of convergence with respect to the L^2-norm is the same as that of the previous example.

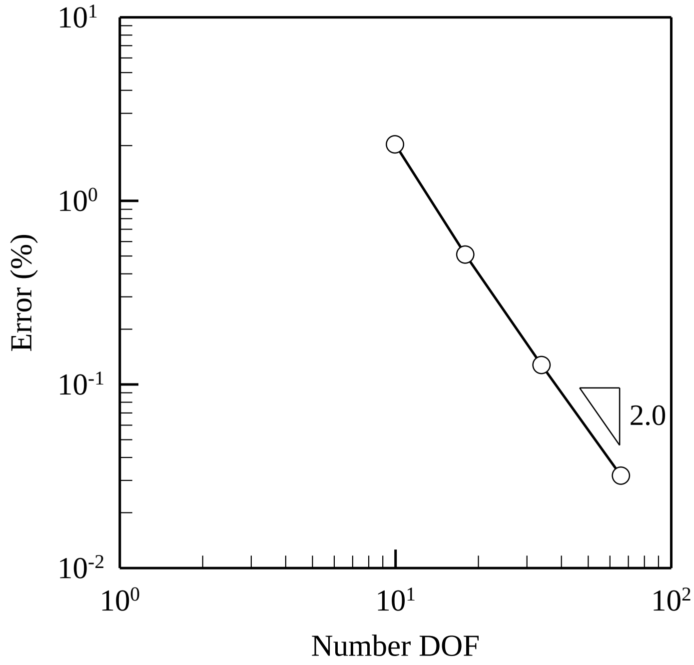

Figure 5.4: Relative percent error of displacement field versus number of degrees of freedom (DOF) for approximation by linear elements.

Table 5.3: Normalized radial displacement of hollowed cylinder under internal and external uniform pressure. Results are reported at different values of radial coordinate $r=\sqrt{x_1^2+x_2^2}$ for four meshes.

	$u_r/(p_1R_1/E)$					
r/R_1	1.0	1.1	1.2	1.3	1.4	1.5
SBFEM, N = 4	1.0958	0.9864	0.8943	0.8155	0.7473	0.6875
SBFEM, N = 8	1.1124	1.0014	0.9080	0.8282	0.7590	0.6984
SBFEM, N = 16	1.1166	1.0052	0.9115	0.8313	0.7619	0.7011
SBFEM, N = 32	1.1177	1.0061	0.9123	0.8321	0.7627	0.7018
Exact solution	1.1180	1.0064	0.9126	0.8324	0.7629	0.7020

Table 5.4: Normalized radial stress of hollowed cylinder under internal and external uniform pressure. Results are reported at different values of radial coordinate $r=\sqrt{x_1^2+x_2^2}$ for four meshes.

	σ_{rr}/p_1					
r/R_1	1.0	1.1	1.2	1.3	1.4	1.5
SBFEM, *N* = 4	-0.9821	-0.8289	-0.7124	-0.6217	-0.5497	-0.4917
SBFEM, *N* = 8	-0.9955	-0.8401	-0.7218	-0.6298	-0.5568	-0.4979
SBFEM, *N* = 16	-0.9989	-0.8429	-0.7242	-0.6319	-0.5586	-0.4995
SBFEM, *N* = 32	-0.9997	-0.8436	-0.7248	-0.6324	-0.5590	-0.4999
Exact solution	-1.0000	-0.8438	-0.7250	-0.6325	-0.5592	-0.5000

Table 5.5: Normalized hoop stress of hollowed cylinder under internal and external uniform pressure. Results are reported at different values of radial coordinate $r=\sqrt{x_1^2+x_2^2}$ for four meshes.

	$\sigma_{\theta\theta}/p_1$					
r/R_1	1.0	1.1	1.2	1.3	1.4	1.5
SBFEM, *N* = 4	0.7833	0.6301	0.5136	0.4229	0.3510	0.2929
SBFEM, *N* = 8	0.7958	0.6404	0.5222	0.4301	0.3571	0.2982
SBFEM, *N* = 16	0.7990	0.6429	0.5243	0.4319	0.3587	0.2996
SBFEM, *N* = 32	0.7997	0.6436	0.5248	0.4324	0.3591	0.2999
Exact solution	0.8000	0.6438	0.5250	0.4325	0.3592	0.3000

5.3 Pressurized Circular Hole in an Infinite Domain

Another problem in linear elasticity ($\Lambda = 2$) is considered, here, to demonstrate the capability of the implemented procedure to treat an unbounded body with prescribed state variable on the side faces. Consider a pressurized circular hole of radius R_1 in an infinite domain as shown in Figure 5.5(a). The medium is made of a homogeneous, linearly elastic, isotropic material with Young's modulus E and Poisson's ratio ν and subjected to the uniform pressure p_1 on the surface of the hole, (the modulus matrix **D** is taken to be same as that employed in section 5.2 for the plane strain condition). Due to the symmetry, it is sufficient to model this problem using only a quarter of the cylinder (see Figure 5.5(b)) with appropriate conditions on both side faces (i.e., the normal displacement and tangential traction on the side faces vanish). To describe the geometry, the scaling center is chosen at the center of the cylinder whereas the inner boundary is treated as the defining curve. In a numerical study, the Poisson's ratio $\nu = 0.3$ and meshes with N identical linear elements are employed.

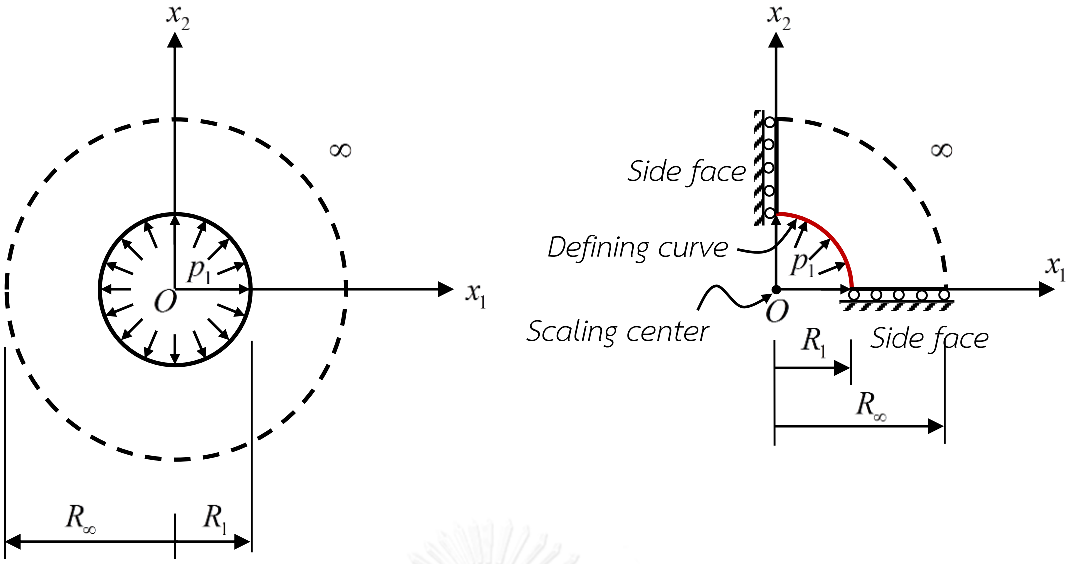

(a) (b)

Figure 5.5: Schematics of (a) pressurized circular hole in linear elastic, infinite medium and (b) quarter of domain used in the analysis.

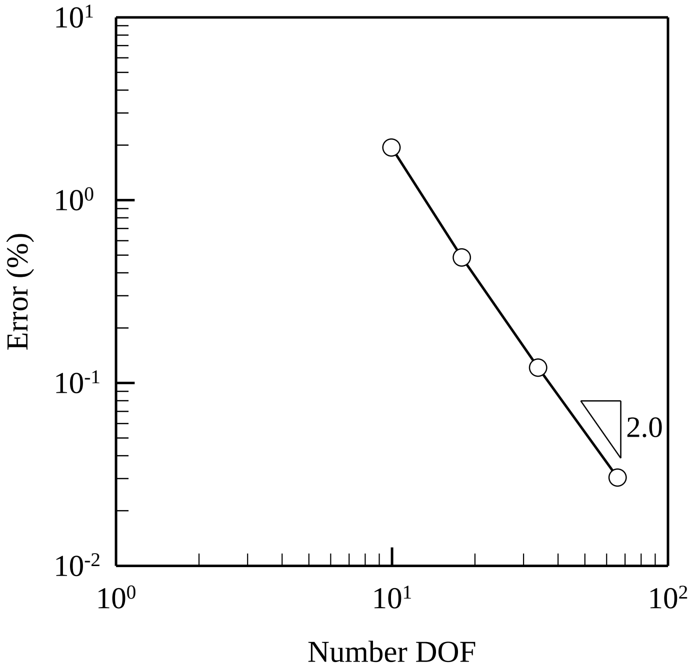

Figure 5.6: Relative percent error of displacement field versus number of degrees of freedom (DOF) for approximation by linear elements.

Results for the normalized radial displacement ($u_r/(p_1R_1/E)$), normalized radial stress (σ_{rr}/p_1) and normalized hoop stress ($\sigma_{\theta\theta}/p_1$) are reported along with existing analytical solutions (Martin 2014) in Tables 5.6 and Figure 5.7, respectively, for four meshes (i.e., $N = 4,8,16,32$). It is seen that numerical solutions generated by the proposed technique converge and exhibit excellent agreement with the benchmark solution. It is worth noting that the discretization with only few linear elements can capture numerical solution with the sufficient accuracy. In addition, the relative percent error of the approximate displacement field versus the number of degrees of freedom is shown in Figure 5.6 for the approximation by linear elements. Clearly, the rate of convergence with respect to the L^2-norm, when the linear finite elements are employed, is approximately equal to two.

Table 5.6: Normalized radial displacement of pressurized circular hole in linear elastic, infinite medium. Results are reported at different values of radial coordinate $r=\sqrt{x_1^2+x_2^2}$ for four meshes.

	$u_r/(p_1R_1/E)$					
r/R_1	1.0	1.8	2.6	3.4	4.2	5.0
SBFEM, *N* = 4	1.2750	0.7083	0.4904	0.3750	0.3036	0.2550
SBFEM, *N* = 8	1.2937	0.7187	0.4976	0.3805	0.3080	0.2587
SBFEM, *N* = 16	1.2984	0.7214	0.4994	0.3819	0.3092	0.2597
SBFEM, *N* = 32	1.2996	0.7220	0.4998	0.3822	0.3094	0.2599
Exact solution	1.3000	0.7222	0.5000	0.3824	0.3095	0.2600

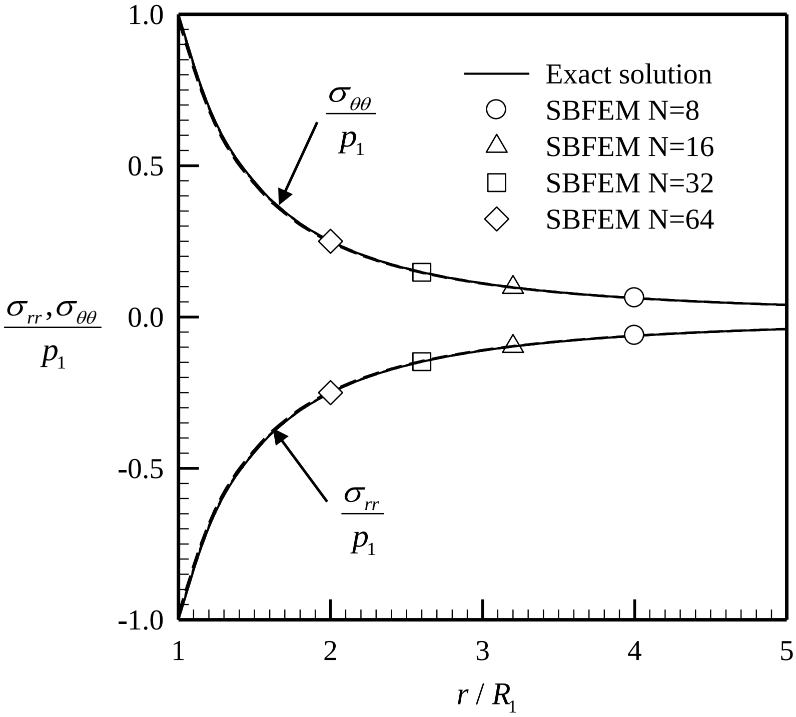

Figure 5.7*:* Normalized radial and hoop stress components along the radial direction of pressurized circular hole in linear elastic, infinite medium.

5.4 Linear Elastic Square Plate under Mixed Boundary Conditions

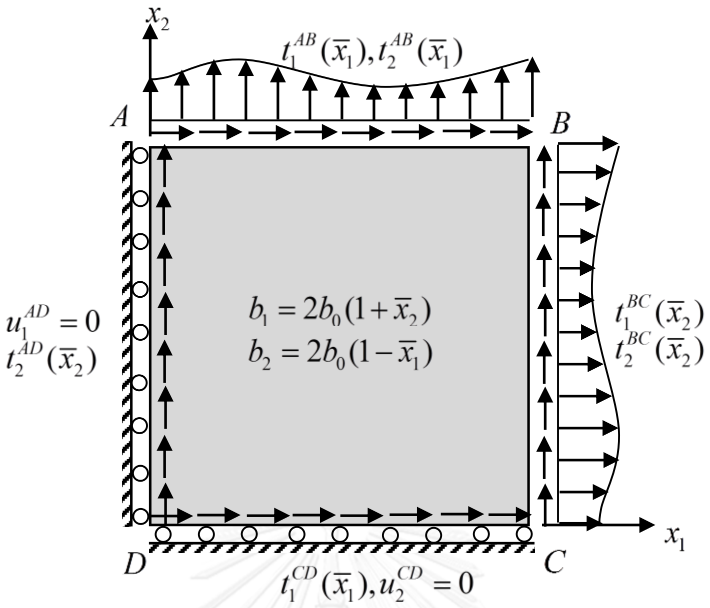

Figure 5.8: Schematic of elastic square plate under mixed boundary conditions.

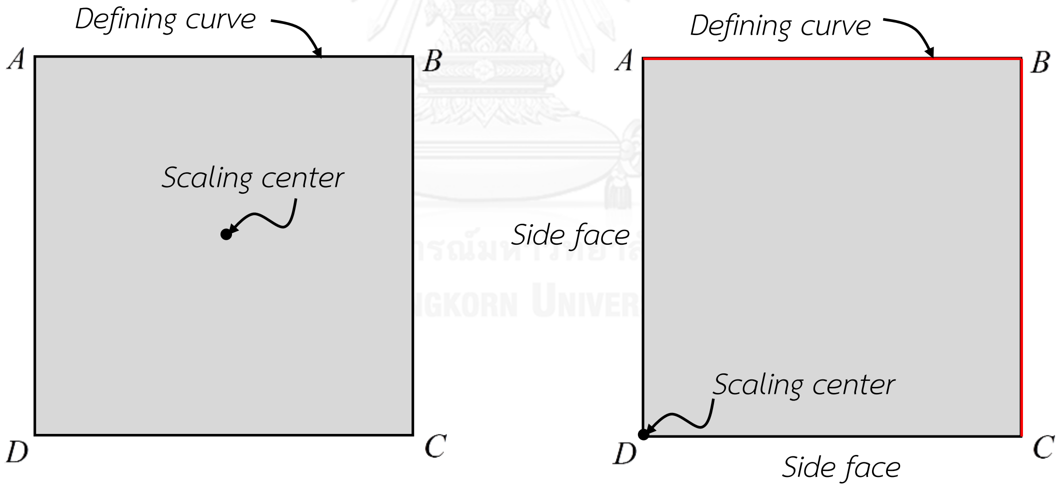

(a) (b)

Figure 5.9: Schematic of (a) defining curve corresponding to scaling center at center of plate and (b) defining curve corresponding to scaling center at corner point D.

Another representative problem in linear elasticity ($\Lambda = 2$) is chosen to demonstrate the capability of the implemented procedure to treat problems with distributed body source and prescribed state variable and surface flux on the boundary; the flexibility of scaling center and the accuracy of shape function in approximation. Consider a plane-strain, square plate *ABCD* made of a homogeneous, isotropic, linearly elastic material of Young's modulus E and Poisson's ratio ν as shown schematically in Figure 5.8. Note that the modulus matrix $\mathbf{D}$ for this particular problem is the same as the previous case. The plate is subjected to a linear body force field $b_1 = 2b_0(1+\bar{x}_2)$, $b_2 = 2b_0(1-\bar{x}_1)$ with b_0 denoting a constant and $\bar{x}_1 = x_1/l$, $\bar{x}_2 = x_2/l$ denoting the normalized coordinates whereas the non-uniform traction and homogeneous displacement boundary conditions are prescribed on its four sides as follows:

Side *AB*: $t_1^{AB} = b_0 l(3+14\bar{x}_1 - \bar{x}_1^2)$ and $t_2^{AB} = 2b_0 l(-4+4\bar{x}_1+3\bar{x}_1^2)$
Side *BC*: $t_1^{BC} = 6b_0 l(\bar{x}_2^2 - 2)$ and $t_2^{BC} = b_0 l(1+14\bar{x}_2+\bar{x}_2^2)$
Side *AD*: $u_1^{AD} = 0$ and $t_2^{AD} = -b_0 l(2\bar{x}_2+\bar{x}_2^2)$
Side *CD*: $t_1^{CD} = b_0 l(\bar{x}_1^2 - 2\bar{x}_1)$ and $u_2^{CD} = 0$

The exact solution for this particular problem under the plane strain condition can be readily obtained from a classical theory of linear elasticity and results are given by

$$Eu_1^{exact} = -2b_0 l^2(1+\nu)(1+\bar{x}_1-2\bar{x}_2+\bar{x}_1^2-3\bar{x}_2^2+\bar{x}_1\bar{x}_2)\bar{x}_1 \tag{5.3}$$

$$Eu_2^{exact} = -2b_0 l^2(1+\nu)(-1-2\bar{x}_1+\bar{x}_2-3\bar{x}_1^2+\bar{x}_2^2-\bar{x}_1\bar{x}_2)\bar{x}_2 \tag{5.4}$$

$$\sigma_{11}^{exact} = -\sigma_{22}^{exact} = -2b_0 l(1+2\bar{x}_1-2\bar{x}_2+3\bar{x}_1^2-3\bar{x}_2^2+2\bar{x}_1\bar{x}_2) \tag{5.5}$$

$$\sigma_{12}^{exact} = -b_0 l(-2\bar{x}_1-2\bar{x}_2+\bar{x}_1^2-\bar{x}_2^2-12\bar{x}_1\bar{x}_2) \tag{5.6}$$

In the geometry modeling, two different locations of the scaling center, one at the center of the plate (see Figure 5.9(a)) and the other at the corner (see Figure 5.9(b)), are considered. The geometry of plate is fully described by the chosen scaling center along with the defining curve ABCD for the former case and the defining curve *ABC* for the latter case. As a result, the boundaries *AD* and *CD* become the side faces (see Figure 5.9(b)) if the corner point D is chosen as the scaling center. In the analysis, Poisson's ration is taken as $\nu = 0.3$ and the defining curve is discretized by *N* identical linear elements. The relative percent errors of the displacement field, defined by (4.56), are reported in Table 5.7 for different numbers of degrees of freedom. It is seen that the level of accuracy resulting from the two different choices of the scaling center is similar. The normalized displacements $Eu_1/b_0 l^2$ and $Eu_2/b_0 l^2$ along the boundaries *AB* and *BC* are reported in Tables 5.8, 5.9, 5.10 and 5.11 for various locations and meshes. It can be seen that the numerical solutions converges to the exact solution as the number of elements *N* used to discretize the defining curve increases and, in addition, only few number of degrees of freedom is sufficient to obtain accurate displacements. The normalized normal stress components $\sigma_{11}/b_0 l$ and $\sigma_{22}/b_0 l$ along the boundaries *CD* and *AD* are also reported in Figures 5.11 and 5.12 along with the exact solution. Similar to the displacements, the present method also yields highly accurate stress components and the good convergent behavior; in particular, results obtained from all meshes are nearly indistinguishable from the benchmark solution. The rate of convergence of the approximation is also investigated when linear and quadratic elements are employed in the discretization of the defining curve and solution. Plots of the relative percent errors versus the number of degrees of freedom are reported in Figure 5.10 for both linear and quadratic elements. It can be seen that use of quadratic elements in the discretization yield higher rate of convergence in comparison with the linear elements. This implies that converged solutions for a specified tolerance can be achieved using only few quadratic elements.

Table 5.7: The relative percent error of displacement field versus number of elements (N) and number of degrees of freedom (NDOF) and two locations of scaling center.

Scaling center at center of plate			Scaling center at corner point D		
N	NDOF	Error (%)	N	NDOF	Error (%)
16	32	1.04308	8	18	1.34902
32	64	0.27932	16	34	0.34511
64	128	0.07193	32	66	0.08687
128	256	0.01838	64	130	0.02176

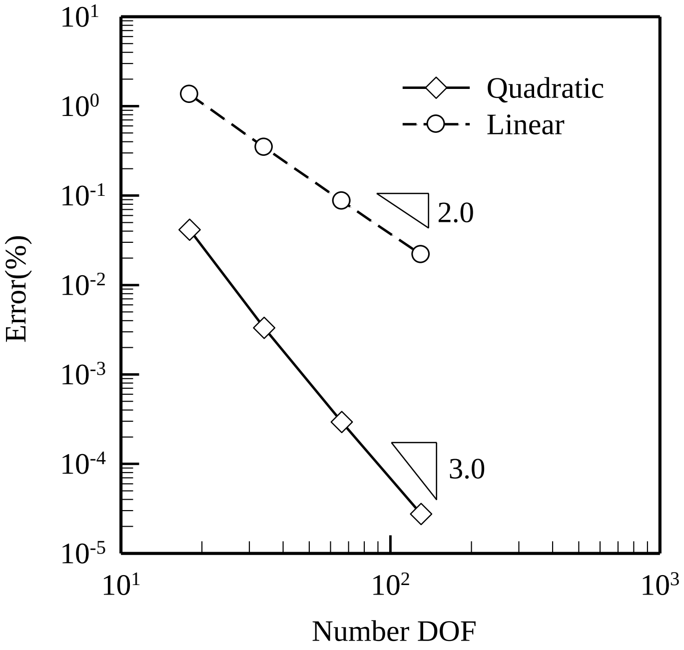

Figure 5.10: Relative percent error of displacement field versus number of degrees of freedom (DOF) for approximation by linear and quadratic elements.

Table 5.8: Normalized displacements along the boundary *AB* of elastic square plate subjected to mixed boundary conditions (scaling center at center of plate).

	Eu_1/b_0l^2					
$\bar{x}_1$	0.0	0.2	0.4	0.6	0.8	1.0
SBFEM, *N* = 8	0.0000	1.8395	3.0895	3.7001	3.5834	2.6139
SBFEM, *N* = 16	0.0000	1.8406	3.1545	3.7914	3.6303	2.6042
SBFEM, *N* = 32	0.0000	1.8508	3.1573	3.7995	3.6565	2.6012
SBFEM, *N* = 64	0.0000	1.8506	3.1612	3.8054	3.6588	2.6004
Exact solution	0.0000	1.8512	3.1616	3.8064	3.6608	2.6000
	Eu_2/b_0l^2					
$\bar{x}_1$	0.0	0.2	0.4	0.6	0.8	1.0
SBFEM, *N* = 8	-2.6066	-0.7364	1.7603	4.9094	8.6651	12.9104
SBFEM, *N* = 16	-2.6034	-0.7190	1.7536	4.8809	8.6551	12.9575
SBFEM, *N* = 32	-2.6020	-0.7284	1.7668	4.8886	8.6353	12.9835
SBFEM, *N* = 64	-2.6009	-0.7275	1.7671	4.8875	8.6334	12.9929
Exact solution	-2.6000	-0.7280	1.7680	4.8880	8.6320	13.0000

Table 5.9: Normalized displacements along the boundary *BC* of elastic square plate subjected to mixed boundary conditions (scaling center at center of plate).

	Eu_1/b_0l^2					
$\bar{x}_2$	0.0	0.2	0.4	0.6	0.8	1.0
SBFEM, *N* = 8	-7.8136	-6.9605	-5.5237	-3.4428	-0.7131	2.6139
SBFEM, *N* = 16	-7.8108	-6.9534	-5.5275	-3.4480	-0.7138	2.6042
SBFEM, *N* = 32	-7.8054	-6.9669	-5.5135	-3.4336	-0.7275	2.6012
SBFEM, *N* = 64	-7.8021	-6.9671	-5.5130	-3.4330	-0.7273	2.6004
Exact solution	-7.8000	-6.9680	-5.5120	-3.4320	-0.7280	2.6000
	Eu_2/b_0l^2					
$\bar{x}_2$	0.0	0.2	0.4	0.6	0.8	1.0
SBFEM, *N* = 8	0.0000	3.1272	6.0670	8.7440	11.0633	12.9104
SBFEM, *N* = 16	0.0000	3.1050	6.0769	8.7912	11.1201	12.9575
SBFEM, *N* = 32	0.0000	3.1015	6.0736	8.7951	11.1436	12.9835
SBFEM, *N* = 64	0.0000	3.0997	6.0739	8.7979	11.1470	12.9943
Exact solution	0.0000	3.0992	6.0736	8.7984	11.1488	13.0000

Table 5.10: Normalized displacements along the boundary AB of elastic square plate subjected to mixed boundary conditions (scaling center at corner point D).

	Eu_1/b_0l^2					
$\bar{x}_1$	0.0	0.2	0.4	0.6	0.8	1.0
SBFEM, *N* = 8	0.0000	1.7870	3.0433	3.6835	3.5878	2.6008
SBFEM, *N* = 16	0.0000	1.8263	3.1420	3.7877	3.6322	2.6012
SBFEM, *N* = 32	0.0000	1.8469	3.1542	3.7986	3.6571	2.6006
SBFEM, *N* = 64	0.0000	1.8496	3.1604	3.8052	3.6587	2.6143
Exact solution	0.0000	1.8512	3.1616	3.8064	3.6608	2.6000

	Eu_2/b_0l^2					
$\bar{x}_1$	0.0	0.2	0.4	0.6	0.8	1.0
SBFEM, *N* = 8	-2.7256	-0.7721	1.8011	4.9689	8.6766	12.8397
SBFEM, *N* = 16	-2.6262	-0.7306	1.7661	4.8982	8.6579	12.9369
SBFEM, *N* = 32	-2.6051	-0.7310	1.7700	4.8929	8.6363	12.9780
SBFEM, *N* = 64	-2.6009	-0.7281	1.7679	4.8886	8.6333	13.0038
Exact solution	-2.6000	-0.7280	1.7680	4.8880	8.6320	13.0000

Table 5.11: Normalized displacements along the boundary *BC* of elastic square plate subjected to mixed boundary conditions (scaling center at corner point D).

	Eu_1/b_0l^2					
$\bar{x}_2$	0.0	0.2	0.4	0.6	0.8	1.0
SBFEM, *N* = 8	-7.9407	-7.0248	-5.5067	-3.3831	-0.6694	2.6008
SBFEM, *N* = 16	-7.8346	-6.9726	-5.5213	-3.4319	-0.7027	2.6012
SBFEM, *N* = 32	-7.8086	-6.9716	-5.5119	-3.4297	-0.7246	2.6006
SBFEM, *N* = 64	-7.8021	-6.9683	-5.5126	-3.4320	-0.7268	2.6143
Exact solution	-7.8000	-6.9680	-5.5120	-3.4320	-0.7280	2.6000

	Eu_2/b_0l^2					
$\bar{x}_2$	0.0	0.2	0.4	0.6	0.8	1.0
SBFEM, *N* = 8	0.0000	3.0812	6.0130	8.7017	11.0266	12.8397
SBFEM, *N* = 16	0.0000	3.0922	6.0621	8.7806	11.1096	12.9369
SBFEM, *N* = 32	0.0000	3.0978	6.0699	8.7924	11.1408	12.9780
SBFEM, *N* = 64	0.0000	3.0988	6.0729	8.7973	11.1465	13.0038
Exact solution	0.0000	3.0992	6.0736	8.7984	11.1488	13.0000

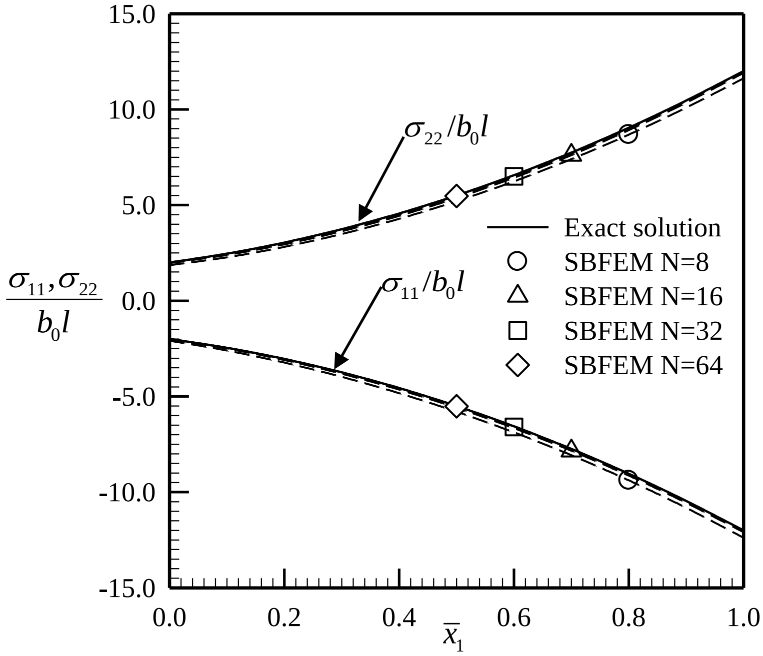

Figure 5.11: Normalized normal stress component along the boundary *CD* of elastic square plate subjected to mixed boundary conditions (scaling center at corner point D).

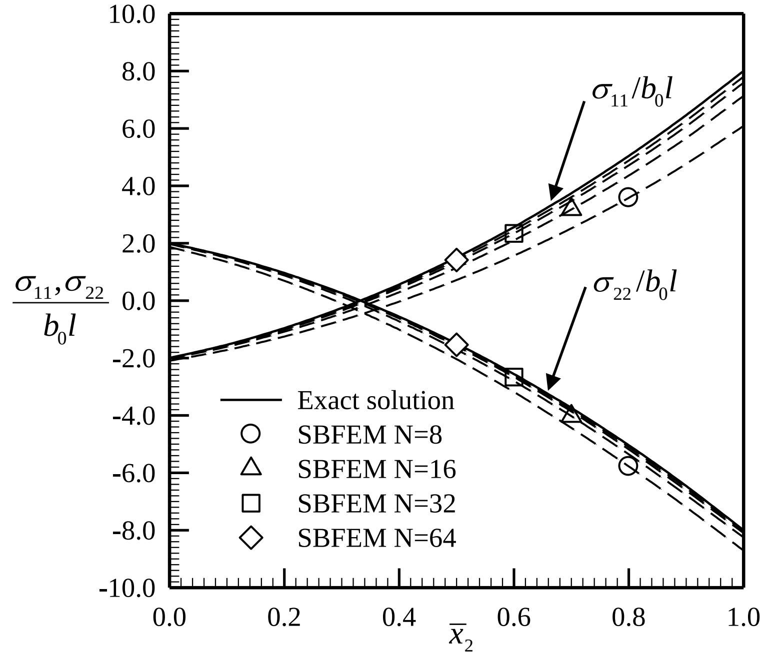

Figure 5.12: Normalized normal stress component along the boundary *AD* of elastic square plate subjected to mixed boundary conditions (scaling center at corner point D).

5.5 Linear Piezoelectric Square Plate

Next, a representative boundary value problem associated with the linear piezoelectricity ($\Lambda = 3$) is investigated to further highlight the capability of the proposed technique to treat linear multi-field problems. Let us consider a two-dimensional square plate of length l and made of a linear piezoelectric solid with all material constants taken from PZT-4 (Li et al., 2013) as shown in Figure 5.13(a). In particular, all non-zero entries of the modulus matrix $\mathbf{D}$ are given explicitly by $D_{11} = 139GPa$, $D_{15} = D_{51} = 74.3GPa$, $D_{16} = D_{61} = -6.98Cm^{-2}$, $D_{22} = 25.6GPa$, $D_{24} = 25.6GPa$, $D_{42} = 25.6GPa$, $D_{33} = 6.0\times10^{-9}C(Vm)^{-1}$, $D_{34} = D_{43} = 13.44Cm^{-2}$, $D_{44} = 25.6GPa$, $D_{55} = 113GPa$, $D_{56} = D_{65} = 13.84Cm^{-2}$, and $D_{66} = 5.47\times10^{-9}C(Vm)^{-1}$. For a purpose of verification, a set of prescribed data such as the distributed body source and boundary conditions on four sides is chosen such that the exact solution for the displacements (u_1 and u_2) and the electric potential (u_3) takes the following form

$$u_1 = u_{10}\bar{x}_1^2,\quad u_2 = u_{20}\bar{x}_2^2,\quad u_3 = \phi_0\bar{x}_2 \tag{5.7}$$

where u_{10}, u_{20}, ϕ_0 are given constants and $\bar{x}_1 = x_1/l$, $\bar{x}_2 = x_2/l$ are normalized coordinates. The corresponding exact stress field ($\sigma_{11},\sigma_{12},\sigma_{21},\sigma_{22}$) and electrical induction vector (σ_{13},σ_{23}) is given by

$$\sigma_{11} = (2D_{11}u_{10}\bar{x}_1 + 2D_{15}u_{20}\bar{x}_2 + D_{16}\phi_0)/l, \quad \sigma_{12} = \sigma_{21} = 0 \tag{5.8}$$

$$\sigma_{22} = (2D_{15}u_{10}\bar{x}_1 + 2D_{55}u_{20}\bar{x}_2 + D_{56}\phi_0)/l \tag{5.9}$$

$$\sigma_{13} = 0, \quad \sigma_{23} = (2D_{16}u_{10}\bar{x}_1 + 2D_{56}u_{20}\bar{x}_2 - D_{66}\phi_0)/l \tag{5.10}$$

The distributed body source that is in equilibrium with the above stress and electric induction can readily be obtained from (3.4) as

$$b_1 = -2D_{11}u_{10}/l^2, \quad b_2 = -2D_{55}u_{20}/l^2, \quad b_3 = -2D_{56}u_{20}/l^2 \tag{5.11}$$

In the modeling, the scaling center is chosen at a point *D* and the prescribed conditions on the side faces *AD* and *CD* and the boundaries *AB* and *BC* are given below

Side *AB*: $t_1^{AB} = 0$, $t_2^{AB} = (2D_{15}u_{10}\bar{x}_1 + 2D_{55}u_{20} + D_{56}\phi_0)/l$,
$t_3^{AB} = (2D_{16}u_{10}\bar{x}_1 + 2D_{56}\bar{u}_{20} - D_{66}\phi_0)/l$

Side *BC*: $t_1^{BC} = (2D_{11}u_{10} + 2D_{15}u_{20}\bar{x}_2 + D_{16}\phi_0)/l$, $t_2^{BC} = 0$, $t_3^{BC} = 0$

Side *AD*: $u_1 = 0$, $u_2 = u_{20}\bar{x}_2^2$, $t_3^{AD} = 0$

Side *CD*: $t_1^{CD} = 0$, $u_2 = 0$, $u_3 = 0$

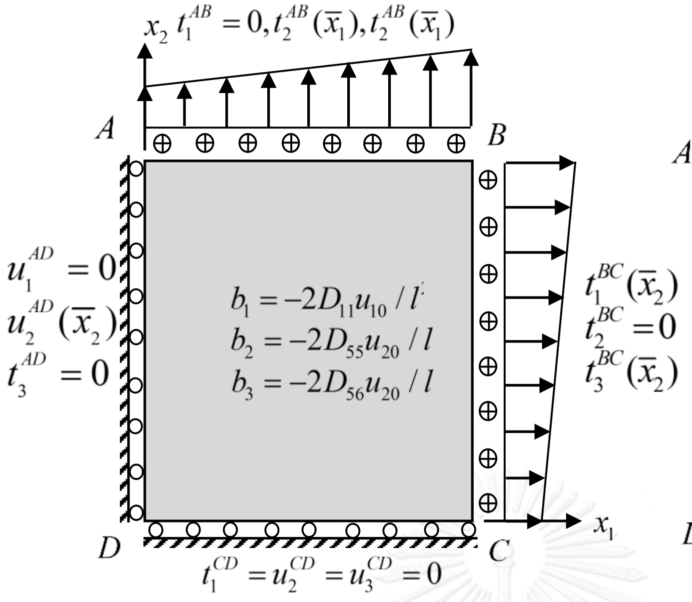

(a) (b)

Figure 5.13: Schematic of (a) linear piezoelectric square plate under mixed boundary conditions and (b) scaling center and defining curve used in scale boundary finite element analysis.

It is worth noting that the boundary conditions shown above are chosen to represent the general prescribed data on the side faces and boundaries of the domain. In the numerical study, a series of meshes with *N* identical linear elements is constructed to discretize the defining curve and solution along the scale boundary direction and $u_{20}/u_{10}=2$, $D_{16}\phi_0/D_{11}u_{10}=1$ are employed. Computed displacements and electric potential along the diagonal line *BD* are reported in Tables 5.12 and 5.13 for various meshes. It is seen for this particular problem that the proposed technique yield highly accurate results even when relatively coarse meshes containing only few degrees of freedom are employed. In addition, the improvement of solutions as the mesh is refined is clearly observed. The good quality of numerical solutions is also confirmed for the body flux as indicate in Figures 5.15 and 5.16. Computed stresses and electrical induction along the diagonal line *BD* show an excellent agreement with the exact solution; in particular, only slight difference between solutions can be seen for very coarse meshes while almost indistinguishable results are obtained for fine meshes. As indicated by results in Figure 5.14, the rate of convergence of the state variable is about two when linear elements are used in the approximation.

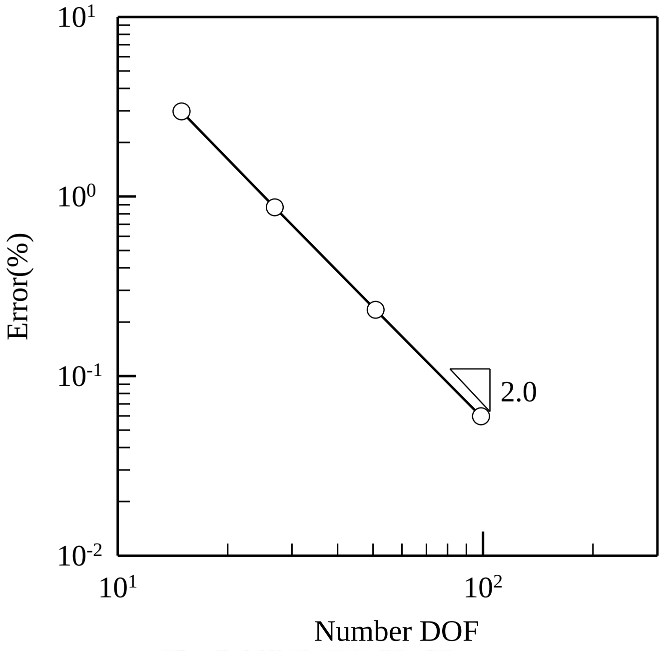

Figure 5.14: Relative percent error of displacement and electric potential versus number of degrees of freedom (DOF) for approximation by linear elements.

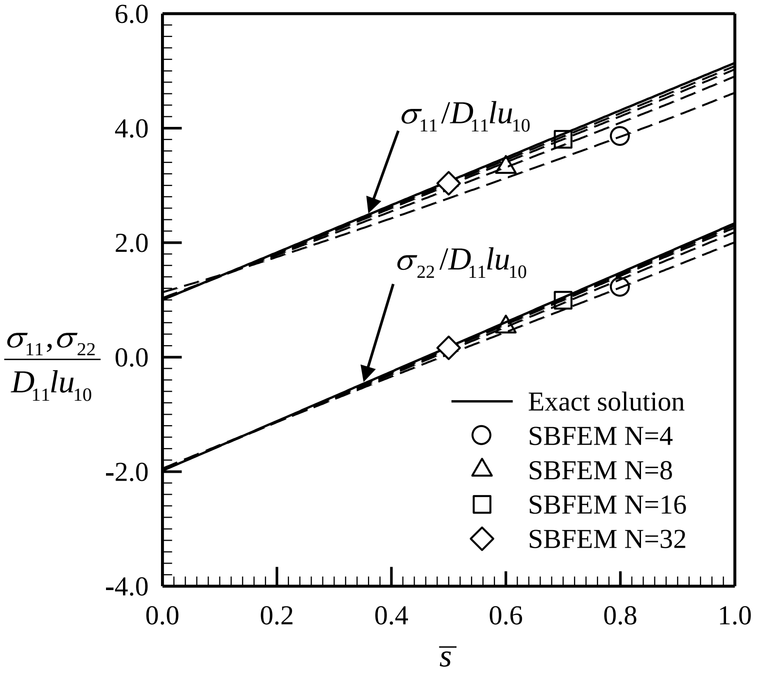

Figure 5.15: Normalized non-zero stress components along the diagonal line BD of a piezoelectric square plate subjected to mixed boundary conditions. Results are reports as a function of normalized length $\bar{s} = s/\sqrt{2}l$ where s is the length along the line BD measured from point D.

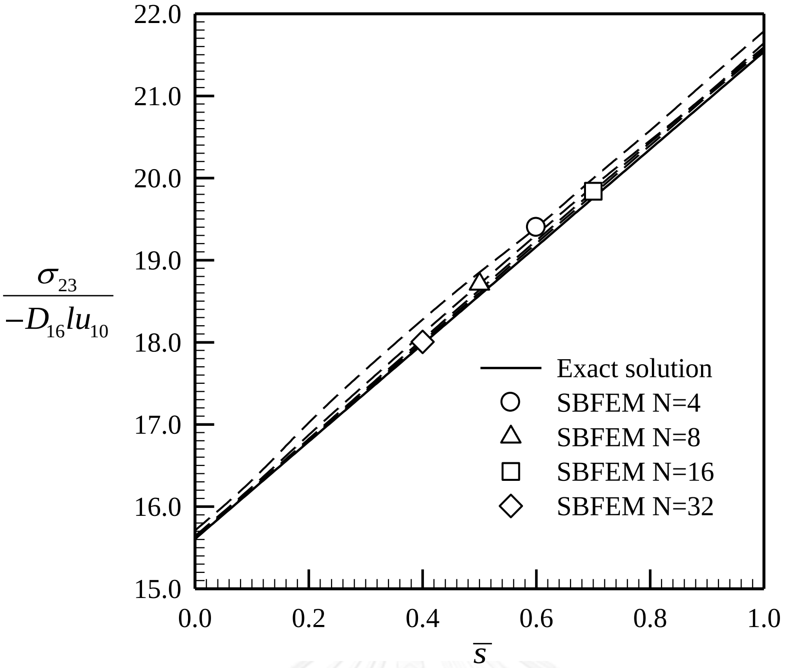

Figure 5.16: Normalized a non-zero electrical induction component along the diagonal line BD of a piezoelectric square plate subjected to mixed boundary conditions. Results are reports as a function of normalized length $\bar{s} = s/\sqrt{2}l$ where s is the length along the line BD measured from point D.

Table 5.12: Normalized electrical potential along the diagonal line *BD* of linear piezoelectric square plate subjected to mixed boundary conditions. Results are reports as a function of normalized length $\bar{s} = s/\sqrt{2}l$ where s is the length along the line *BD* measured from point *D*.

	u_3/ϕ_0					
$\bar{s}$	0.0	0.2	0.4	0.6	0.8	1.0
SBFEM, *N* = 4	0.0000	0.2013	0.4019	0.6013	0.7991	0.9938
SBFEM, *N* = 8	0.0000	0.2003	0.4004	0.6003	0.7998	0.9976
SBFEM, *N* = 16	0.0000	0.2001	0.4001	0.6001	0.7999	0.9992
SBFEM, *N* = 32	0.0000	0.2000	0.4000	0.6000	0.8000	0.9997
Exact solution	0.0000	0.2000	0.4000	0.6000	0.8000	1.0000

Table 5.13: Normalized displacements along the diagonal line *BD* of linear piezoelectric square plate subjected to mixed boundary conditions. Results are reports as a function of normalized length $\bar{s} = s/\sqrt{2}l$ where s is the length along the line *BD* measured from point *D*.

	u_1/u_{10}					
$\bar{s}$	0.0	0.2	0.4	0.6	0.8	1.0
SBFEM, *N* = 4	0.0000	0.0369	0.1351	0.3278	0.6291	1.0459
SBFEM, *N* = 8	0.0000	0.0393	0.1531	0.3503	0.6360	1.0252
SBFEM, *N* = 16	0.0000	0.0398	0.1582	0.3574	0.6385	1.0098
SBFEM, *N* = 32	0.0000	0.0400	0.1596	0.3593	0.6396	1.0033
Exact solution	0.0000	0.0400	0.1600	0.3600	0.6400	1.0000
	u_2/u_{20}					
$\bar{s}$	0.0	0.2	0.4	0.6	0.8	1.0
SBFEM, *N* = 4	0.0000	0.0821	0.3272	0.7222	1.2554	1.9134
SBFEM, *N* = 8	0.0000	0.0803	0.3220	0.7213	1.2739	1.9679
SBFEM, *N* = 16	0.0000	0.0801	0.3205	0.7204	1.2786	1.9891
SBFEM, *N* = 32	0.0000	0.0800	0.3201	0.7201	1.2797	1.9965
Exact solution	0.0000	0.0800	0.3200	0.7200	1.2800	2.0000

5.6 Finite Elastic Plate with Edge Notch

As the last example, a representative boundary value problem associated with a finite elastic plate containing an edge notch is considered in order to investigate the capability of the proposed technique to treat problems with a singular field. In particular, consider a plain-strain, rectangle plate made of a homogeneous, isotropic, linearly elastic material of Young's modulus E and Poisson's ratio ν and subjected to uniform normal traction at both ends as shown schematically in Figure 5.17(a). Note that the modulus matrix $\mathbf{D}$ for this particular problem is the same as the previous case. Two values of an opening angle of the notch, α =0, 30, are considered in the numerical study. When the opening angle α approaches zero, the notch becomes a crack. In this particular case, the reference solution of the mode-I stress intensity factor SIF K_I is obtained from the work of Brown and Srawley (1966) by

$$K_I = C\sigma_0\sqrt{a\pi} \tag{5.12}$$

where C is a finite geometry factor defined by

$$C = 1.12 - 0.231\left(\frac{a}{W}\right) + 10.55\left(\frac{a}{W}\right)^2 - 21.72\left(\frac{a}{W}\right)^3 + 30.39\left(\frac{a}{W}\right)^4 \tag{5.13}$$

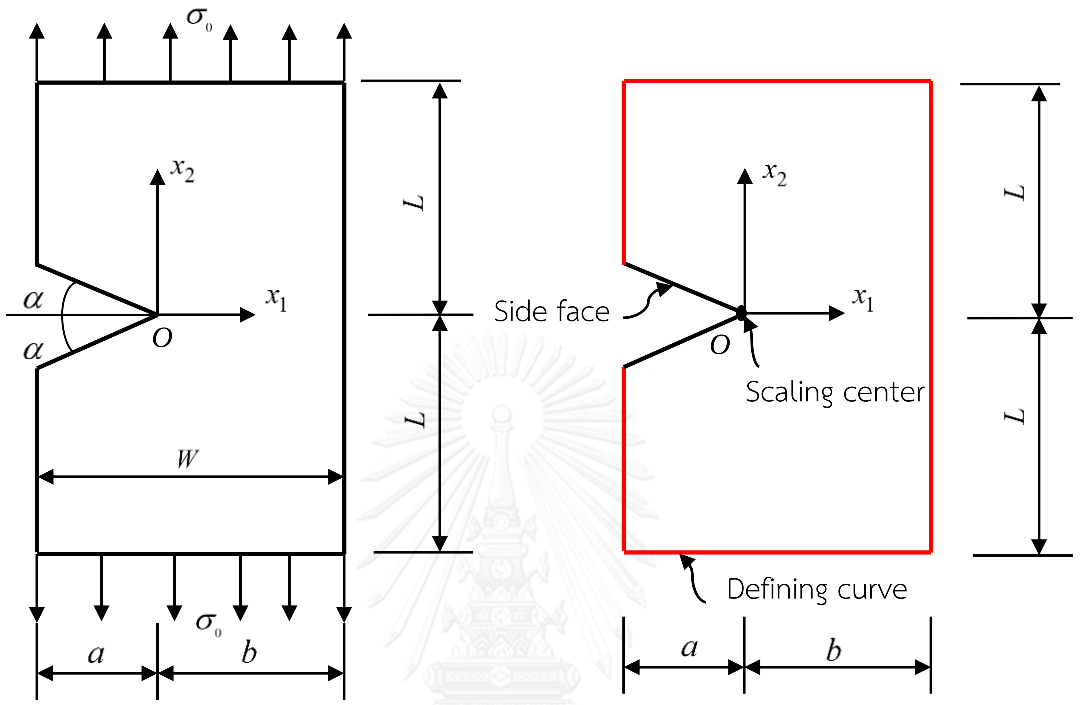

(a) (b)

Figure 5.17: Schematics of (a) finite elastic plate containing edge notch and (b) scaling center and defining curve used in scale boundary finite element analysis.

In the geometry modeling, the scaling center is selected at the notch tip and the defining curve is discretized by N identical linear elements. In the numerical study, the dimensions of the plate are chosen such that $a = b$ and $W = L$. Results for this problem are also generated by a reliable finite element program and used as the benchmark solutions. In the finite element analysis, the plate is used 6–node triangular elements. In the case of crack, numerical results for the mode-I stress intensity factor K_I are reported in Table 5.14. It is seen that numerical solutions generated by the proposed technique converge and also exhibit excellent agreement with the benchmark solution. In addition, K_I obtained from the SBFEM converges faster than that obtained from the FEM. The order of singularity (i.e., one of eigenvalues obtained from the present method) is also reported in Table 5.15. It is evident that the order of singularity converges to the theoretical value (i.e., 0.5) as expected. The normalized normal stress σ_{22}/σ_0 along the x_1 direction is plotted in Figure 5.18 along with the

FE solution. Clearly, the proposed method yields highly accurate stress in the vicinity of the crack tip. When the angle α is equal to 30 degree, the normalized normal stress σ_{22} / σ_0 along the x_1 direction is reported in Figure 5.19 along with, again, the FE solution. As evident from this set of results, the computed near-tip stress shows the good convergence behavior and good agreement with the benchmark solution with using only few linear elements.

Table 5.14: Mode-I stress intensity factor of finite elastic plate containing edge crack.

	K_I	$\eta(\%) = \left\lvert \frac{K_I^{Ref} - K_I^{SBFEM}}{K_I^{Ref}} \right\rvert x100$	$\eta(\%) = \left\lvert \frac{K_I^{FEM} - K_I^{SBFEM}}{K_I^{FEM}} \right\rvert x100$
SBFEM, N = 11	65.6009	7.4016	7.1926
SBFEM, N = 21	69.6269	1.7187	1.4969
SBFEM, N = 41	70.3924	0.6382	0.4139
SBFEM, N = 81	70.7098	0.1901	0.0352
Ref solution	70.8445		
FEM, N = 66700	70.6850		

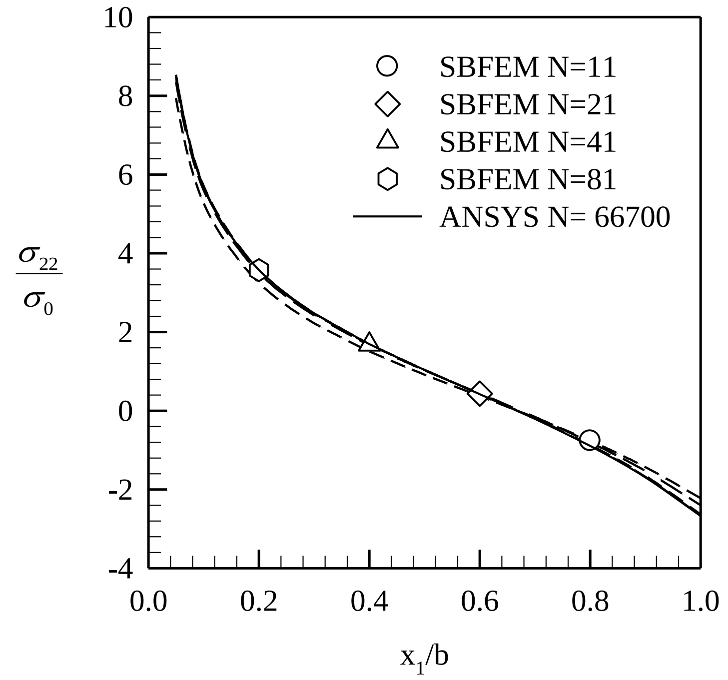

Figure 5.18: Normalized normal stress component σ_{22} along x_1-direction of finite elastic plate containing edge crack (i.e., $\alpha = 0$) subjected to uniform normal traction at both ends.

Table 5.15: The first eigenvalue corresponding to the singular stress field when the opening angle $\alpha = 0$.

	$\lambda_1(\alpha = 0)$
SBFEM, N = 11	0.49691
SBFEM, N = 21	0.49998
SBFEM, N = 41	0.50006
SBFEM, N = 81	0.50001

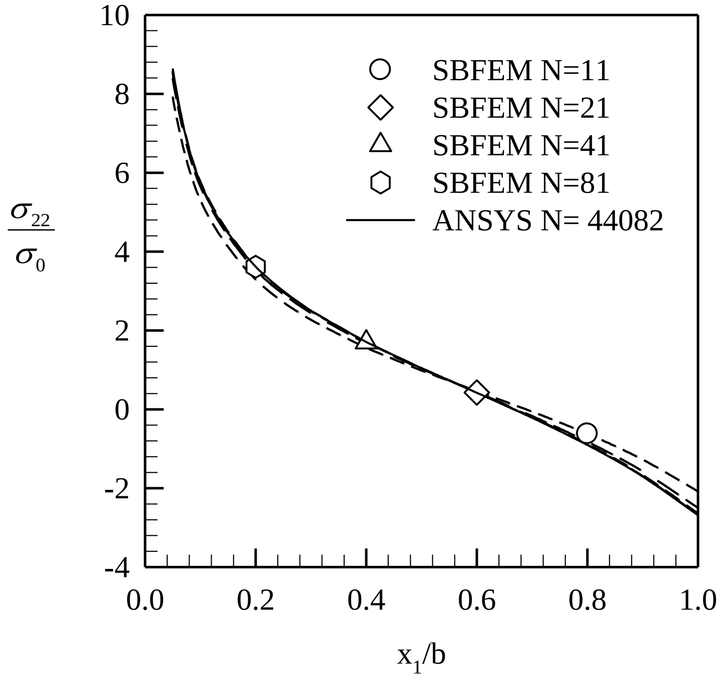

Figure 5.19: Normalized normal stress component σ_{22} along x1-direction of finite elastic plate containing edge notch (i.e., $\alpha = 30$) subjected to uniform normal traction at both ends.

Chapter 6
CONCLUSIONS

6.1 Summary

A numerical technique based upon the scaled boundary finite element method (SFBEM) has been successfully developed for solving two-dimensional, multi-field boundary value problems. Both the formulation and implementations have been established in a general framework allowing various classes of linear boundary value problems (e.g., steady-state heat conduction problems, Laplace's equation, linear elasticity, linear piezoelectricity, etc.) and a set of general data such as the domain geometry, the prescribed distributed body source, the prescribed boundary conditions, and the contribution of the side-face conditions to be treated in a single, unified fashion. Results from an extensive numerical study for various scenarios have revealed that the proposed SBFEM yields highly accurate numerical solutions with the good convergence behavior. Relatively coarse meshes containing only few degrees of freedom have been found to accurately capture both the state variable and the body flux. In particular, both prescribed state variables and prescribed surface flux along the side faces and the general mixed boundary conditions along the scale boundary direction have been implemented into the proposed procedure and this, therefore, provides the flexibility in the selection of the scaling center and defining curve for describing the domain geometry.

Several numerical examples have been solved and obtained results have been compared with analytical solutions to validate the proposed technique. Linear and quadratic shape functions have been employed in the approximation of the defining curve and the trial and test functions. From the convergence study of numerical solutions, it has been found that the rate of convergences resulting from the use of quadratic elements in the approximation is higher than that of the linear elements. In addition, the capability and robustness of the proposed technique to handle the general boundary conditions, general geometry, prescribed state variables, and the flexible choices of the scaling center have been demonstrated. Extensive analysis of problems in various fields such as steady-state heat conduction problems, linear elasticity problems, and linear piezoelectric problems, have also indicated that the proposed technique is promising in terms of accuracy and computational efficiency and can handle problems in various different scenarios in an efficient and unified fashion.

6.2 Limitations and Directions of Future Research

Although the proposed technique has been implemented within the context of two-dimensional boundary value problems with domains described by a single scaling center, its underlying formulation and computational procedure are sufficiently general and should provide an essential basis for an extension to treat more general bodies such as those requiring multiple scaling centers to fully describe their geometry. Another potential extension is to generalize the present unified framework to three-dimensional multi-field problems.

REFERENCES

Brown, W. F. J., Srawley, J. (1966). Plane strain crack toughness testing of high strength metallic materials. ASTM 410.

Chen, S. S., Li, Q. H., Liu, Y. H., Chen, H. T. (2013). "Identification of elastic orthotropic material parameters by the scaled boundary finite element method." Engineering Analysis with Boundary Elements **37**(4): 781-787.

Chowdhury, M.S., Song, C., Gao, W. (2014). "Probabilistic fracture mechanics with uncertainty in crack size and orientation using the scaled boundary finite element method." Computers & Structures **137**: 93-103.

Dai, S., Augarde, C., Du, C., Chen, D. (2015). "A fully automatic polygon scaled boundary finite element method for modelling crack propagation." Engineering Fracture Mechanics **133**: 163-178.

Deeks, A. J. (2004). "Prescribed side-face displacements in the scaled boundary finite-element method." Computers & Structures **82**(15–16): 1153-1165.

Deeks, A. J., Wolf, J. P. (2002). "An h-hierarchical adaptive procedure for the scaled boundary finite-element method." International Journal for Numerical Methods in Engineering **54**: 585-605.

Deeks, J. A., Wolf, P. J. (2002). "A virtual work derivation of the scaled boundary finite-element method for elastostatics." Computational Mechanics **28**(6): 489-504.

Dieringer, R., Becker, W. (2015). "A new scaled boundary finite element formulation for the computation of singularity orders at cracks and notches in arbitrarily laminated composites." Composite Structures **123**: 263-270.

Doherty, J. P., Deeks, A. J. (2005). "Adaptive coupling of the finite-element and scaled boundary finite-element methods for non-linear analysis of unbounded media." Computers and Geotechnics **32**(6): 436-444.

Gravenkamp, H., Birk, C., Song, C. (2014). "The computation of dispersion relations for axisymmetric waveguides using the Scaled Boundary Finite Element Method." Ultrasonics **54**(5): 1373-1385.

He, Y., Yang, H., Deeks, A. J. (2012). "An Element-free Galerkin (EFG) scaled boundary method." Finite Elements in Analysis and Design **62**: 28-36.

He, Y., Yang, H., Deeks, A. J. (2014). "Use of Fourier shape functions in the scaled boundary method." Engineering Analysis with Boundary Elements **41**: 152-159.

He, Y., Yang, H., Xu, M., Deeks, A. J. (2013). "A scaled boundary finite element method for cyclically symmetric two-dimensional elastic analysis." Computers & Structures **120**: 1-8.

Li, C., Man, H., Song, C., Gao, W. (2013a). "Fracture analysis of piezoelectric materials using the scaled boundary finite element method." Engineering Fracture Mechanics **97**: 52-71.

Li, C., Ooi, E. T., Song, C., Natarajan, S. (2015). "SBFEM for fracture analysis of piezoelectric composites under thermal load." International Journal of Solids and Structures **52**: 114-129.

Li, C., Song, C., Man, H., Ooi, E. T., Gao, W. (2014). "2D dynamic analysis of cracks and interface cracks in piezoelectric composites using the SBFEM." International Journal of Solids and Structures **51**(11–12): 2096-2108.

Li, F., Ren, P. (2016). "A novel solution for heat conduction problems by extending scaled boundary finite element method." International Journal of Heat and Mass Transfer **95**: 678-688.

Li, M., Guan, H., Zhang, H., Liu, J. (2013b). "Three-dimensional investigation of wave–pile group interaction using the scaled boundary finite element method—Part II: Application results." Ocean Engineering **64**: 185-195.

Li, M., Zhang, H., Guan, H. (2011). "Study of offshore monopole behavior due to ocean waves." Ocean Engineering **38**: 1946-1956.

Li, M., Zhang, H., Guan, H., Lin, G. (2013). "Three-dimensional investigation of wave–pile group interaction using the scaled boundary finite element method. Part I: Theoretical developments." Ocean Engineering **64**: 174-184.

Liu, J., Lin, G. (2012). "A scaled boundary finite element method applied to electrostatic problems." Engineering Analysis with Boundary Elements **36**(12): 1721-1732.

Martin, H. S. (2014). Elasticity: Theory, Application, and Numerics., Academic Press is an imprint of Elsevier.

Meng, X. N., Zou, Z. J. (2013). "Radiation and diffraction of water waves by an infinite horizontal structure with a sidewall using SBFEM." Ocean Engineering **60**: 193-199.

Ooi, E. T., Shi, M., Song, C., Tin-Loi, F., Yang, Z. J. (2013). "Dynamic crack propagation simulation with scaled boundary polygon elements and automatic remeshing technique." Engineering Fracture Mechanics **106**: 1-21.

Ooi, E. T., Song, C., Tin-Loi, F. (2014). "A scaled boundary polygon formulation for elasto-plastic analyses." Computer Methods in Applied Mechanics and Engineering **268**: 905-937.

Ooi, E. T., Song, C., Tin-Loi, F., Yang, Z. J. (2012). "Automatic modelling of cohesive crack propagation in concrete using polygon scaled boundary finite elements." Engineering Fracture Mechanics **93**: 13-33.

Reddy, J. N. (1993). An introduction to the finite element method. McGraw-Hill.

Shrestha, S., Ohga, M. (2007). "Scaled boundary finite element method for various crack problems." Steel Structures **7**: 277-287.

Song, C., Tin-Loi, F., Gao, W. (2010). "Transient dynamic analysis of interface cracks in anisotropic biomaterials by the scaled boundary finite-element method." International Journal of Solids and Structures **47**: 978-989.

Song, C., Wolf, J. P. (1997). "The scaled boundary finite-element method—alias consistent infinitesimal finite-element cell method—for elastodynamics." Computer Methods in Applied Mechanics and Engineering **147**(3): 329-355.

Song, C., Wolf, J. P. (1997). "The scaled boundary finite-element method: analytical solution in frequency domain." <u>Computer Methods in Applied Mechanics and Engineering</u> **164**(1-2): 249-264.

Song, C., Wolf, J. P. (1999). "Body loads in scaled boundary finite-element method." <u>Computer Methods in Applied Mechanics and Engineering</u> **180**(1–2): 117-135.

Song, C., Wolf, J. P. (2000). "The scaled boundary finite-element method – a primer: solution procedures." <u>Computers & Structures</u> **78**(1–3): 211-225.

Vu, T. H., Deeks, A. J. (2006). "Use of higher-order shape functions in the scaled boundary finite element method." <u>International Journal for Numerical Methods in Engineering</u> **65**(10): 1714-1733.

Vu, T. H., Deeks, A. J. (2008). "A p-adaptive scaled boundary finite element method based on maximization of the error decrease rate." <u>Computational Mechanics</u> **41**(3): 441-455.

Vu, T. H., Deeks, A. J. (2014). "Using fundamental solutions in the scaled boundary finite element method to solve problems with concentrated loads." <u>Computational Mechanics</u> **53**(4): 641-657.

Wolf, J. P. (2003). <u>The scaled boundary finite element method</u>, John Wiley and Sons, Chichester.

Wolf, J. P., Song, C. (1995a). "Consistent infinitesimal finite-element cell method: in-plane motion." <u>Computer Methods in Applied Mechanics and Engineering</u> **123**(1): 355-370.

Wolf, J. P., Song, C. (1995b). "Unit-impulse response matrix of unbounded medium by infinitesimal finite-element cell method." <u>Computer Methods in Applied Mechanics and Engineering</u> **122**(3): 251-272.

Wolf, J. P., Song, C. (1996a). "Finite-element modelling of undounded media." 70.

Wolf, J. P., Song, C. (1996b). <u>Finite-element modelling of unbounded domain</u>. Jonh Wiley and Sons, Chichester.

Wolf, J. P., Song, C. (2000). "The scaled boundary finite-element method – a primer: derivations." Computers & Structures **78**(1–3): 191-210.

Wolf, J. P., Song, C. (2001). "The scaled boundary finite-element method – a fundamental solution-less boundary-element method." Computer Methods in Applied Mechanics and Engineering **190**(42): 5551-5568.

APPENDIX

VITA

The author, Chung Van Nguyen, was born in Ho Chi Minh City, Viet Nam, on January 04, 1979. He received a Bachelor of Engineering and Master of Engineering degree in Civil Engineering from Ho Chi Minh City University of Technology in 2002 and 2008. He joined Industrial & Civil Designing Consulting Joint Stock Company (IDCo) in 2003. He also taught at College of Technology and Industrial Management (CTIM) in 2003. He has been lecturer in Faculty of Civil Engineering of HCMC University of Technology and Education in 2008. In 2013, he achieved the scholarship by CU Scholarship for ASEAN countries 2013 for his doctoral degree in Civil Engineering at Chulalongkorn University under the supervision of Associate Professor Dr. Jaroon Rungamornat. His current research interest is in Theoretical and Applied Mechanics: Solid Mechanics, Fracture Mechanics and Computational Techniques: Finite Element Method, Boundary Element Method, and Scaled Boundary Element Method.